

Diss. ETH No. 18690

Oscillating Flow Liquid Cooling for High Performance Computing Systems

A dissertation submitted to

ETH ZURICH

for the degree of

DOCTOR OF SCIENCES

presented by

RETO WÄLCHLI

Dipl. Masch.-Ing. ETH

born on October 27, 1978

citizen of Zürich and Brittnau, Switzerland

Accepted on the recommendation of

Prof. Dr. Dimos Poulikakos, examiner

Prof. Dr. Kostantinos Boulouchos, co-examiner

Dr. Bruno Michel, co-examiner

2009

Acknowledgment

The work described in this thesis was performed at IBM Research - Zurich in Rüschlikon and at the Laboratory of Thermodynamics in Emerging Technologies (LTNT) of ETH Zurich. I am grateful to all the people who contributed in one way or the other, including the members of the ETH group, the Advanced Thermal Packaging (ATP) Group at IBM Research - Zurich, the support staff at IBM, and all those from other groups who have helped.

First of all, I would like to express my sincere thanks to my advisor, Prof. Dr. Dimos Poulikakos of LTNT for his guidance and support during the course of the project. I would like to convey my cordial gratitude to my co-examiner Dr. Bruno Michel who enabled me to conduct my thesis at ZRL and for his illuminative ideas. My thanks also go to Prof. Dr. Konstantinos Boulouchos for all his efforts as co-examiner of my dissertation.

From the ATP group, very special thanks go to Thomas Brunschwiler for the un-resting support and all the enlightening discussions on microchannel heat and mass transfer. Furthermore, I am grateful to Dr. Ryan Linderman for giving me support for my thesis. I would like to thank Urs Kloter, Martin Witzig, and Hansruedi Steinauer for their continuous help during my experimental work.

This work would not have been possible without the endurance and never-ending support of my dearest, Sibylle and Johan. Thank you for your unwavering encouragement and the quiet sleep during the closing of my thesis. A final thanks goes to my parents, Susanne and Rolf, and my siblings, Bettina and Daniel.

Reto Wälchli

October 2009

Zürich, Switzerland

Summary

The scope of the thesis at hand is to characterize and develop a novel thermal management system for high performance electronic equipment. Under the constraint of a low form factor device, a self-contained, hermetically sealed, liquid heat spreading system was pursued to outperform the cooling potential of present-day technologies. Furthermore, it should facilitate a soft transition to liquid cooling by means of a hybrid system; the combination of high-performance liquid cooled microchannel heat sinks with conventional air cooling. Efficient waste heat spreading from the heat source via a microchannel heat absorber, and the interconnecting tubes, to the large-area heat dissipator cold plate devices is established by means of an oscillating fluid flow regime generated from a set of reciprocating pumps. The fluid contained in the system is kept to a minimum amount of several milliliters to limit a potential damage in the case of leakage. A secondary cooling loop, established either with conventional finned air heat sinks or another liquid flow, is thermally connected to the primary heat spreading system.

The thesis provides a thorough description and characterization of the above delineated liquid cooling heat spreading system. However, the focus lies in the description of the heat and mass transfer within this dynamically-acting heat spreading system with regard to the characteristic measures of frequency and fluid displacement and the design of the mesh-type microchannel cold plates. The secondary cooling loop, dumping heat to the environment, and the fluid displacement pumps are introduced pragmatically with the objective of exploring the performance of the respective liquid heat spreading technology.

Chapter Two describes an efficient modeling approach that allows one to determine the fluidic and thermal performance of microchannel cold plates. Starting from local microchannel-scale numerical modeling, unit cell performance measures are determined. Velocity-dependent pressure losses and heat transfer coefficients are identified to characterize microchannel heat transfer meshes of different porosities. A global chip-scale network model is discussed which predicts the efficiency of such heat transfer devices in steady-state flow conditions. The analytical and numerical results are verified with experimental work.

In Chapter Three, a full-system numerical simulation studies the fluidic and thermal performance of the self-contained, oscillating liquid cooling heat spreading system. The characteristic properties of microchannel cold plate unit cells with various as-

pect ratios are implemented into a simplified porous media model. The dependency of the overall system performance on the heat transfer mesh porosity, the oscillation frequency, and the fluid displacement are investigated and discussed. This allows one to appraise the driving parameters and to estimate the performance limitations of the according cooling apparatus. The conclusions of this numerical work constrict the frequency range to $0.5 \leq f \leq 2$ Hz and the relative fluid displacement to $1 \leq \bar{A} \leq 1.5$. Frequencies of $f \geq 10$ that would enable superior heat transfer rates in such a reciprocating fluid flow system are impossible to manage with regard to a reasonable pumping work. A large fluid displacement and low frequency driving regime proves to be the most effective. Furthermore, the requested cooling performance defines the optimal design of the microchannel heat transfer mesh.

The next chapter, Chapter Four, examines the experimental implementation of the according technology. A test setup containing the absorber/dissipator microchannel cold plates, the interconnecting tubes, and the displacement pumps is built. A heater/sensor chip is adopted to simulate a high power density microprocessor. The thermal and fluidic characteristics are presented in a time-resolved and cycle-averaged manner. A peak cooling performance from chip to the thermodynamic ground potential of 180 W/cm^2 ($\Delta T = 67 \text{ K}$, fluid pumping power 1 W) is demonstrated experimentally. Two different oscillation regimes, called *linear* and *radial*, are investigated. In terms of temperature cycling, radial oscillations are advantageous at some local points on the chip. However, *linear* is preferable from a performance perspective and it is of lower complexity.

Chapter Five covers the combination of numerical and experimental work on an oscillating liquid heat spreading system. The geometrical constraints are bound to an existing vapor chamber heat sink device that is implemented in one of IBM's server systems. Therefore, the self contained microchannel absorber/dissipator heat transfer mesh is intended to be integrated into the base of the appropriate air heat sink. The effective conductivity, the heat spreading improvement and the thinning potential of the air heat sink base over a passive system, are discussed.

Zusammenfassung

Das Ziel der vorliegenden Doktorarbeit ist die Charakterisierung und Entwicklung eines neuartigen Wärmemanagementsystems für hochleistungsfähige, elektronische Geräte. Unter der Bedingung eines flachen Formfaktors wurde der Ansatz eines in sich hermetisch geschlossenen Mikrokanalkühlsystems verfolgt, welcher die Effizienz der gegenwärtigen Technologien deutlich übertreffen sollte. Zudem ist es das Ziel mit dem vorliegenden hybriden Kühlsystem die Überleitung zu reiner Flüssigkühlung zu vereinfachen; dies bedeutet eine Kombination von mikrokanalbasierten Hochleistungsflüssigkühlern und konventionellen Luftkühlern. Effiziente Wärmeverteilung vom Mikroprozessor via absorbierende und dissipative Wärmetauscher wird mittels eines oszillierenden, primären Flüssigkühlkreislauf erstellt. Das Fluid wird über oszillierende Verdrängerpumpen transportiert. Das Flüssigkeitsvolumen ist auf wenige Milliliter beschränkt, um den möglichen Schaden im Fall einer Leckage in Grenzen zu halten. Ein sekundärer Kühlkreislauf, welcher entweder durch herkömmliche Luftkühlung oder aber durch Flüssigkühlung realisiert ist, ist thermisch an den Primärkreislauf gekoppelt.

Die Doktorarbeit liefert eine umfassende Beschreibung des obengenannten Wärmeverteilsystems, wobei die Analyse des Wärme- und Stoffaustausches dieses dynamischen Systems im Mittelpunkt steht. Es werden vorwiegend die charakteristischen Systemparameter wie Frequenz, Fluidhubvolumen und das Design der Mikrokanalstrukturen besprochen. Der sekundäre Kühlkreislauf, welcher die Abwärme mit der Umgebung austauscht, sowie die Verdrängerpumpen werden in pragmatischer Weise behandelt, mit der Absicht, das Leistungsvermögen des primären Wärmeverteilsystems zu untersuchen.

Kapitel Zwei beschreibt einen Modellierungsansatz, welcher es erlaubt, die Effizienz von Mikrokanalkühlern abzuschätzen. Ausgehend von numerischen Modellierungen auf der Basis der Mikrokanalstrukturen, wurde die Leistungsfähigkeit der Einheitszelle ermittelt. Der geschwindigkeitsabhängige Druckverlust als auch der Wärmeübergangskoeffizient für unterschiedliche Porositäten des gewebeartigen Mikrokanalkühlers wurden identifiziert. Weiterführend wurde ein Netzwerkmodell entwickelt, um die Effizienz auf der Ebene des Mikrokanalkühlers abzuschätzen. Die numerischen und analytischen Resultate wurden zudem mit experimentellen Messdaten verifiziert.

In Kapitel Drei wurde eine numerische Simulation durchgeführt, welche den Wirkungs-

grad des gesamten oszillierenden Flüssigkühlsystem untersucht. Die charakteristischen Eigenschaften der Mikrokanalkühler-Einheitszelle für unterschiedliche Aspektverhältnisse wurden in ein vereinfachtes Modell des porösen Materials eingesetzt. Die Abhängigkeit der Systemleistung von Porosität, Frequenz und Fluidhubvolumen wurden untersucht und diskutiert. Dies ermöglichte die Festlegung des Bereichs der Betriebsparameter und eine Abschätzung der maximalen Kühlleistung. Die entsprechenden Schlussfolgerungen beschränken den Frequenzbereich auf $0.5 \leq f \leq 2$ Hz und das relative Hubvolumen auf $1 \leq \bar{A} \leq 1.5$. Frequenzen $f \geq 10$, bei welchen ein deutlich verbesserter Wärmeübergang in einem entsprechenden oszillierenden Flusssystem zu erwarten wären, sind im Rahmen einer realistischen Pumpleistung (z. B. $p < 2$ bar) nicht zu erzielen. Ein grosses Fluidhubvolumen und eine geringe Frequenz erwiesen sich als am Effektivsten. Des Weiteren konnte gezeigt werden, dass die geforderte und entsprechend spezifizierte Kühlleistung massgeblich das Design des Mikrokanalkühlers bestimmt.

Kapitel Vier behandelt die experimentelle Umsetzung der entsprechenden Wärmeverteiler-Technologie. Ein Teststand, welcher die Absorber- und Dissipator- Kühlerplatten, die Verbindungsrohrleitungen, die Verdrängerpumpen beinhaltet, wurde gebaut. Der Hochleistungs-Mikroprozessor wurde mittels Heizer/ Sensor Chip eingesetzt. Die thermischen und fluiddynamischen Betriebsleistungen werden entsprechend zeitaufgelöst und zyklusgemittelt präsentiert. Eine maximale Kühlleistung von der Wärmequelle zum thermodynamischen Grundpotential von 180 W/cm^2 ($\Delta T = 67 \text{ K}$, Pumpleistung 1 W) konnte experimentell nachgewiesen werden. Zwei unterschiedliche Flussmuster, *linear* und *radial*, wurden untersucht. Dabei zeigen sich gewisse Vorteile bei *radial* auf lokalen Stellen auf dem Chip. Insgesamt zeigte aber *linear* die bessere Leistung und weist als System einen geringeren Grad an Komplexität auf.

Kapitel Fünf berichtet von einer experimentellen und numerischen Arbeit mit einem leicht modifizierten oszillierenden Wärmeverteilersystem. Die geometrischen Rahmenbedingungen beziehen sich dabei auf ein existierendes Kühlersystem, welches in einem von IBM's Serversystemen zum Einsatz kommt. Dafür wurde das hermetisch geschlossene Absorber/Dissipator-Wärmeverteilsystem in die Grundplatte eines Luftkühlers integriert. Die effektive Wärmeleitfähigkeit, die Wärmeverteiloptimierung und das Potential zur Bauhöhenreduktion gegenüber einem passiven Kühlsystem werden diskutiert.

Contents

Acknowledgment	iii
Summary	iv
Zusammenfassung	vi
1 Introduction	1
1.1 Background and Motivation	1
1.2 Electronic Equipment Thermal Management Concept	3
1.3 Project Outline and Goals	7
2 Combined Local Microchannel-Scale CFD Modeling and Global Chip-Scale Network Modeling for Electronics Cooling Design	11
Abstract	11
Nomenclature	12
2.1 Introduction	14
2.2 Cold Plate Geometry	16
2.2.1 Experimental Setup	18
2.3 Unit Cell Model Description	19
2.3.1 Flow Resistance Model	20
2.3.2 Convection Model	21
2.4 Finite Volume Simulations	23
2.4.1 Governing Equations	23
2.4.2 Numerical Simulation Procedure	24
2.4.3 Postprocessing	26

2.5	Results and Discussions	27
2.5.1	Numerical Simulations	27
2.5.2	Hydrodynamic Study	31
2.5.3	Heat Transfer Study	33
2.6	Summary and Conclusions	38
3	Numerical Modeling of a Self Contained, Reciprocating Liquid Heat Spreader System	41
	Abstract	41
	Nomenclature	42
3.1	Introduction	44
3.2	Model Description	46
3.2.1	Fluidic Considerations	49
3.2.2	Thermal Considerations	51
3.3	Results and Discussion	56
3.3.1	Variable Frequency f , Fixed Mesh Design V_i	56
3.3.2	Constant Frequency f , Variable Mesh Design V_i	62
3.3.3	Experimental Verification of Simulation Results	65
3.4	Summary and Conclusions	68
4	Experimental Study of a Self Contained, Reciprocating Liquid Heat Spreader System for Low Form Factor Electronics	71
	Abstract	71
	Nomenclature	72
4.1	Introduction: Transition to Liquid Cooling	74
4.1.1	Principle of Operation	76
4.2	Device Fabrication, Experimental Apparatus and Procedure	78
4.2.1	Microchannel Cold Plates: HA & HD	78
4.2.2	Piston Pump Actuators	81
4.2.3	Experimental Setup and Data Reduction	82

4.3	Results and Discussions	85
4.3.1	Fluidic Performance	85
4.3.2	Thermal Performance	87
4.3.3	Oscillating Flow versus Steady Flow	94
4.3.4	Thermal Budget of Single Cooling Components	97
4.4	Summary and Conclusions	98
5	Effectiveness of a Radially Oscillating Liquid Heat Spreading System	101
	Abstract	101
	Nomenclature	102
5.1	Introduction: Transition to Liquid Cooling	103
5.2	RADIOS - Technology	105
5.2.1	Flow Principle and Driving Scheme	105
5.2.2	Spreader Plate Design	106
5.2.3	Test Vehicle Description	108
5.3	Results and Discussions	110
5.3.1	IR Camera Spreader Evaluation	110
5.3.2	Model 1 - RADIOS Spreader Plates	112
5.3.3	Model 2 - RADIOS Spreader Plates + Solid Base	115
5.4	Summary and Conclusions	117
5.5	Outlook	118
6	Conclusions	119
	Bibliography	123

1 Introduction

1.1 Background and Motivation

Over the past twenty years our society has been transforming at an incredible pace with the onset of a new digital era and rapid developments in information technology (IT) and digital communications. Computers and digital communication devices are ubiquitous, and the World Wide Web is accessible to billions of people - at any time of the day. Data centers have mushroomed in the past 10 years with an annual growth rate of 15% [1]. Thus, the energy consumption has risen accordingly, lifting the entire information and communication technology (ITC) industry on equal CO₂ emission terms with the entire aviation industry [2]. The accumulated expenses to operate a data center today, already equals the equipment investment costs [3]. According to IDC [2], in 2008, data center operators worldwide spent \$37 billion on power and cooling. Thus, energy costs are a major economic issue and the demand for more efficient systems is high. Furthermore, with our society becoming more and more ecology-aware, the push towards energy-efficient data centers might grow to a greater extent.

Today's data centers are typically air cooled by employing chillers. Sub ambient air is directed to and across the high performance server modules to maintain the chips below a specified temperature of 85 °C. Mostly, large metal air heat sinks are attached to the microprocessors to decrease the convective thermal resistance. Highly

conductive pastes are employed between solid interfaces. To dissipate the heat of individual components to the air heat sinks, heat conduction slabs, heat pipes, and vapor chambers are typically used. However, these methods are limited to low heat flux devices and small heat transport distances. Overall, air cooling solutions are inefficient and limit the integration density of IT equipment due to its large form factors. The situation is even more severe for blade servers, which are optimized to minimize physical space. Blade modules are typically restricted to the minimum size requirements of a standard 1U server-rack configuration (1U: one rack unit, 19" wide and 1.75" tall), while still having all the functional components to be considered a computer [4], [5]. However, with a continuous increase in power dissipation and/or module integration densification, air cooling reaches its cooling capacity.

In order to provide greater cooling efficiency many IT systems are currently developing and employing liquid cooling systems. Liquid cooling systems are typically more compact relative to similarly rated air cooling systems and have lower power requirements due to the improved thermo-physical properties of liquids as compared to air. From the very first demonstrations to the enhanced packages of today, various microchannel cold plate approaches have been reported resulting in cooling capacities of 350 W/cm² and higher [6], [7], [8], [9], [10]. Owing to the small diffusive path from the solid wall into the fluid, water cooled microchannel heat sinks exhibit high convective heat transfer coefficients.

While effective, liquid cooling systems possess several drawbacks. A reliable implementation of liquid cooling systems in highly parallel and flexible systems such as blade servers is challenging. When using liquid as a coolant, each blade server includes a corresponding blade liquid loop that must connect with an associated rack liquid loop. Furthermore, the system flexibility needs to be guaranteed to interchange individual blade servers during operation. Thus, each blade server typically includes a quick-connect member that fluidly links the blade liquid loop to the rack

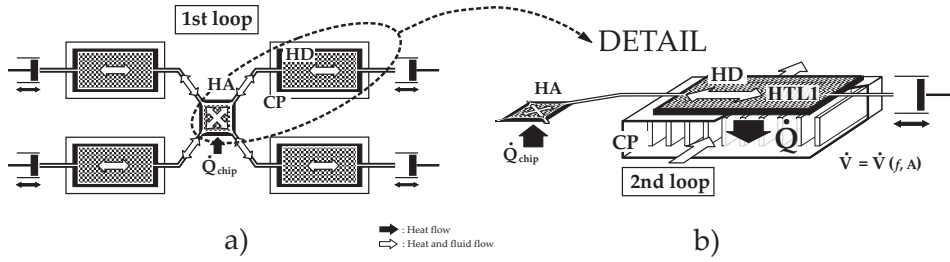


Figure 1.1: Liquid cooling approach for low form factor, blade-type high-performance electronic equipment. A blade-level liquid cooling loop (1st loop) spreads heat from the chip via absorber cold plate (HA) to the large-area dissipator cold plates (HD) in an oscillating manner. The rack-level cooling loop (2nd loop) collects the heat by means of a heat exchanger device (either air or liquid).

liquid loop. Quick-connects represent a potential failure point that may result in fluid contacting electronic components on the blade server. With a typical uniform-flow rate of 0.5 liters/min/blade this raises a scenario with drastic economic consequences. Also, quick connects do not prevent the gradual loss of liquid over time, requiring liquid reservoirs to be refilled. Moreover, an all liquid cooled computing system requires a significant amount of supplementary equipment, such as piping, hoses, and pumping stations. High investment costs are expected when adapting data centers to liquid cooling. Therefore, the IT industry acts rather cautiously in implementing liquid cooling concepts for data center's electronics.

1.2 Electronic Equipment Thermal Management Concept

The technology presented in this thesis examines a novel liquid cooling approach for low form factor, blade-type high-performance electronic equipment, cp. Fig. 1.1. It addresses the effectiveness of liquid cooling by actively spreading the chip waste heat to a large heat transfer area. A blade liquid cooling loop (1st loop) is fluidically separated from a rack cooling loop (2nd loop). The dissipated heat from

the microprocessor is spread to a large heat transfer surface (blade thermal ground plane), which is in contact with an interleaved cold plate (CP) from the rack cooling loop. If the 2nd loop is assembled by conventional computer room air conditioning, a so-called hybrid, liquid-air cooling system is established. No additional installations such as water supply and piping are required. This can be seen as a soft transition to liquid cooling for electronic equipment. Alternatively, the heat spreading concept presented here can also be combined with a rack *liquid* cooling loop, which would be preferred in the case of data center waste heat recovery, e.g. for district heating purposes.

The unique heat spreading concept within the blade liquid cooling loop consists of a self-contained, hermetically sealed, and reciprocating fluid flow system [11], [12]. A small liquid volume in the range of several milliliters is contained in a microchannel cold plate system. Convective heat transfer from the chip to the fluid occurs in the microchannel heat absorber (HA). Periodic linear actuator(s) displace the fluid in an oscillating mode to the heat dissipator (HD) cold plates, where the thermal energy gets dumped via the interleaved cold plates (CP) to the secondary rack-level cooling loop. Each actuator preferably comprises a fluid reservoir and flexible membrane interfacing between an actuation means and the fluid reservoir.

Thanks to the small fluid amount a potential fluid leakage would limit the damage to the electronic devices. Moreover, implementing expensive nano-engineered fluids with superior thermal properties [13], [14] would be conceivable.

In contrast, a uniform-flow forced liquid cooling loop would require a rotary pump. Since the coolant containment is not hermetically sealed a fluid reservoir is also implemented and gradual losses require refilling the system. Figure 1.2 illustrates the basic difference of a blade/rack cooling loop configuration in a) uniform-flow with a rotary pump and b) oscillating flow with reciprocating pumps.

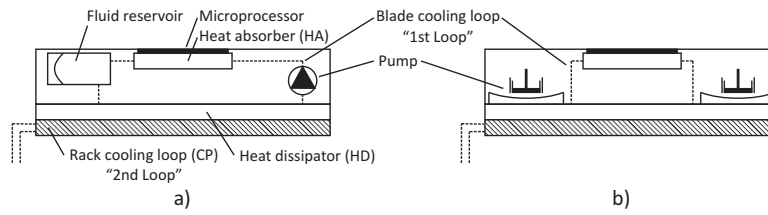


Figure 1.2: Configuration of a blade-level / rack-level cooling system. a) contains a uniform-flow liquid cooling loop using a rotary pump, and b) contains an oscillating liquid cooling loop by means of reciprocating pump(s).

Linearly oscillating flow systems utilize “undeveloped” or plug-like flow profiles for an appropriate frequency and flow rate range. This allows the heat contained in the flow channel to be transported farther along the channel before the heat is absorbed radially. Thus, a higher degree of mass transport is created compared to a parabolic-type flow profile. Furthermore, an undeveloped flow profile enhances the convective heat transfer owing to a lower velocity boundary layer thickness.

The oscillating fluid flow system can be created in a multitude of flow patterns: In a single-phase oscillating flow, cp Fig. 1.3 a), the flow speed between the reservoirs has a sinusoidal flow rate that ranges between zero and some maximum value. Therefore, at least one single displacement actuator is required to create the flow field. This single-phase oscillating flow pattern is simply called *linear*. A two-phase oscillating flow uses four reservoirs that are driven 90 degrees out of phase, cp Fig. 1.3 b). As the flow in the A-A' reservoirs begins to decay to zero, the flow in between the B-B' reservoirs is reaching its maximum value - resulting in a rather constant flow speed and constant higher convective heat transfer. This can be of vital importance with regard to temperature cycling of the microprocessor. For a 3-phase system, cp Fig. 1.3 c), six reservoirs are needed with each of the 3 pairs driven at a 60-degree offset from each other. For the 2 and 3-phase driven flows, at time intervals between those depicted in Fig. 1.3, the flow into and out of the center region will be shared between

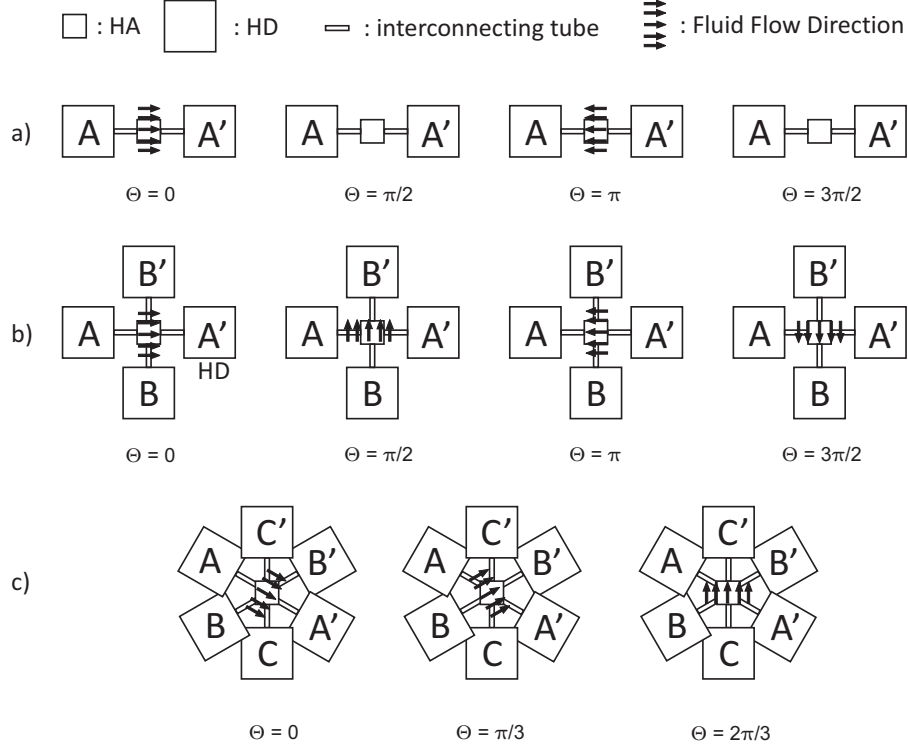


Figure 1.3: Dominant flow pattern of an oscillating heat spreader system. a) describes the single-phase oscillating flow, defined as *linear*, b) (2-phase) and c) (3-phase) create a steady, but radially oscillating flow across the central heat absorber device. This is defined as *radial*.

adjacent reservoirs as the flow rotates radially. This characteristic flow pattern is called *radial*. The benefit of 3-phase and higher systems is a more uniform heat spreading due to the increasing number of reservoirs and smaller entrance and exit opening compared with 2-phase system - however the additional reservoirs with multiple actuators add complexity and cost to the system.

In addition to the benefits of an oscillating fluid flow system delineated above, more opportunities open up for innovative, cost-effective centralized pumping schemes for distributed cooling systems. The basic working principle would be a time variable

pressure in a fluid loop acting on the membranes implemented in the rack of the cold plate. Their deflection is transferred to a second set of membranes in the blade thermal ground plane, which are in close contact with the first set. A time variable pressure can be realized by the modulation of a centralized pressure modulator. Expansion volumes are necessary to displace the fluid in the blade thermal ground plane. They are implemented as membranes or by trapped air in the fluid network.

1.3 Project Outline and Goals

The scope of the thesis is the characterization and development of a self-contained, hermetically sealed, oscillating liquid heat spreader for low-form factor, high performance electronic equipment. With regard to a peak power load of 100 W/cm^2 for conventional air cooling, the thermal load should be doubled (200 W/cm^2) but keeping the microprocessor below the maximum temperature of 85°C (thermal ground potential: 20°C). The thesis provides a thorough characterization of the above delineated liquid cooling heat spreading system. However, the focus lies in the description of the heat and mass transfer within this dynamically-acting heat spreading system. The characteristic measures of frequency and fluid displacement and the design of the mesh-type microchannel cold plates are investigated analytically, numerically, and experimentally. The blade thermal ground plane, which dumps the waste heat to the rack cooling loop, and the fluid displacement pumps are introduced pragmatically with the objective of exploring the performance of the respective liquid heat spreading technology.

Chapter Two describes a methodology accounting for the local as well as device length scales of mesh-type microchannel cold plates. A unit cell stack of the heat transfer microchannel system is modeled and implemented in conjugate CFD simulations. The fluidic and thermal characteristics of three different cold plate mesh

designs are evaluated. Periodic boundary conditions and an iteration procedure are used to reach developed flow and thermal conditions. Subsequently, two network-like models are introduced to predict the overall pressure drop and thermal resistance of the microchannel cold plate based on the results of the unit cell evaluations. Finally, the performance figures from the model predictions are compared to experimental data.

In Chapter Three, a full-system numerical simulation studies the fluidic and thermal performance of the self-contained, oscillating liquid cooling heat spreader system. The characteristic properties of microchannel cold plate unit cells, as described in Chapter Two, are implemented into a simplified porous media model. The resulting time-dependent mass, momentum, and energy equations are solved for the absorber, interconnecting tube, and dissipator devices, which comprise the liquid heat spreader system. The interplay of the fluid volume displacement, the frequency, and the microchannel mesh design on the thermal and fluidic performances are investigated. It also sheds light on the driving range of this highly dynamically-acting liquid-cooling system, facilitating the design specifications and constraints of an experimental assembly.

Chapter Four investigates the experimental realization of the according liquid heat spreader system. Microchannel heat absorber and heat dissipator cold plates are designed and manufactured, and a fully operational system including the displacement pumps and interconnecting tubes is built up. The thermal and fluidic characteristics are presented in a time-resolved and cycle-averaged manner, while a heater/sensor chip is adopted to simulate a high power density microprocessor. The system is configured according to Fig 1.3 b), with one heat absorber and four peripheral heat dissipator cold plates. Correspondingly, four piston-type displacement pumps are implemented. The *linear* and *radial* oscillation flow regimes are established and their assets and drawbacks are discussed in detail.

Chapter Five discusses an oscillating liquid heat spreading system that is geometrically bound to an existing vapor chamber air heat sink device that is implemented in one of IBM's server systems. This study aims at replacing the vapor chamber heat sink base by the self-contained microchannel absorber/dissipator heat transfer. Two different heat transfer mesh layouts are tested to optimize the thermal spreading. The effective conductivity and heat spreading improvement and the thinning potential of the air heat sink base over a passive heat conducting system are numerically and experimentally explored.

2 Combined Local Microchannel-Scale CFD Modeling and Global Chip-Scale Network Modeling for Electronics Cooling Design¹

Abstract

In this paper, a methodology accounting for the local as well as the device length scales of the involved physics is introduced and applied to determine the performance of a microchannel cooler. A *unit cell* of the heat transfer microchannel system is modeled and implemented in conjugate CFD simulations. The fluidic and thermal characteristics of three different cold-plate mesh designs are evaluated. Periodic boundary conditions and an iteration procedure are used to reach developed flow and thermal conditions. Subsequently, two network-like models are introduced to predict the overall pressure drop and thermal resistance of the device based on the results of the *unit cell* evaluations. Finally, the performance figures from the model predictions are compared to experimental data. We illustrate the cooling potential for different channel mesh porosities and compare it to the required pumping power. The agreement between simulations and experiments is within 2%. It was found that for a typical flow rate of 250 ml/min, the thermal resistance of the finest microchannel network examined is reduced by 7% and the heat transfer coefficient is increased by 25% compared to the coarsest channel network. On the other hand, an increase in pressure drop by 100% in the case of densest channel network was found.

¹This Chapter is submitted for publication: R. Wälchli, T. Brunschweiler, B. Michel, D. Poulikakos, “Combined Local Microchannel-Scale CFD Modeling and Global Chip-Scale Network Modeling for Electronics Cooling Design”, *International Journal of Heat and Mass Transfer*, 2009

Nomenclature

A	Elemental <i>unit cell</i> width [mm], or Area [mm ²]
B	Elemental <i>unit cell</i> fin width [mm]
C	Elemental <i>unit cell</i> fin width [mm]
$CMOS$	Complementary metal oxide semiconductor
c_p	Specific heat capacity, 4182 [J kg ⁻¹ K ⁻¹]
DBC	Direct bonded copper
D_h	Hydraulic diameter [m]
FS	Full scale
H	Measure of height [m]
h	Heat transfer coefficient [W m ⁻² K ⁻¹]
L	Measure of length [m]
\mathbf{L}	Translational vector [m]
\dot{m}	Mass flow rate [kg s ⁻¹]
N	Integer number of entities in x -direction [-]
p	Pressure [Pa]
\dot{Q}	Heat flux [W]
R	Thermal resistance [K W ⁻¹]
T	Temperature [K]
u	Velocity component [m s ⁻¹]
V	Volume [m ³]
\dot{V}	Volumetric flow rate [m ³ s ⁻¹]
V_i	Mesh design version, $i=1,2,3$
W	Measure of width [m]
\mathbf{x}	Spatial vector [m]

Greek letters

β	Coefficient of thermal resistance model function [$\text{K s W}^{-1} \text{ m}^{-3}$]
γ	Coefficient of pressure drop model function [Pa s m^{-3}]
δ	Coefficient of pressure drop model function [-]
Δ	Laplace-Operator [-]
ϵ	Coefficient of thermal resistance model function [K W^{-1}]
λ	Thermal conductivity [$\text{W m}^{-1} \text{ K}^{-1}$]
ν	Kinematic viscosity [$\text{m}^2 \text{ s}^{-1}$]
φ	Porosity [%]
ϕ	Coefficient of thermal resistance model function [-]

subscript/superscript

"	area normalized [m^{-2}]
—	mean
0	zeroth node
<i>avg</i>	average value in the center of the flow channel
<i>base</i>	bottom side of cold plate/ <i>unit cell</i>
<i>cd</i>	conductive
<i>cell</i>	pertaining to the <i>unit cell</i>
<i>center</i>	pertaining to the central part of the cold plate
<i>cv</i>	convective
<i>fl</i>	fluid
<i>H₂O</i>	water
<i>inlet</i>	pertaining to the inlet port
<i>n</i>	network index
<i>tot</i>	pertaining to the entire cold plate
<i>void</i>	void space

2.1 Introduction

In bipolar microprocessor technology, liquid cooling of electronics applications has been ubiquitous and highly needed in order to achieve high power dissipation. This situation changed rapidly when the industry switched from bipolar to complementary metal oxide semiconductor (CMOS) chip technology. Due to low heat fluxes of the first chip generations, CMOS microprocessors immediately dropped the need for liquid cooling. However, aligning with Moore's law a continuous increase in power dissipation of high performance computing systems has been taking place. Furthermore, the idea of collecting excess heat from data centers for reuse are expected to leverage low resistance liquid coolers for future thermal packaging solutions [15].

Microchannel cold plates have been demonstrated for the first time by Tuckerman and Pease with a cooling performance up to W/cm^2 [6]. However, manufacturing difficulties, high pressure drop, and cost issues hindered this innovative concept for being implemented in electronics applications. Since the introduction of the flip chip and C4 technology that removed the requirement for wire bonding the entire backside of the die became available for heat removal. Thermal interface materials allow for a low heat flow resistance between the chips and the heat absorber device. Recent backside liquid cooling approaches ([8],[9]) have demonstrated high cooling potential. In Brunschweiler et al. [8] direct water jet impingement with 50'000 nozzles arranged in a hierarchical manner was used to cool the backside of the chip. At a flow rate of 2.5 liters per minute (lpm) and a pressure drop of 0.35 bar a thermal resistance value of $17.0 \text{ K mm}^2 \text{ W}^{-1}$ was reached. However, direct contact of fluid with the microprocessor is delicate and requires advanced sealing and assembling. In the work of Colgan et al. [9], micromachining in silicon was used to build three-dimensional heat transfer structures of the size of $20 \times 20 \text{ mm}^2$. At a flow rate of 1.5 lpm and a pressure drop of 0.4 bar a unit thermal resistance of $15.9 \text{ K mm}^2 \text{ W}^{-1}$

was achieved. A comprehensive study of high heat flux cooling technologies can be found in [16].

High convective heat transfer and low pressure drop is desired in order to meet performance requirements mentioned above. Precise prototyping and mass manufacturing technologies are needed to achieve well controllable and tunable performance figures of such microchannel cold plates. The cold plates studied in this paper utilize a direct copper bonding (DBC) process in order to comply with the requirements mentioned earlier. Copper sheets of 200 μm thickness are patterned by means of lithography and wet etching. A subsequent chemical oxidation process to build a defined copper oxide layer is applied. Finally, the layers are aligned in a stack and are fused at a temperature above the liquidus temperature of the copper oxide but below the solidus temperature of the copper. The result is a copper only and interface free bond due to the interlayer grain growth [17]. By alternating the patterns from one layer to the next, a porous, mesh-like heat transfer cavity with percolation paths can be created. A more detailed description of this technology can be found in [18]. Depending on the geometry and aspect ratio of a *unit cell* of this mesh the devices can be designed towards a particular operation point with respect to pumping power and cooling potential requirements.

In order to allow for fast and reliable engineering of liquid cooling systems, it is important to establish reliable design rules. Hence, fluidic and thermal performance figure estimates of microchannel cold plates are required. This typically implies an optimization of such microchannel cold plates with the correct engineering trade-off between frictional losses and convective heat transfer.

This article proposes a novel and reliable approach to characterize such mesh-type microchannel heat exchangers. The method is based on first solving at the *local level* the conjugate heat transfer problem of a mesh *unit cell* stack with computational fluid dynamics. Employing periodic boundary conditions the computational

domain can be reduced to one *unit cell* stack only. This allows detailed studies and the optimization of heat transfer geometries within acceptable time frames and reasonable computation power. Physical data such as heat transfer coefficients and pressure drop are extracted for a flow rate range of 50 to 500 ml/min. This information can be subsequently used to estimate the performance figures of the entire cold plate device. To this end, a resistor network model for pressure drop analysis and a heat advection/convection model, both at the *device level*, are proposed to calculate the overall fluidic and thermal resistance of the cold plates. The thermal model also accounts for the effect of lateral heat spreading in the base due to the heating of the fluid from inlet to outlet. The model predictions are finally compared to experimental data.

2.2 Cold Plate Geometry

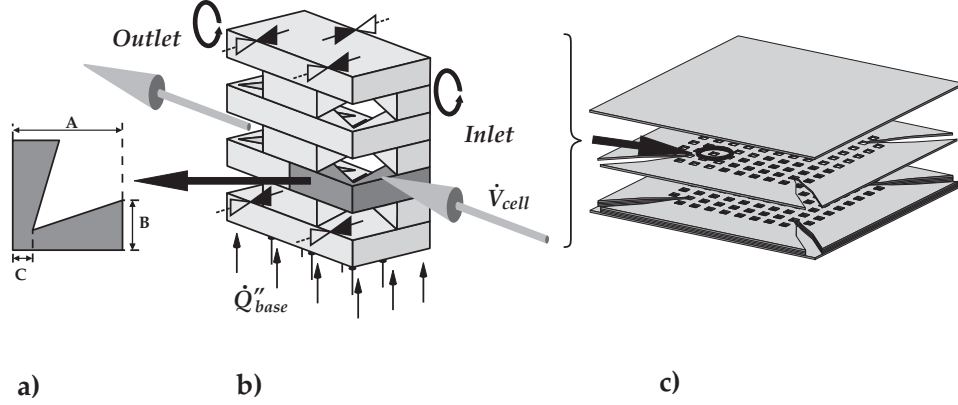


Figure 2.1: Scheme of the microchannel heat transfer mesh. a) represents the elemental unit and b) the entire *unit cell* stack which defines the simulation domain. In c), a scheme of the completed cold plate assembly is shown.

Figure 2.1 describes the geometry of the heat transfer mesh and the layering principle of the entire cold plate respectively. Figure 2.1 a) is the top view of the elemental

unit of the entire heat transfer space. By mirroring and stacking this entity a *unit cell* stack, Fig. 2.1 b), is created. This represents the simulation domain used in this work to calculate the performance quantities like pressure drop and heat transfer coefficient. The entire cold plate assembly is depicted in Figure 2.1 c). Several micromachined sheets of copper foils are piled and finally bonded together to form the entire cold plate. The mesh and cold plate manifold design allow multiple flow directions in a plane, i. e. being rotation-symmetric. This is needed where oscillating/reciprocating fluid flows take place. A potential application for self-contained, oscillating liquid cooling within a confined space is described in [11]. Four opening ports are implemented with tubes attached to the sidewalls of the cold plates. In the present work we are studying steady-state conditions with a continuous flow rate of water entering two ports from one side and leaving from the opposite side. Due to vertical and horizontal direction change of the streamlines a highly curling and tortuous flow profile with a resulting minimal thermal boundary layer can be achieved within the heat exchanger mesh. The geometry presented herein creates multiple flow impingements against the copper posts as it crosses a single cell. High fin efficiencies are therefore expected.

The geometry information of the elemental unit, cp. Fig. 2.1 a), is given in Table 2.1. Three different porosity levels

$$\varphi = \frac{V_{void}}{V_{cell}} \quad (2.1)$$

have been manufactured and modeled in the computational study. By varying the fin thickness B, porosities of 59, 52, and 46% for design *V1*, *V2*, and *V3* are constructed. We decided to adopt a rather coarse porous mesh in order to keep the pressure drop low [19]. Convection dominated heat flow resistance should be reached at flow rates of 400-500 ml/min. For liquid cooling systems this is at the lower bound [8],[9],[16],

however, specifications for low pumping power typically limit the coolant flow rate. Applications of low pressure drop microchannel cold plates for electronics equipment with moderate flow rates are described in [20].

Variable Name		$V1$	$V2$	$V3$
A	[mm]	0.7	0.7	0.7
B	[mm]	0.25	0.3	0.35
C	[mm]	0.06	0.06	0.06
φ	[%]	58.8	52.2	45.7

Table 2.1: Geometry information according to Figure 2.1 of the three different cold plate meshes and the according porosity values.

2.2.1 Experimental Setup

Manufacturing of the DBC microchannel cold plates was realized by Curamik (Eschenbach, Germany). Three samples of each design were characterized with a thermal test setup. The cold plates were attached to a 18.6 x 18.6 mm² test chip with areal resistive heaters and 8 resistive temperature detectors. Thermal connection between the heater chip and the cold plates was established using high performance thermal grease and constant squeeze load. We determined the area thermal resistance of the chip and thermal grease as $1.3 \cdot 10^{-5} \text{ K m}^2 \text{ W}^{-1}$. The flow rate and temperature was controlled by means of a flow rate sensor (Omega FLR 1000, accuracy: $\max \pm 2\%$ FS) and a chiller (Lauda Proline RP 855, $\pm 0.01^\circ\text{C}$ FS). A differential pressure sensor (Omega PD 23, $\pm 0.2\%$) was used to measure inlet-outlet pressure loss. Data points were determined by averaging several hundred measurements read by a LabVIEW program. Uncertainty studies were executed in a standard manner but are not presented in this paper for brevity, since the experiments are not the main topic of this paper. Herein we will focus on the simulation and modeling

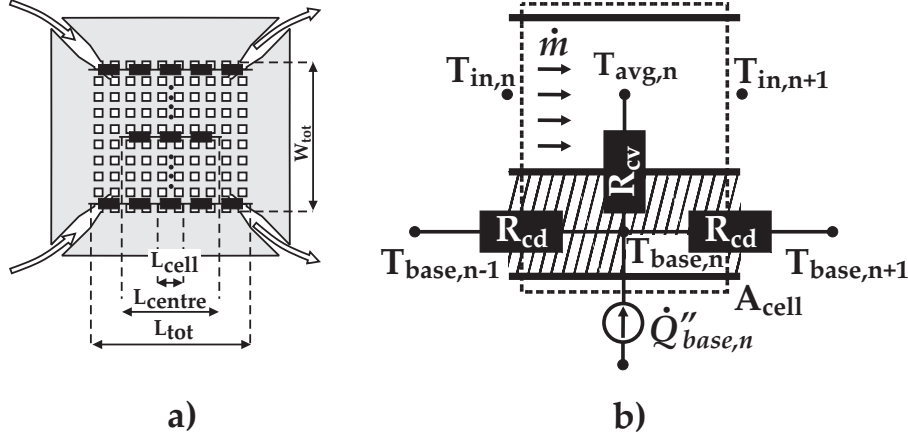


Figure 2.2: Resistor network model to predict the fluidic and thermal performance: a) Shows a group of serially connected fluidic resistor elements, and b) represents the heat advection/convection model of a *unit cell*.

approach for mesh-type microchannel cold plates and simply use the experimental data to confirm the accuracy of the modeling.

2.3 Unit Cell Model Description

The main objective of this paper is to develop a microchannel mesh model combined with a chip level model to estimate the overall fluidic and thermal performance of cold plates. The *unit cell* CFD simulations of the heat transfer mesh will deliver the characteristic values for the flow rate \dot{V}_{cell} , pressure drop Δp_{cell} , and heat transfer coefficient h_{cell} . With this information available, a resistor network model for pressure drop calculations and a heat convection network model for the thermal resistance of the entire cold plate can be used to describe the plate performance.

2.3.1 Flow Resistance Model

Fluid flow resistance of a microchannel cold plate is defined as the relative pressure change from the inlet to the outlet port Δp_{tot} . From the CFD simulations, the *unit cell* pressure drop is expressed as an empirical model function of the flow rate

$$\Delta p_{cell} = \gamma \cdot \dot{V}_{cell}^\delta \quad (2.2)$$

where fully developed flow conditions are assumed. The manner in which this can be derived is explained later in Section 2.4.

Flow resistor networks are efficient and reliable methods to describe the pressure drop of fluidic devices: In a resistor network a change of state of node n affects node $n + 1$ in the same way a change in node $n + 1$ affects node n . Each single resistor element represents a *unit cell* with its corresponding pressure drop Δp_{cell} . Serial connections of resistor elements are assumed to derive the overall pressure drop of the fluid flowing from one side to the next. Here, a straight forward model delivers satisfying results that correlate very well with the experimental data. Due to the particular shape of the cold plates (Fig. 2.1 c)), the number of serial connections is reduced in the center of the mesh area. The fluid resistor network is shown in Fig. 2.2 a). Because of the symmetric shape of the cold plates presented herein, we utilize an arithmetic average number of serially connected *unit cells* to calculate the total pressure drop

$$\Delta p_{tot} = \frac{L_{tot} + L_{center}}{2 \cdot L_{cell}} \cdot \Delta p_{cell} \quad (2.3)$$

where L_{tot} is the full length of the heat transfer mesh area and L_{centre} the shortest flow path within the manifold structures (Fig. 2.2 a). Manifold entrance and exit effects on the overall pressure drop Δp_{cell} are neglected and parallel resistors are assumed in the transversal flow direction. The principle of the resistor network model

can be adapted to any arbitrary shape. Starting from the *unit cell* pressure drop more complex networks can be formulated and solved with corresponding network analysis tools.

2.3.2 Convection Model

Determining the thermal performance of a cold plate the situation is not as straightforward as in the case of the fluidic network model. This has to do with the nonsymmetrical nature of convective heat transfer in an open system. It cannot be modeled by a classical resistor element due to energy transport by enthalpy flows [21]. Our model approach (Fig. 2.2 b) which represents the previously introduced *unit cell* of the heat transfer structure lumps the solid and liquid domains of the mesh into an open channel where the control volume (C.V.) confines the domain of the n^{th} *unit cell*. $T_{in,n}$ and $T_{in,n+1}$ are the inlet and outlet temperature of the n^{th} element. $T_{base,n}$ is the base and $T_{avg,n}$ the average fluid temperature of the n^{th} element. Two energy equations can be formed:

$$\dot{m}_{cell} \cdot c_p \cdot (T_{in,n+1} - T_{in,n}) = \dot{Q}_{cv,n} \quad (2.4)$$

the balance of the change of energy in the fluid from inlet to outlet with the convective heat input into the fluid where

$$R_{fl} = \frac{1}{\dot{m}_{cell} \cdot c_p} \quad (2.5)$$

is referred as the fluidic resistance that occurs due to the temperature rise of the coolant [22]. Another energy equation is formulated at the node in the base of the *unit cell*:

$$\dot{Q}_{cv,n} = \dot{Q}_{base,n} + \dot{Q}_{cd,n+1} - \dot{Q}_{cd,n} \quad (2.6)$$

where $\dot{Q}_{cv,n}$ is the heat transfer between the solid base and the fluid that occurs due to a temperature difference

$$\dot{Q}_{cv,n} = h_{cell} \cdot A_{cell} \cdot (T_{base,n} - T_{avg,n}) \quad (2.7)$$

Regarding resistor elements we define

$$R_{cv} = \frac{1}{h_{cell} \cdot A_{cell}} \quad (2.8)$$

as the convective heat flow resistance between the base node and the average fluid temperature. We assume a constant temperature rise along the fluid channel, therefore

$$T_{avg,n} = \frac{T_{in,n} + T_{in,n+1}}{2} \quad (2.9)$$

In order to allow for heat spreading at the base, conductive terms are included in Eq. 2.6

$$\begin{aligned} \dot{Q}_{cd,n+1} &= \frac{1}{R_{cd}} \cdot (T_{base,n+1} - T_{base,n}) \\ \dot{Q}_{cd,n} &= \frac{1}{R_{cd}} \cdot (T_{base,n} - T_{base,n-1}) \end{aligned} \quad (2.10)$$

where the resistance reads

$$R_{cd} = \frac{L_{cell}}{\lambda_{cell} \cdot W_{cell} \cdot H_{base}} \quad (2.11)$$

A constant heat flux source at the base of the *unit cell* is assumed [23, pp. 477]:

$$\dot{Q}_{base,n} = \dot{Q}_{base,n}'' \cdot W_{cell} \cdot L_{cell} \quad (2.12)$$

The overall thermal resistance of the microchannel cold plate is defined as the ratio of the base to inlet temperature difference and the heat input

$$R_{tot} = \frac{\bar{T}_{base} - T_{in,1}}{\dot{Q}_{base}} \quad (2.13)$$

$T_{in,1}$ and $\dot{Q}_{base} = \dot{Q}_{base}'' \cdot W_{tot} \cdot L_{tot}$ are given as independent variables. We determine \bar{T}_{base} of the entire cold plate by connecting $N = \min \{N \in \mathbb{Z} | N \geq L_{tot}/L_{cell}\}$ serial *unit cell* entities in the flow direction. This assumes uniform fluid flow from inlet to outlet and zero temperature gradients transversal to the flow direction. With Eq. (2.4) and (2.6) a system of linear equations can be formulated for all N cells as

$$\begin{aligned} \mathbf{y} &= \mathbf{A} \cdot \mathbf{x} \\ \mathbf{x} &= [T_{in,1}, \dots, T_{in,N}, T_{base,1}, \dots, T_{base,N}] \end{aligned} \quad (2.14)$$

and the average cold plate base temperature is finally determined as

$$\bar{T}_{base} = \frac{1}{N} \sum_{n=1}^N T_{base,n} \quad . \quad (2.15)$$

From the CFD simulations of the *unit cell*, the heat transfer coefficients h_{cell} can be determined depending on the mesh design version $V1$, $V2$, $V3$ and the mass flow rate \dot{m}_{cell} . This is discussed in detail in the next section.

2.4 Finite Volume Simulations

2.4.1 Governing Equations

For the numerical simulation procedure in the *unit cell* we approached the conjugate heat transfer problem from the bottom surface through the solid into the fluid by solving the three-dimensional continuity, Navier-Stokes, and energy equations in the

fluid and the heat conduction equation solid domain. The equations read:

$$\frac{\partial u_j}{\partial x_j} = 0 \quad (2.16)$$

$$\frac{\partial}{\partial x_j} (\rho u_j u_i) = -\frac{\partial p}{\partial x_i} + \frac{\partial}{\partial x_j} \left(\mu \frac{\partial u_i}{\partial x_j} \right), \quad i = 1, 2, 3, \quad (2.17)$$

$$\frac{\partial}{\partial x_j} (\rho c_p u_j T_{fl}) = \frac{\partial}{\partial x_j} \left(\lambda_{fl} \frac{\partial T_{fl}}{\partial x_j} \right) + \mu \left(\frac{\partial u_i}{\partial x_j} + \frac{\partial u_j}{\partial x_i} \right) \frac{\partial u_i}{\partial x_j} \quad (2.18)$$

$$\frac{\partial}{\partial x_j} \left(\lambda_s \frac{\partial T_s}{\partial x_j} \right) = 0 \quad (2.19)$$

The *unit cell* geometries introduced were created using the commercial software ANSYS ICEM CFD [24]. Three-dimensional finite volumes (hexahedrons) were used to discretize the *unit cell* geometry by specifying the minimum edge length. Finer resolution is provided where larger gradients are expected, i.e. at solid/fluid interfaces. The mesh was transferred to the commercial code ANSYS CFX [25] for flow and heat transfer calculations. A high resolution scheme (second order upwind plus first order for oscillation corrections) was used to calculate the convective terms [26]. A Rhie-Chow formulation is used to avoid pressure-velocity decoupling for pressure based methods [27]. The linearized systems of equations were solved using an algebraic multigrid algorithm. The calculations were terminated when the RMS residual undercut 10^{-5} for all governing equations. Grid independence tests were performed with meshes between 90'000 and 930'000 volume elements. The calculations reported in this paper were performed using approximately 570'000 finite volumes, which deviates from some asymptotic values by 1%.

2.4.2 Numerical Simulation Procedure

A three-dimensional model with solid (copper) and fluid (water) domains is considered (cp. Fig. 2.1) to model steady-state, periodic, laminar, and incompressible flow.

The temperature dependency of the thermophysical properties and radiative heat transfer are neglected. The fluid flow is first solved for adiabatic conditions ($T_0 = 298$ K). We consider a periodic structure between inlet and outlet with a constant translational vector \mathbf{L} with respect to the flow direction. For periodic boundaries the velocity and the pressure at any position \mathbf{x} can be written as [28],[29]:

$$u_i(\mathbf{x}) = u_i(\mathbf{x} + \mathbf{L}) = u_i(\mathbf{x} + 2\mathbf{L}) = \dots \quad (2.20)$$

$$p(\mathbf{x}) - p(\mathbf{x} + \mathbf{L}) = p(\mathbf{x} + \mathbf{L}) - p(\mathbf{x} + 2\mathbf{L}) = \dots \quad (2.21)$$

A fixed pressure drop from inlet to outlet is assigned that controls the mass flow rate through the module, hence, the channel Reynolds number. With this, fully-developed spatial flow conditions are calculated in a single simulation run. Flow profiles at the inlet and outlet can be defined with the appropriate postprocessor. Next, the full solid/fluid domain is simulated with the spatial flow distribution inserted as initial condition. In- and outflow boundaries are now defined as openings with the respective flow profiles. The energy equations are solved for the solid and fluid domains respectively; however, the hydrodynamic conservation equations are suppressed. In order to determine the heat transfer coefficient h_{cell} for the corresponding mass flow rate \dot{m}_{cell} thermally developed conditions are required. These conditions are determined with the following procedure: Starting with a constant inlet temperature $T_0 = 298$ K the *unit cell* temperature field is calculated. The outlet conditions of the first cell are used as inlet conditions for the numerical determination of the temperature field of the second cell. The process is repeated until a thermally developed state is achieved (the heat transfer coefficient approaches a constant value). This sequential approach is computationally efficient and avoids having to guess and solve iteratively for the entire length of the developing region. Thermally developed conditions are determined by observing the temperature rise

of the fluid. Thermally developed conditions are achieved when

$$T(\mathbf{x}) - T(\mathbf{x} + \mathbf{L}) = T(\mathbf{x} + \mathbf{L}) - T(\mathbf{x} + 2\mathbf{L}) = \dots \quad (2.22)$$

2.4.3 Postprocessing

In order to calculate R_{fl} and R_{cv} the mass flow rate \dot{m}_{cell} and heat transfer coefficient h_{cell} need to be determined (cp. Eq. (2.5) and (2.8)). This is achieved using the commercial postprocessor ANSYS CFX-Post. As mentioned earlier, the pressure drop from inlet to outlet is part of the domain boundary conditions. The volume flow rate is therefore identified from the simulation results as

$$\dot{V}_{inlet} = A_{inlet} \cdot \bar{v}_{inlet} \quad (2.23)$$

with \bar{v}_{inlet} , A_{inlet} being the average flow velocity at the inlet boundaries and the cross-sectional inlet area of the fluidic domain. The formulation of the heat transfer coefficient is arbitrary. Different temperature potentials could be taken into account to calculate the convective heat transfer. We adopt a mean temperature approach of the entire domain to calculate the heat transfer coefficient

$$h_{cell} = \frac{\dot{Q}_{base}''}{T_{base} - T_{fluid}} \quad (2.24)$$

with T_{base} , T_{fluid} being the area-averaged base temperature and the volume-averaged fluid temperature in the fluid domain respectively. \dot{Q}_{base}'' is part of the boundary conditions and therefore fixed. The study of the thermally developed flow conditions has been performed by monitoring the temperature rise of the fluid in each *unit cell*. As soon as the conditions of Eq. (2.22) were achieved, the iteration procedure was terminated. The finite volume model presented herein ignores conductive heat fluxes across the boundaries, i.e. adiabatic conditions are assumed.

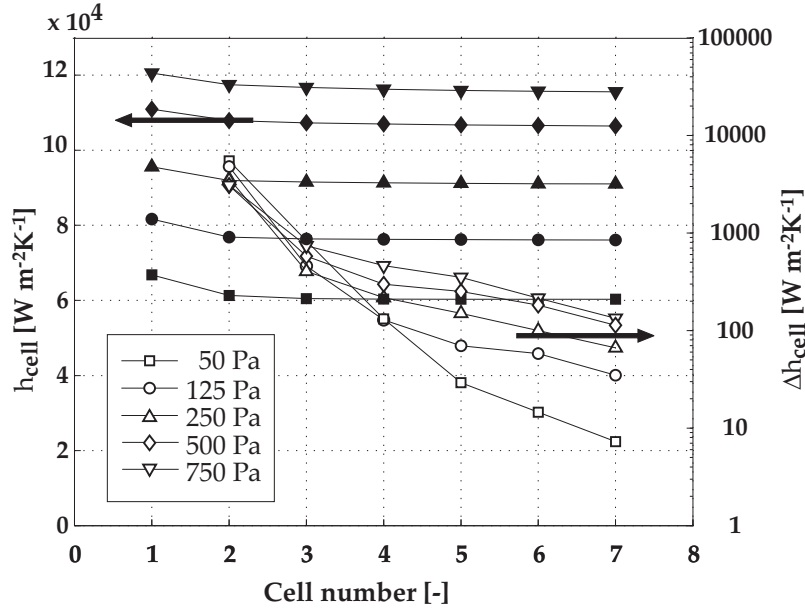


Figure 2.3: Study of the development and transition to steady conditions of the thermal profile depending on the simulation iteration. The left axis shows the heat transfer coefficient (filled markers) for different pressure losses per *unit cell*. The change in heat transfer coefficient of two successive iterations is shown on the right axis (open markers).

2.5 Results and Discussions

The pressure drop across a *unit cell* is chosen such that the extrapolated flow rate for the entire cold plate - see fluidic resistance model in Fig. 2.2 a) - are below 500 ml/min. This is the range the microchannel cold plates are designed for and which is represented by the experimental results. Therefore, each design *V1*, *V2*, and *V3* was simulated with five different pressure values.

2.5.1 Numerical Simulations

Since the velocity profile is determined via periodic boundary conditions, we calculate the developed flow conditions in a single simulation run. Several iterations need

to be executed in order to calculate h_{cell} (cp. Eq. (2.24)) for thermally developed conditions. Figure 2.3 shows the development of the heat transfer coefficient of the channel mesh V1 for different pressure drops depending on the iteration number. h_{cell} is highest after the first iteration since the thermal boundary profile is not yet developed (entrance region effects) but it quickly reaches an asymptotic value. The change of the heat transfer coefficient $\Delta h_{cell} = h_{cell,n} - h_{cell,n-1}$ is shown on the right y-axis. We decided to abort the iteration procedure Δh_{cell} as soon as

$$\Delta h_{cell} \approx 100 \text{ [W m}^{-2} \text{K}^{-1}] \quad (2.25)$$

For all flow rates simulated this is attained after maximum seven iterations. The lower the flow rate, i.e. the smaller the pressure drop, the sooner condition Eq. (2.25) can be reached. Pressure drops per *unit cell* for V1 from 50 to 750 Pa vary the heat transfer coefficient h_{cell} from 60'000 to 115'000 W m⁻²K⁻¹. In Figure 2.4 a) the pressure drop (left y-axis) and heat transfer coefficient (right y-axis) for the three different designs V1, V2, V3 are presented as functions of the flow rate per *unit cell*. The pressure drop follows an exponential behavior. Since the transition from V1 to V3 refines the microchannel copper mesh, the pressure drop increases for any given flow rate. For an arbitrary flow rate of 10 ml/min this leads to a pressure drop of 550, 800, and 1000 Pa for V1, V2, and V3, respectively, i.e. roughly double the pressure loss for mesh design V3 compared to V1.

Convective heat flows are represented in terms of the heat transfer coefficient h_{cell} as defined in Eq. (2.24). For the range of the flow rates investigated, the heat transfer coefficient varies typically by a factor of two, e.g. from 60'000 W m⁻² K⁻¹ for 2 ml/min to 120'000 W m⁻² K⁻¹ for 12 ml/min. Furthermore, the various designs show a significant change in convective performance for a given flow rate. At 10 ml/min fluid flow rate per cell, heat transfer coefficients of 108'000, 122'000, and 135'000 W

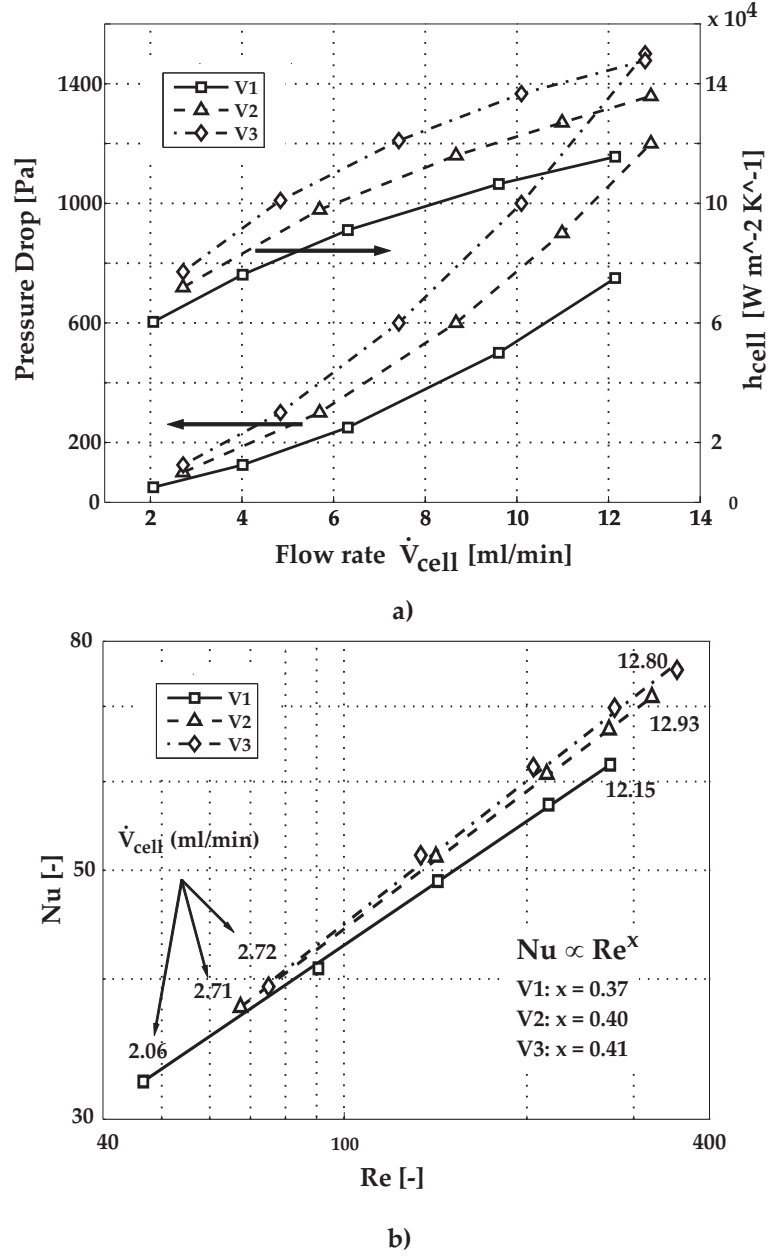


Figure 2.4: Numerical simulation results of the *unit cell* for the three different designs V1, V2, and V3 after fluidic and thermally steady conditions are reached: a) Shows the pressure drop and heat transfer coefficient per cell, and b) characterizes the *unit cells* in terms of Re and Nu .

$\text{m}^{-2} \text{K}^{-1}$ can be observed for $V1$, $V2$, and $V3$. This meets a relative performance increase of 13 and 25 % from $V1$ to $V2$ and $V1$ to $V3$, respectively. Obviously, the finer the heat transfer mesh the higher heat transfer, but at the expense of higher frictional losses. The assumption of a uniform temperature distribution within the solid part of the *unit cell* stack can be verified with the help of the dimensionless Biot number [23, pp. 244]:

$$Bi = \frac{h_{cell} \cdot L_{cell}}{\lambda_{Cu}} \quad . \quad (2.26)$$

With $Bi < 1$ for the entire flow range presented here the lumped capacity model can be legitimated and the error is assumed to be not decisive. A more general base of comparison for the hydraulic characteristics can be performed using the Reynolds number

$$Re = \frac{\bar{v}_{inlet} \cdot D_h}{\nu_{H_2O}} \quad (2.27)$$

With \bar{v}_{inlet} and ν_{H_2O} being the average flow speed (cp. Eq. (2.23)) and the kinematic viscosity of the fluid. In Eq. (2.27), the hydraulic diameter D_h is defined as

$$D_h = \frac{2 \cdot W_{inlet} \cdot H_{inlet}}{W_{inlet} + H_{inlet}} \quad (2.28)$$

with $W_{inlet} = A - B$ (cp. Fig. 2.1 a) and $H_{inlet} = 200\mu\text{m}$ being the width and height of the cell inlet opening into the *unit cell* stack. A commonly used measure to identify the thermal performance of a heat exchanging device is the dimensionless Nusselt number defined as:

$$Nu = \frac{h_{cell} \cdot D_h}{\lambda_{H_2O}} \quad (2.29)$$

In Fig. 2.4 b) the dependence of the Nusselt number on the Reynolds number for the three different designs is shown. The flow rates are indicated next to the simulation data points and correlate with the plot on the left side, Fig. 2.4 a). The assumption of a laminar flow regime is confirmed. For a given flow rate, the

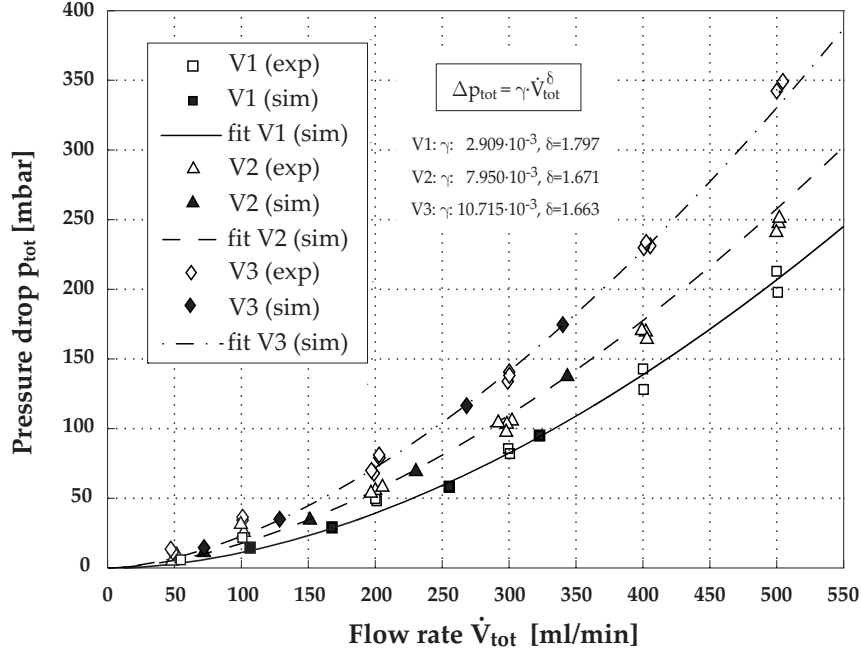


Figure 2.5: The overall pressure drop is calculated according to the fluidic network model presented here, and fitted with a simple power law. The experiments show a very good agreement with the physical modeling.

coarse mesh has the lowest flow velocity \bar{v}_{inlet} and the largest hydraulic diameter D_h . Therefore, the Reynolds numbers of *V1* and *V3* differ between 0 to 18% for the flow range presented. The heat transfer of the densest mesh design *V3* exhibits the best performance values. The slope of the plots in Fig. 2.4 b) represents an exponential dependency between Re and Nu . Results of competing devices show similar values for the corresponding flow rates [30].

2.5.2 Hydrodynamic Study

The results of the application of the fluid resistance model from the simulated pressure drop/flow rate behavior is shown in Fig. 2.5. The coefficients γ, δ of the power fit are listed in Table 2.2. The two model parameters, the cold plate total length

L_{tot} and cold plate inner length L_{center} in Eq. (2.3) are 18.6 mm and 14 mm, respectively. Especially for L_{center} an arbitrary value has been chosen in order to match the experimental results. Depending on the geometry of the heat transfer space the model parameter L_{center} has to be adapted accordingly. Usually, manifold structures are implemented outside the heat transfer area and the fluid flows uniformly from left to right over the entire width of the cold plate. In this case, the fluid resistance model would be a constant number of serially connected resistor elements across the entire cold plate. In Fig. 2.5 the fluid resistance model data are compared to the experimental data. A highly satisfactory agreement is reached in the middle to high fluid flow range (200-500 ml/min). The model data matched the experimental measurements within 5%. In turn, the experimental data shows markedly higher pressure drop in the very low flow range. However, this is of little relevance since the overall characteristics of the pressure loss in the cold plate are well predicted in the flow range of interest.

Variable Name		$V1$	$V2$	$V3$
γ	$[Pa \cdot s \cdot m^{-3}]$	2.909e-3	7.950e-3	10.715e-3
δ	$[-]$	1.797	1.671	1.663
β	$[K \cdot s \cdot W^{-1} \cdot m^{-3}]$	10.510	9.079	8.814
ϕ	$[-]$	0.902	0.865	0.856
ϵ	$[K \cdot W^{-1}]$	0.050	0.042	0.036

Table 2.2: Coefficients of the model fit functions described in Eq. (2.2) and (2.30) for the three cold plate heat transfer meshes.

The relative difference between the three designs is similar for all these designs $V1$, $V2$, and $V3$. This leads to the first conclusion that the simulation/modeling

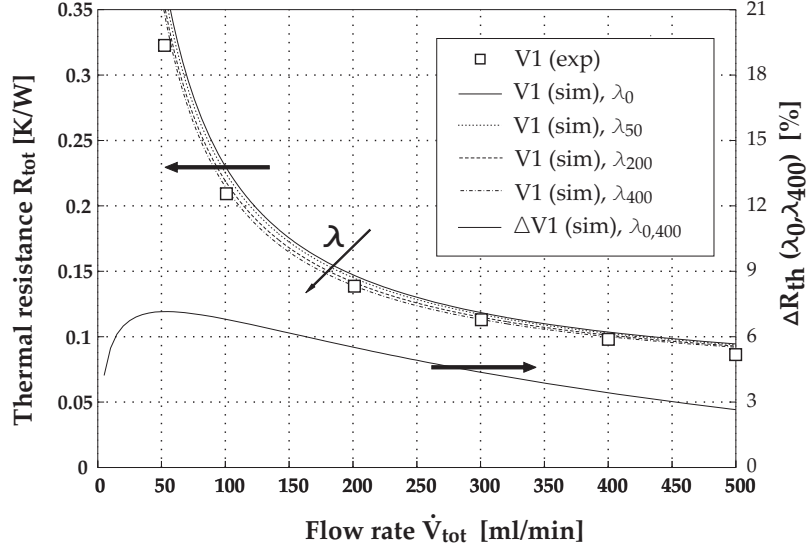


Figure 2.6: The effect of lateral conduction in the base of the cold plate is studied by varying the effective conductivity coefficient λ . The overall thermal resistance is shown on the left side and the relative improvement of λ_{400} over λ_0 is shown on the right axis.

approach works well to estimate the hydrodynamic performance of the microchannel cold plate. However, deviations need to be considered at the boundaries of the fluid flow range investigated.

2.5.3 Heat Transfer Study

Next, we discuss the model presented in Fig. 2.2 from a thermal standpoint. The numerical simulation as it is described above does not account for heat conduction across the boundaries of the solid domain. However, down-stream in the channel the fluid heats up and temperature differences between the inlet and outlet of the cold plate exist. A temperature gradient would be expected in the solid base of the heat sink. Especially for low flow rates where larger convective and fluidic resistances (R_{cv} , R_{fluid}) occur, the overall thermal performance might deviate from

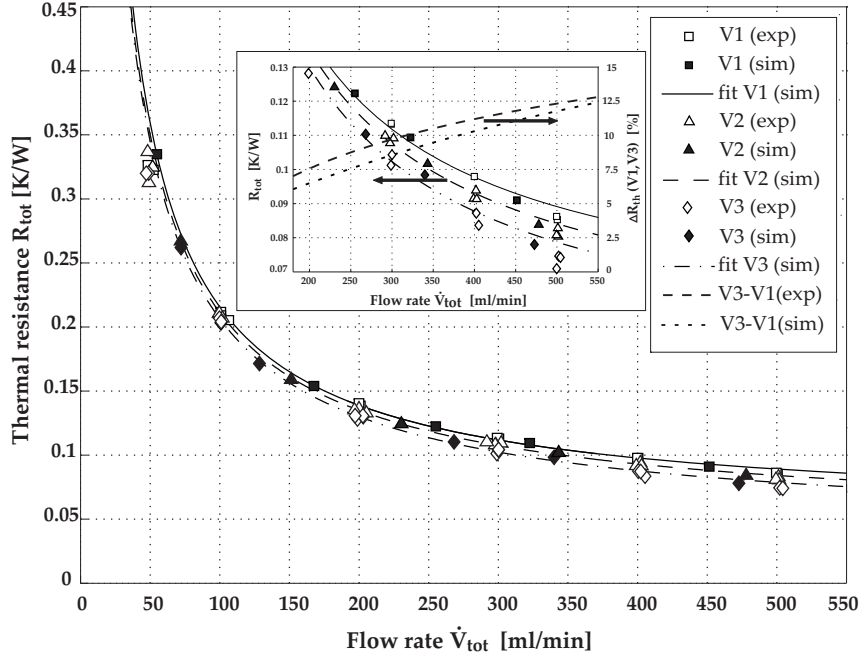


Figure 2.7: Overall thermal resistance as a function of the fluid flow rate. The insert gives a closer view of the thermal resistance (left axis) and compares the relative difference between design *V1* and *V3* for both the modeling and experimental results (right axis).

the experiments. The average base temperature \bar{T}_{base} (cp. Eq. (2.3.2)) would be too high if heat conduction in the solid was omitted in this plate. Therefore, conduction resistances are inserted in the heat transfer model presented in Fig. 2.2b). The effect to the overall thermal resistance is shown in the plots in Fig. 2.6 (left y-axis). The effective conductivity λ_{base} varies stepwise from 0 to $400 \text{ W m}^{-1} \text{ K}^{-1}$. Since copper is used as the solid material $\lambda_{base} = 400 \text{ W m}^{-1} \text{ K}^{-1}$ is the most realistic number to be implemented. As expected, the base heat conduction plays a more significant role at lower flow rates, e.g. $\dot{V}_{tot} < 100 \text{ ml/min}$. Biot numbers between 0.2 and 0.5 for low and high flow rates respectively, corroborate the assumption of a lumped capacity model as introduced in this paper. In order to illustrate the effect of conduction, the

difference between two extreme situations $\Delta R_{th} = R_{th,\lambda=400} - R_{th,\lambda=0}$ is shown in Fig. 2.6 (right y-axis). The thermal resistance performance differs from 0.3 to 0.03 K/W in the flow range presented here. Comparing the two extreme cases, $\lambda_{base} = 0$ and $\lambda_{base} = 400 \text{ W m}^{-1} \text{ K}^{-1}$, the difference in thermal resistance is 7% for low flow rates and 3% for high flow rates. This provides useful information about the heat spreading behavior in a microchannel cold plate. A comparison of the model data with the measurements shows that $\lambda_{base} = 400 \text{ W m}^{-1} \text{ K}^{-1}$ gives the best agreement. The convection model predicts the thermal performance of the experimental data with a deviation below 10% for all data points. However, in order to estimate the performance at moderate flow rates (e.g. $> 200 \text{ ml/min}$) the base spreading can be disregarded completely. With $R_{cd} = \infty$ the thermal model becomes simpler and the average base temperature can be solved explicitly.

Next, we compare the thermal performances of the different microchannel cold plate designs. In Fig. 2.7 the simulation results for all three cases $V1$, $V2$, and $V3$ are shown as a function of the total fluid flow rate. Additionally, the performance figures of the experiments are presented. In order to account for the thermal losses in the chip and the thermal grease, the data from the measurements ($0.13 \text{ K mm}^2 \text{ W}^{-1}$) are added as a constant, serial resistor element. First, a good agreement between model and experiment is evident. This is the case for each design at any flow rate. Low flow rates causing high thermal resistance values lead to insignificant performance variations between $V1$, $V2$, and $V3$. This can be seen either from the measurements or the simulations. At higher flow rates the difference becomes more significant. In order to describe the thermal performance characteristic with an algebraic function the following power-dependent ansatz has been used:

$$R_{tot} = \beta \cdot \dot{V}_{tot}^{-\varphi} + \varepsilon \quad (2.30)$$

This is physically justifiable as follows: for developing or jet flows it usually holds $Nu \propto Re^x, x < 1$ ([23], pp. 489). Recalling the definition of the convective resistance Eq. (2.8) the exponent of the power function must be negative. The symbol ε represents the one-dimensional conduction resistances in the substrate, thermal interface and base of the cold plate. A left-shift of the fitted curves would be effective in representing the parallel heat path through conduction to the board and natural convection to the ambient. Since forced convection is dominating this value is very low and can be neglected. The coefficients $\beta, \varphi, \varepsilon$ for the three different designs are listed in Table 2.2.

The inset graph in Fig. 2.7 gives a closer view of the total thermal resistance in a narrower flow range. The solid line on the right vertical-axis in this graph records the performance improvement of $V3$ over $V1$. For 200 ml/min an improvement of 6% is found while at 550 ml/min design $V3$ surpasses $V1$ by 12.5%. Design $V2$ places in between. From a thermal perspective, the only difference between the different designs arises from varying heat transfer coefficients. As illustrated in Fig. 2.4a) the heat transfer coefficients differ by 25% at 250 ml/min. In turn, this leads to an overall performance improvement of 7%. For the experimental data, the same metric is represented by the short-dashed line on the right vertical-axis of the inlet graph. Deviations between modeling and experiments are less than 2 %. This is another clear indication that the heat convection model predicts the thermal performance of the microchannel cold plates in a highly satisfactory manner. At this point it is worth mentioning that the heat transfer area and the heater chip area are approximately the same. Therefore, the spreading effect that occurs from source to sink is less significant [31].

A reduction of porosity by narrowing the fluid flow channels leads to an improvement of the thermal performance. At a fixed flow rate higher velocities occur and, therefore, the convective heat transfer increases. However, for a heat exchanger design

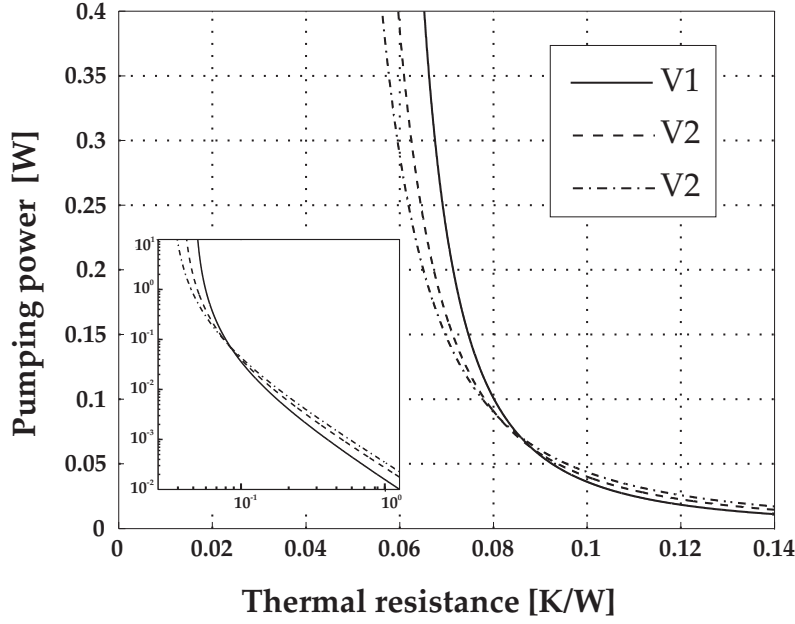


Figure 2.8: The pumping power requirement in order to achieve a given thermal performance for different cold plate designs: Higher flow rate and pumping powers are needed for lower thermal resistance targets.

thermal measures must be weighed against the required pumping power to meet a certain performance. To this end, we calculate the pumping power at various flow rates for the different designs as

$$\dot{W} = \Delta p_{tot} \cdot \dot{V}_{tot} \quad [W]. \quad (2.31)$$

In Fig. 2.8 the pumping power of the cold plates is plotted against the overall thermal resistance for a range of interest (0.06-0.14 K/W). In the case of the cold plates presented in this paper, at performance measures down to 0.1 K/W, the high porosity, low pressure drop design *V1* is preferable. Below this value, the R_{tot} of *V1* reaches an asymptotic regime where the required flow rate, i.e. pressure drop, increases exponentially. Therefore, the low porosity design *V3* becomes more

efficient in terms of pumping power. Depending on the cooling performance required, either a low pressure drop and low thermal performance design *V1*, or a high pressure drop and high thermal performance design *V3* may be preferable.

2.6 Summary and Conclusions

We have shown that a simplified flow resistor network combined with a detailed local convection model can predict well the hydrodynamic and thermal performance of a microchannel cold plate. Three different designs were implemented with a constant pitch but variable channel-to-wall ratio. Periodic boundary conditions were used to determine the steady-state flow field. In addition, an iterative approach was implemented in order to evaluate the steady-state temperature distribution in the *unit cell* stack. Local convective heat flow measures and pressure drops were calculated. Heat transfer coefficients up to $135'000 \text{ W}\cdot\text{m}^{-2}\cdot\text{K}^{-1}$ and pressure drops of 1000 Pa at 250 ml/min were determined.

With this information available, the total pressure drop and thermal resistance was calculated using the corresponding model approaches. For the pressure drop network model, the *unit cell* pressure losses were defined as a flow resistance element and such elements were connected serially. A heat transfer model determined the heat flows occurring laterally by conduction and vertically into the open fluid channel by convection. Again, a serial connection of thermal models accounts for the impact of neighboring entities. A linear system of energy-balance equations was formulated and the cold plate thermal resistance was calculated.

For a flow rate of 250 ml/min the pressure drop doubled while the heat transfer coefficient increased by 25% with the densest mesh geometry, compared to the coarsest. Modeling of base heat conduction is important for low flow rates. However, the complexity of the model can be reduced by omitting lateral conduction. This sim-

plification still delivers good accuracy at high flow rates.

Finally, we compared the model results with experimental data. To this end, we reproduced the microchannel cold plates with the exact same mesh geometry as in the simulations. The pressure drop and thermal resistance at uniform flow conditions with water as the coolant were measured. A very good agreement between modeling and experiments was demonstrated, i.e. relative deviations of max. 2%. We conclude that the modeling approach presented in this paper predicts the thermal and fluidic performance of a microchannel cold plate in an accurate manner. Furthermore, this paper offers the opportunity to limit the complexity of a three-dimensional CFD model to the modeling of only the *unit cell* stack of heat exchanging meshes. This keeps the required computing power at a reasonable level and allows parametric study and optimization of microchannel heat exchanger mesh geometries.

3 Numerical Modeling of a Self Contained, Reciprocating Liquid Heat Spreader System¹

Abstract

An efficient numerical modeling approach is demonstrated to predict the performance of a self-contained, reciprocating liquid cooling system for low form factor electronics. The mesh heat transfer structures involved are described in an averaged sense as fluid-saturated porous media, which is represented with a velocity-dependent permeability κ and a heat transfer coefficient h . The resulting time-dependent mass, momentum, and energy equations are solved for the absorber, interconnecting tube, and dissipator devices, which comprise the liquid heat spreader system. We present the interplay of pump displacement \bar{A} , frequency f , and microchannel heat transfer mesh design Vi on the thermal and fluidic performances. From a pumping power perspective, large displacement and low frequency is beneficial and a relative displacement $\bar{A} > 1$ is a minimum requirement. However, frequencies $f > 1$ Hz are needed to keep the heat source temperature oscillations, e.g. microprocessor junction, below 2 K ($\dot{q}_{in} = 100$ W/cm²). A maximum power load of 600 W can be reached ($\Delta T = 65$ K, $A_{chip} = 15 \times 15$ mm²). We discuss an optimum heat transfer mesh design as a function of the peak cooling performance demand.

¹This Chapter is submitted for publication: R. Wälchli, T. Brunschweiler, B. Michel, D. Poulikakos, "Numerical Modeling of a Self Contained, Reciprocating Liquid Heat Spreader System for Electronics", *International Journal of Heat and Fluid Flow*, 2009

Nomenclature

A	Area [m ²]
\bar{A}	Relative fluid stroke [-]
C_p	Thermal capacity [J kg ⁻¹ K ⁻¹]
D	Diameter [m]
f	Frequency [Hz]
F	Body force [Pa/m]
h	Heat transfer coefficient [W m ⁻² K ⁻¹]
H	Height [m]
L	Length [m]
p	Pressure [Pa]
P	Power [W]
\dot{q}	Heat flux [W/m ²]
R	Thermal resistance [W mm ² K ⁻¹]
t	Time [s]
T	Temperaure [K]
\mathbf{v}	Intrinsic pore velocity [m/s]
$\bar{\mathbf{v}}$	Darcy velocity [m/s]
V	Volume [m ³]
V_i	Heat transfer mesh design, $i = 1, 2, 3$
W	Width [m]
X	Linear factor [-]

Greek letters

φ	Porosity [-]
κ	Permeability [m ²]
λ	Thermal conductivity [W m ⁻¹ K ⁻¹]
μ	Dynamic viscosity [Pa s]
ρ	Density [kg/m ³]
ω	Angular frequency [rad/s]

Ω	Simulation domain
$\delta\Omega$	Simulation domain boundary
Δ	Laplace operator, or Delta
∇	Nabla operator
τ	Thermal time constant [s]

subscript/superscript

0	Total, amplitude
<i>amb</i>	Ambient
<i>chip</i>	Microprocessor chip
<i>Cu</i>	Copper
<i>cycle</i>	Oscillation cycle
<i>eff</i>	Effective
<i>fluid</i>	Liquid matter
<i>H₂O</i>	Water
<i>HA</i>	Heat absorber cold plate
<i>HD</i>	Heat dissipator cold plate
<i>in</i>	Inflow direction
<i>j</i>	Chip junction
<i>max</i>	Maximum value
<i>out</i>	Outflow directin
<i>PM</i>	Porous media
<i>pump</i>	Fluid pump
<i>rms</i>	Root mean square
<i>Si</i>	Silicon
<i>solid</i>	Solid matter
<i>TIM</i>	Thermal interface material
<i>th, thermal</i>	Thermal measure
<i>tube</i>	Interconnecting tube
<i>Vi</i>	Mesh design Vi

3.1 Introduction

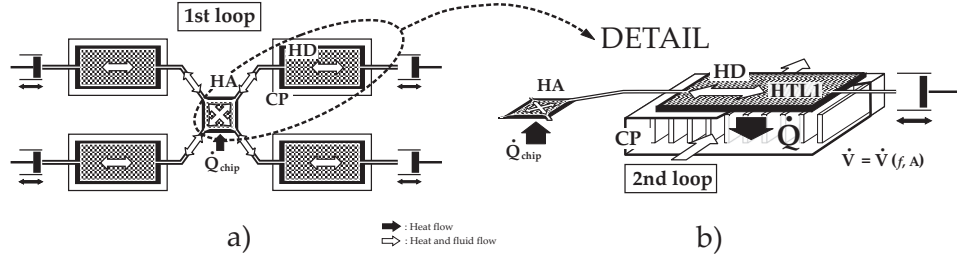


Figure 3.1: Description of a self-contained, reciprocating microchannel liquid cooling device. a) Displays a typical configuration of the devices that represent the primary heat transfer loop inside electronic equipment. b) Illustrates the heat (black arrows) and fluid flows (white arrows) inside the primary transfer loop and the coupling to the secondary heat transfer loop.

With a continuative increase in system integration and densification of electronic equipment, the information technology industry is in dire need of advanced thermal packaging approaches. Furthermore, with the microprocessor power dissipation growing steadily, traditional air cooling will reach its limit in the near future [32], [33]. Especially for low form factor, high-performance computing systems, e.g. blade server modules, the thermal management is becoming problematic. Financially, the expenses to operate a data center today already equal the equipment investment costs [3], [34]. High power air-moving devices blow subcooled air across the blade to absorb thermal energy. Large volume air heat exchangers are used to augment the active heat transfer area and in order to increase the cooling performance. However, the available space for solid-to-air heat exchangers is limited. Since passive heat spreading technologies, e.g. heat pipes and vapor chambers, are restricted in the dispersion area, heat removal has to occur in close vicinity to the microprocessor(s). Unpopulated regions within the electronic device can't be utilized for heat transfer due to the described limit in passive heat spreading.

We introduce a self-contained, blade-level, liquid-flow heat spreading system that addresses the above mentioned challenges as follows, Fig. 3.1: a high performance microchannel cold plate (heat absorber, *HA*) absorbs heat from the electronic component and shuttles it by means of reciprocating fluid oscillations to large area heat dissipator cold plates (heat dissipators, *HD*), positioned in the periphery. Tubes provide a fluid connection between the central *HA* and the peripheral *HD*'s. The oscillating fluid flow is established using hermetically sealed reciprocating pumps with a specific stroke and frequency. A suitable low form-factor pump consists of a membrane-type, axisymmetric magnetic actuator attached to a fluid container via a flexible membrane, e.g. a corrugated copper-beryllium (CuBe) sheet.

Within a pump cycle, the working fluid takes up heat from the source in the *HA*, shuttles it to the peripheral *HD*'s, exchanges it with a secondary heat transfer loop (air or liquid) and returns again cooled to the *HA*. The main advantage of the proposed cooling concept arises from the high heat spreading effectiveness due to high convective heat transfer rates of the microchannel liquid cold plates. The waste heat of the microprocessors can be distributed and directed easily since it is transported in a liquid (e.g. water has a 4000X higher heat capacity per volume compared to air). Therefore, unpopulated regions within a highly packed device such as a blade server can be addressed. Furthermore, the heat spreading system described herein contains a very small amount of liquid, being in the range of a total of 10 - 15 ml. In case of a leakage, the damage to the computer system would be limited to a single blade, but not the entire rack or even the data center. With the primary heat transfer loop (1st loop, cp Fig. 3.1) assigned to spread the heat to a large area inside the electronic equipment, a secondary heat transfer loop (2nd loop) conducts the excess heat to the thermodynamic ground potential (usually the atmosphere). This can be done with either a conventional air conditioning concept by using finned air heat sinks or another liquid cooling loop that collects the heat from each individual

server module and, ideally, makes use of it in the sense of heat recovery (e.g. domestic heating). In that case, a thermal bus system would be required on the top side of the blade server module that establishes an ideal thermal connection between the primary and the secondary heat transfer loop. Experimental work on a similar liquid cooling system is described in [35].

By means of a numerical model, we are investigating the impact of the driving parameters on the fluidic and thermal performance of the above described reciprocating fluid flow system. Additionally, microchannel heat transfer structures with different porosities are implemented and the choice of the optimal design is discussed to meet the specifications. The scope of this work is to illustrate the characteristic behavior of this dynamic cooling system and to predict performance figures thereof. The physical system is reduced to two dimensions, with the microchannel cold plate regions defined as liquid-saturated porous media and the interconnecting tubes as a parallel plate free flow configuration. Analytical solutions of fully developed flow in porous media either on the basis of the Darcy model or on the Brinkman extended Darcy equation can be found in [36], [37], and [38]. Transient forced convection in a fluid-saturated porous-medium layer is presented in [39]. Fundamental numerical work on forced convection through porous media was performed by [40] and [41]. Numerical and experimental work on thermal transport in open-cell metal foams used as high performance heat exchangers are presented in [42], [19], [29], [30], [43].

3.2 Model Description

Figure 3.2 illustrates the simulation domain being considered in this work. It consists of one heat absorber device (*HA*) in the center and two adiabatic tubes, which connect to two dissipator devices (*HD*) on the left and on the right. The fluid chan-

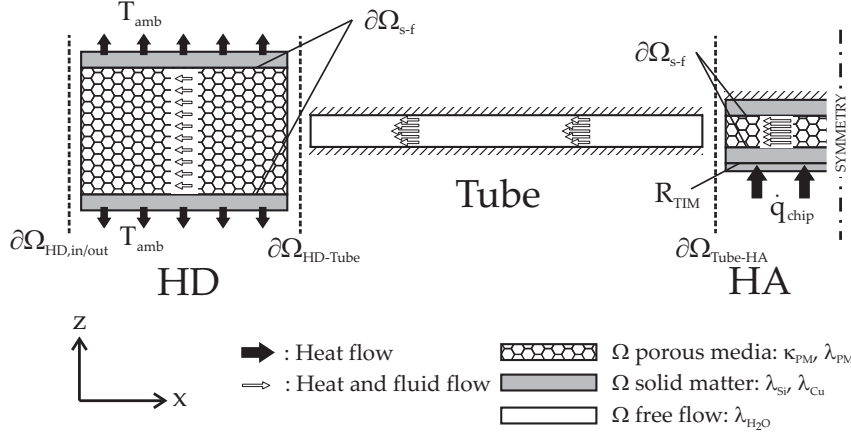


Figure 3.2: Simulation domain of the 2D CFD model (symmetric arrangement). Heat and fluid flows are calculated within the main system components (*HA*, *Tube*, *HD*) by means of porous media, solid matter, and free flow subdomains.

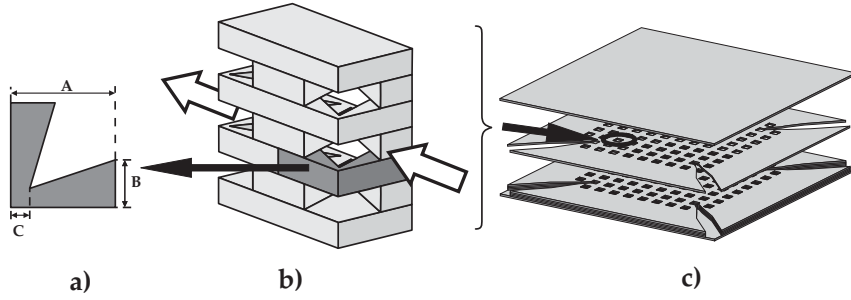


Figure 3.3: Description of the mesh-type microchannel cold plate. By mirroring and stacking the unit cell a), a unit cell *stack* is established b). The duplication of this unit cell stack in series and parallel creates the microchannel cold plate c).

nel structures in the heat exchangers (HA , HD) are described as water-saturated porous media and the interconnecting tubes allow for free flow. The reference microchannel heat transfer mesh is built up from a unit cell presented in Fig. 3.3 a). By mirroring and layering, a unit cell stack is established, cp. Fig 3.3 b), which is duplicated laterally to build up the entire microchannel cold plate, cp. Fig 3.3 c). Different mesh densities are obtained by varying the measure of B , cp. Fig. 3.3 a), which represent the fin thickness. The measures of $A = 700 \mu\text{m}$, and $C = 60 \mu\text{m}$ are kept constant for all microchannel heat transfer meshes presented in this paper. The porosity values of the microchannel cold plates are in the range of $\varphi_{V1} = 0.55$ ($B_{V1} = 0.25 \mu\text{m}$), $\varphi_{V2} = 0.50$ ($B_{V2} = 0.30 \mu\text{m}$), and $\varphi_{V3} = 0.45$ ($B_{V3} = 0.35 \mu\text{m}$). The microchannel heat transfer mesh has been modeled and characterized in detail in Chapter 2 [35].

The work presented in this paper consists of a reproduction of the real three-dimensional cooling device geometry [44] and the flow and heat transfer calculation with a CFD model, cp. Fig. 3.2. As a reference, the three-dimensional cooling device is described to be as follows: the absorber cold plate has the dimensions of $20 \times 10 \times 1 \text{ mm}^3$ (LxWxH) with a void fraction of $\varphi \approx 0.5$. The tubes are 60 mm in length with a diameter of $D_{tube} = 2.5 \text{ mm}$, and the dimensions of the dissipator cold plates are $25 \times 42 \times 1 \text{ mm}^3$ (LxWxH). The dimensions given for HA and HD only account for the microchannel heat exchanger mesh volume (modeled as porous media in this work), but not the solid material that composes the entire device. We assume the same mesh for both, HA and HD . For the 2D model, length scales and cross section areas of the three units (HA , Tube, HD) are kept close to the actual device in order to reproduce the flow velocity and fluid travel time. The channel height of the porous media domains is such that the cross-sectional flow velocity complies with the intrinsic pore velocity \mathbf{v} , which is related to the well-known Darcy velocity as $\bar{\mathbf{v}} = \varphi \cdot \mathbf{v}$ [45, pp. 4]. Taking the tube diameter D_{tube} as a reference, the fluid-

saturated porous media channel heights of the HA and HD in the 2D simulation are adjusted to match the corresponding cross sections. The ratios of the cross-sectional areas in the x-z plane are

$$\begin{aligned} A_{HA}/A_{tube} &\approx 1 \\ A_{HD}/A_{tube} &\approx 4. \end{aligned} \tag{3.1}$$

The fluid volume is in the range of $V_{HA} = 100 \mu\text{l}$, $V_{tube} = 300 \mu\text{l}$, $V_{HD} = 500 \mu\text{l}$. In [35] we derive fluidic and thermal performance figures of mesh-type microchannel cold plates from unit cell conjugate heat transfer CFD calculations and experimental validations. These data is implemented into the fluid-saturated porous media parameters of the present research.

3.2.1 Fluidic Considerations

To calculate the velocity \mathbf{v} and pressure p in the flow channels, the incompressible, time-dependent Navier-Stokes equations are considered

$$\begin{aligned} \rho \left(\frac{\partial \mathbf{v}}{\partial t} + (\mathbf{v} \cdot \nabla) \mathbf{v} \right) &= -\nabla p + \mu \Delta \mathbf{v} + F \\ \nabla \cdot \mathbf{v} &= 0 \end{aligned} \tag{3.2}$$

This facilitates taking inertial forces ($\partial \mathbf{v} / \partial t$ for unsteady and $(\mathbf{v} \cdot \nabla) \mathbf{v}$ for convective accelerations) into account. F represents a volume body force. The fluid viscosity is assumed to be constant, $\mu = \mu_{H_2O}$. For the interconnecting free flow tubes, no-slip flow boundary conditions

$$\mathbf{v} = 0 \tag{3.3}$$

are applied and the body forces F are omitted

$$F_{tube} = 0 \tag{3.4}$$

The average pore Reynolds number in the fluid saturated porous media modeled here is clearly above 10, and therefore, inertia effects (or form drag) have to be considered [46, pp. 10], [47, pp. 12]. A modified permeability $\kappa = \kappa(\mathbf{v})$ that is a function of flow velocity is introduced in order to transform the nonlinear flow equation (in literature usually referred to as *Darcy-Forchheimer* flow [48]) into the pseudo-linear Darcy form [49]:

$$\frac{dp}{dx} = -\frac{\mu}{\kappa} \cdot \mathbf{v} \quad (3.5)$$

Following the numerical simulations of a five-layered unit cell stack [35], we assume a homogenous fluid flow velocity across the heat transfer mesh. Therefore, the effect of solid walls as proposed in Brinkman's equation [50] is excluded. Instead, slip-flow conditions

$$\mathbf{n} \cdot \mathbf{v} = 0 \quad (3.6)$$

are applied to the top and bottom boundaries of the corresponding porous media domains (HA , HD , \mathbf{n} : normal vector). For the porous media domains HA , HD the body force in Eq. 3.2 represents the hydraulic losses in terms of Eq. 3.5:

$$F_{HA,HD} = -\frac{\mu}{\kappa(\mathbf{v})} \mathbf{v} \quad (3.7)$$

Three microchannel heat transfer meshes ($V1$, $V2$, and $V3$) of different porosities ($\varphi_{V1}=0.55$, $\varphi_{V2}=0.5$, $\varphi_{V3}=0.45$) are defined and simulated in this work. The implementation into the simulation of the porous media permeability as a function of pore velocity and mesh type is presented in Fig. 3.4 (right y-axis).

As mentioned above, the flow channel height and length are chosen to match velocity and fluid travel time occurring in a mesh-type microchannel cold plate. With the mathematical description of the fluid flow domain, the flow profile stays uniform (plug flow) in the heat exchanger mesh domains (HA , HD) but develops along the

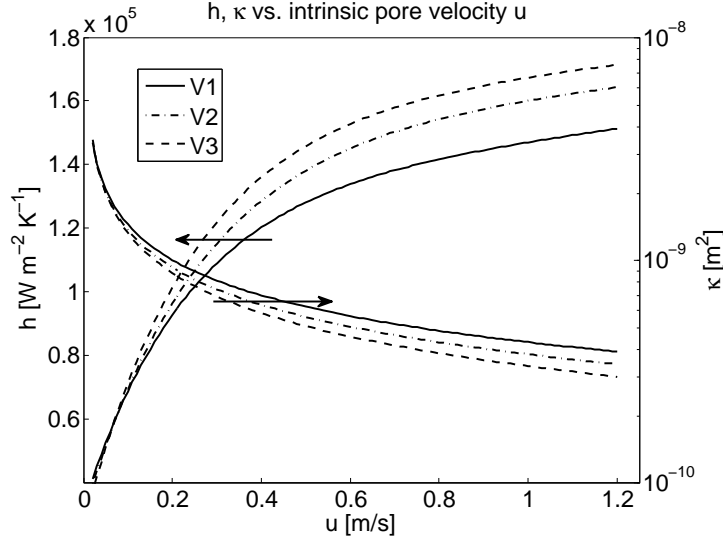


Figure 3.4: Heat transfer coefficient h and permeability κ are implemented as velocity-dependent variables in the simulation domain. Three different microchannel heat transfer meshes $V1$, $V2$, and $V3$ with variable porosities φ are studied.

interconnecting tubes. Therefore, the fluid flow speed developing inside HA , HD represents the intrinsic average flow speed in the ‘pores’ of the microchannel cold plate. In order to account for variable porosity values the height of the fluid flow channels is adjusted accordingly.

3.2.2 Thermal Considerations

A 0.5 mm thick silicon chip ($\lambda_{Si} = 124 \text{ W m}^{-1} \text{ K}^{-1}$) is modeled, which dissipates a constant heat flux at $\partial\Omega_{Si} = \dot{q}_{chip}$. A fixed thermal interface resistance of $R_{TIM} = 10 \text{ W mm}^2 \text{ K}^{-1}$ connects the chip to the solid base of the HA . The top and bottom side of the HD ’s are assumed to be at a constant temperature T_{amb} . All other external

boundaries are represented by adiabatic conditions

$$\frac{\partial T}{\partial \mathbf{n}} = 0. \quad (3.8)$$

The heat exchanger devices (HA , HD) consist of a porous media fluid flow channel which is sandwiched between solid copper slabs. The effective heat capacity

$$C_{p,eff} = C_{p,Cu} \cdot X_{Cu} \quad (3.9)$$

of the solid copper parts account for additional thermal mass available in a real physical system (casing, frame, etc.). This is essential to identify thermal time constants of a transient model as presented in this work. The following energy balancing equation is employed to calculate the time-dependent temperature distribution in the simulation domain:

$$\rho C_p \frac{\partial T}{\partial t} + \nabla \cdot (-\lambda \nabla T) = -\rho C_p \mathbf{v} \cdot \nabla T. \quad (3.10)$$

We assume thermal radiation, viscous heating and pressure work to be negligible. The same equation is employed for the solid parts, but with $\mathbf{v} = 0$. Mesh-type microchannel cold plates exhibit high thermal conductivity in the vertical direction because a continuous thermal path in the solid material is provided. Therefore, a rather uniform temperature distribution in the z-direction is to be expected. This is implemented in the simulation domain by employing an anisotropic fluid thermal conductivity in the porous media channels of the heat exchangers:

$$\lambda_{PM} = \begin{pmatrix} \lambda_{H_2O} & 0 \\ 0 & \lambda_{Cu} \end{pmatrix} \quad (3.11)$$

The definition of the boundary conditions between the fluid flow channels and its adjoining solid copper slabs are used to allow for high convective heat transfer rates occurring in microchannel cold plates. It follows that

$$\vec{n} \cdot \lambda \nabla T = h \cdot (T_{solid} - T_{fluid}) \quad (3.12)$$

where $h = h(\mathbf{v})$ is a velocity-dependent area heat transfer coefficient extracted from unit cell simulations discussed in [35]. The implementation of the heat transfer coefficient as a function of pore velocity and mesh type into the numerical simulation is presented in Fig. 3.4 (left y-axis).

In order to reduce the simulation model to the most important components, the different subdomains (HA , Tube, HD) have been detached from each other, cp. Fig. 3.2. Therefore, transition regions between free flow domains, porous media domains, and expansions/constrictions are not resolved. We expect the pressure loss error of this approximation to be $< 5\%$; from a thermal perspective the accuracy might be even better since heat transfer mainly occurs within the HA and HD 's and the fluid volume is kept close to the actual device. Large flow velocity or pressure gradients can be omitted, and therefore, the numerical solver converges faster. Instead, the pressure potentials and velocities are averaged at the openings of each subdomain and assigned to the boundary of the neighboring subdomains. As an example, the boundary conditions for the openings between the heat absorber and the left tube, when fluid flows from right to left, are determined as follows:

$$\mathbf{v}_{tube,in} = \frac{1}{H_{HA}} \int_{-H_{HA}/2}^{H_{HA}/2} \mathbf{v}_{HA,out}(y) \cdot dy \quad (3.13)$$

and

$$p_{HA,out} = \frac{1}{H_{tube}} \int_{-H_{tube}/2}^{H_{tube}/2} p_{tube,in}(y) \cdot dy \quad (3.14)$$

The simulation is implemented in such way that inflow boundary conditions are always velocity and outflow conditions are always pressure. As a matter of consequence, the inlet/outlet boundary conditions switch between pressure and velocity every half-cycle of the fluid oscillation. At the boundaries $\partial\Omega_{HD,left/right}$, where the fluid enters (“in”) or leaves (“out”) the simulation domain, either a constant flow velocity $\mathbf{v} = \mathbf{v}_{in}$ or zero pressure p_{amb} is defined

$$\partial\Omega_{HD,left} \begin{cases} \mathbf{v} = \mathbf{v}_{in} = \mathbf{v}_0 \cdot \sin(\omega t), T = T_{amb} & 0 \leq \omega t \leq \pi \\ p = p_{amb} = 0, T = \text{undef} & \pi < \omega t < 2\pi \end{cases} . \quad (3.15)$$

The flow direction from left to right is defined as positive. In the “in” state, the fluid temperature is set to a constant value of $T_{in} = 293$ K at the domain boundary. In turn, the boundary temperature is undefined when the fluid leaves the domain, i.e. in the “out” state. This can be justified by the assumption that the fluid completely cools down to the system thermodynamic ground potential, being T_{amb} , when it traverses the dissipator cold plate. For small fluid displacements per stroke, e.g. $\bar{A} = A/A_0 < 1$, this assumption is rather optimistic. However, it is adopted as a simplification of the complex simulation procedure.

The simulation results we are presenting are generated as follows: at $t = 0$ the domain is initialized at constant temperature $T_{\Omega}(t=0) = 293$ K and the fluid velocity is $\mathbf{v}_{\Omega}(t=0) = 0$; for $t > 0$, a constant chip heat flux \dot{q}_{chip} starts to heat up the system while the fluid starts oscillating in a reciprocating manner according to Eq. 3.15.

By varying the parameters u_0 and $f = \omega/2\pi$, different fluid displacement areas A

$$A = \mathbf{v}_o \cdot H_{HD} \cdot \int_0^{1/2f} \sin(2\pi \cdot f \cdot t) dt = \frac{\mathbf{v}_o \cdot H_{HD}}{\pi \cdot f} \quad (3.16)$$

can be established. Later in the results discussions, the relative fluid displacement area compared to the total domain area is taken as a reference

$$\bar{A} = \frac{A}{A_0}. \quad (3.17)$$

This is an important measure as it allows scaling the cooling system to any other size. The total domain area A_0 consists of

$$A_0 = A_{HA} + 2 \cdot (A_{tube} + A_{HD}). \quad (3.18)$$

Since the performance figures of this system are discussed in quasi-steady thermal and fluidic conditions, numerical calculations are executed that pass through the start-up phase for several seconds and oscillation cycles. Consequently, the physical measures, namely pressure and temperature, are averaged over one cycle $t_{cycle} = 1/f$.

The numerical simulations conducted using COMSOL Multiphysics 3.5 and grid independence tests are performed to satisfy the constraint to reach some asymptotic values as close as 1%. The model used in this work consists of 5600 mesh cells and the boundaries are resolved in high accuracy (maximum computational grid cell size of $100 \mu m$ over the entire domain).

3.3 Results and Discussion

In the first part, frequencies f and relative fluid displacements \bar{A} are studied while the microchannel heat transfer mesh is kept fixed to a single design (*VI*). Therefore, fluidic performance characteristic in terms of pressure drop for a single mesh design is discussed first, followed by the thermal behavior with respect to the total thermal resistance. Next, the chip temperature fluctuations and the system coefficient of performance (*COP*) are presented. In the second part, the fluid oscillation frequency is kept constant, while the influence of different mesh porosities on the fluidic and thermal performance is studied.

3.3.1 Variable Frequency f , Fixed Mesh Design *Vi*

The cycle-averaged system pressure drop is determined by calculating the difference of the maximum and minimum absolute pressure over one cycle at one end of the simulation domain, i.e. $\partial\Omega_{HD,left/right}$, and determining its *root mean square* (RMS) value

$$\Delta p_{RMS} = \frac{\sqrt{2}}{2} \cdot (p_{\max} - p_{\min}) . \quad (3.19)$$

Figure 3.5 displays system pressure drop Δp_{RMS} as a function of fluid stroke \bar{A} at different frequencies f . Data fitting of the simulation results delivers

$$\Delta p_{RMS} (f, \bar{A}) = 5.525e4 \cdot f^{1.441} \cdot \bar{A}^{1.416} \quad (3.20)$$

with a goodness of model fit $R^2 > 0.99$. As can be seen, the pressure drop follows a power characteristic of both frequency and fluid displacement. Assuming a maximum allowable system pressure loss of $\Delta p_{RMS} < 1$ bar, the system driving parameter can be chosen between *large displacement / low frequency* (e.g. 3/0.5), or *small displacement/high frequency* (e.g. 0.4/4).

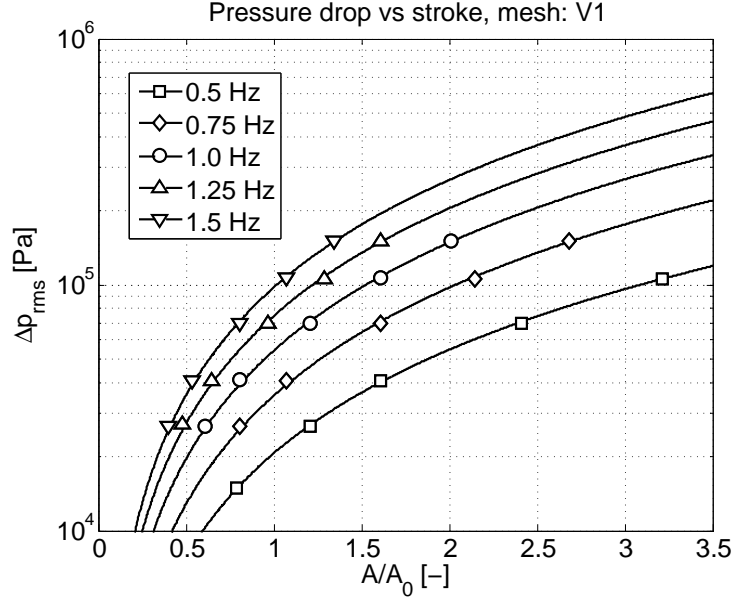


Figure 3.5: Averaged system pressure losses Δp_{RMS} as a function of fluid displacement \bar{A} and frequency f . A fixed heat transfer mesh design *V1* is implemented.

In analogy to the electrical bulk resistance, the thermal resistance R_{th} is a common measure to determine the performance of a cooling system. The total thermal resistance of the system discussed in this work is defined as the ratio of temperature difference between the source and the ambient (thermodynamic ground potential), and the input heat flux

$$R_{th} = \frac{T_{chip} - T_{amb}}{\dot{q}_{in}} \quad [K \text{ mm}^2 \text{ W}^{-1}]. \quad (3.21)$$

In Fig. 3.6, the total thermal resistance is represented as a function of fluid stroke \bar{A} at different frequencies f . The characteristic follows a power function of the form

$$R_{th}(f, \bar{A}) = a(f) \cdot \bar{A}^{b(f)} + c(f) \quad (3.22)$$

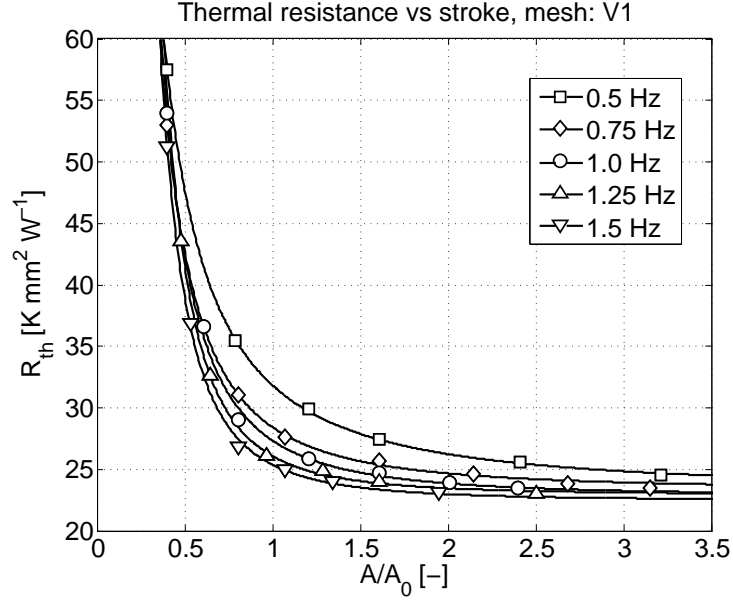


Figure 3.6: Area-normalized thermal resistance R_{th} from the chip junction T_j to the thermal ground potential T_{amb} . The thermal performance R_{th} is described as a function of fluid displacement \bar{A} and frequency f . A fixed heat transfer mesh design *V1* is implemented.

with $c(f)$ representing the lowest possible thermal resistance for an infinite fluid displacement. It can clearly be seen that the cooling performance drastically increases for a fluid stroke $\bar{A} < 1$. In this case, the heat shuttling from the absorber (*HA*) to the dissipater (*HD*) is only established to a limited extent; i.e. the amount of fluid that is displaced per stroke is not completely passing the *HA* and spreading to the *HD*. In turn, at a stroke $\bar{A} > 2$, the thermal resistance differs from the asymptotic value $c(f)$ by $\approx 5\%$. This is especially true for $f \geq 0.75$ Hz. The lowest R_{th} values reached in this study are in the range of $23.5 \text{ K mm}^2 \text{ W}^{-1}$ (e.g. $\bar{A} = 2.5$, $f = 1.5$ Hz). For a chip size of $15 \times 15 \text{ mm}^2$ and $T_{j,max} = 85 \text{ }^\circ\text{C}$, some 600 W could be dissipated ($T_{amb} = 20 \text{ }^\circ\text{C}$).

From Fig. 3.6 one can also deduce the impact of the oscillation frequency on the

cooling performance: by taking a fixed stroke, with increasing frequency, the relative thermal performance improvement becomes smaller. E.g. at a constant $\bar{A} = 1.0$, when increasing the frequency from 0.5 to 0.75 Hz and from 1 to 1.5 Hz (50% higher frequency in each case), R_{th} decreases by 11% and 7%, respectively. At the same time, recalling Fig. 3.5, the pressure losses Δp_{RMS} increase by 64 and 185% for the same frequency raise.

The coefficient of performance (COP) is defined as the ratio of the cycle-averaged thermal power to the cycle-averaged fluid pumping power

$$COP = \frac{P_{thermal}}{P_{pump}} \quad (3.23)$$

with

$$P_{thermal} = \frac{T_{j,max} - T_{amb}}{R_{th}} \cdot L_{HA} \quad [W/m] \quad (3.24)$$

and

$$P_{pump} = \mathbf{v}_{HD} \cdot H_{HD} \cdot \Delta p \quad [W/m]. \quad (3.25)$$

The thermal power $P_{thermal}$ represents the maximum allowable heat input into the system for the heat source (e.g. chip junction temperature) to stay below $T_{j,max} = 358$ K (at a thermal ground potential of $T_{amb} = 293$ K). The pump power P_{fluid} utilized here is similar to the well-known definition of *fluid flow rate* x *pressure drop* but in two dimensions (cp. Eq. 3.25). Figure 3.7 displays the COP as a function of fluid stroke \bar{A} at different frequencies f with the y-axis in logarithmic scale. A clear trend towards lower COP 's for larger strokes can be determined. The same holds for an increase in frequency. In other words, the system becomes less efficient with an increase in fluid displacement and/or frequency. Higher thermal performance can only be achieved at the expense of a non-proportional increase in pumping power. When inserting Eq. 3.20 and 3.22 into Eq. 3.23 a proportionality

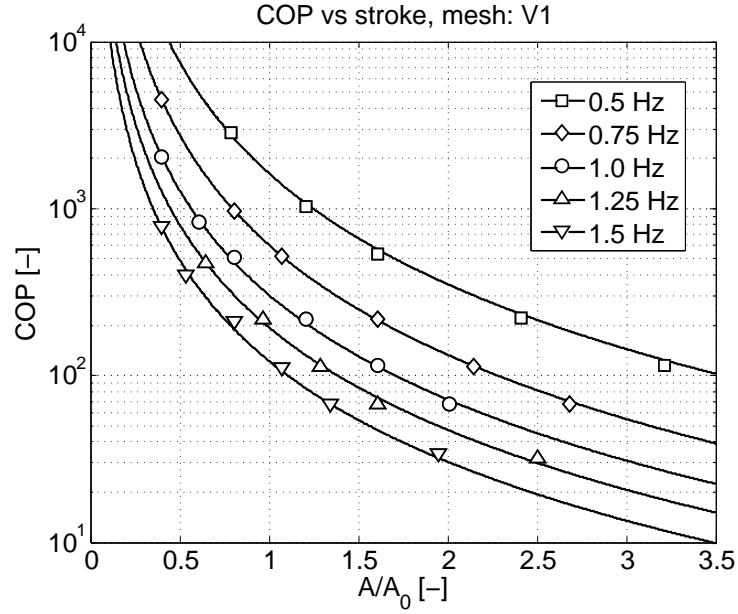


Figure 3.7: Coefficient of performance (COP) depending on fluid pump stroke \bar{A} and frequency f . A fixed heat transfer mesh design $V1$ is implemented. COP describes the allowable heating power compared to the required pumping power.

of $COP \propto \bar{A}^x$ with $x < 1$ can be determined, e.g. for $f = 1$ Hz, $x = 0.35$.

Since the fluid flow of the cooling system presented in this paper is subject to an ongoing velocity change $\mathbf{v} = \mathbf{v}_0 \cdot \sin(\omega t)$, heat transfer rates from one element to the next are oscillating as well. Therefore, the temperature cycling of the chip junction temperate T_j has to be investigated as well. Large temperature oscillations negatively affect the lifetime of a microprocessor. As shown in Fig. 3.6, small fluid strokes $\bar{A} < 1.0$ lead to a drastic rise in the overall thermal resistance or chip junction temperature, respectively. A similar behavior can be observed for the temperature oscillations presented in Fig. 3.8. For $f = 0.5$ Hz, $\Delta T_{j,max}$ is reduced significantly when the fluid stroke is increased. However, this is no longer the case for larger frequencies, e.g. $f > 1.0$ Hz. Here, the thermal time constant of the cooling system

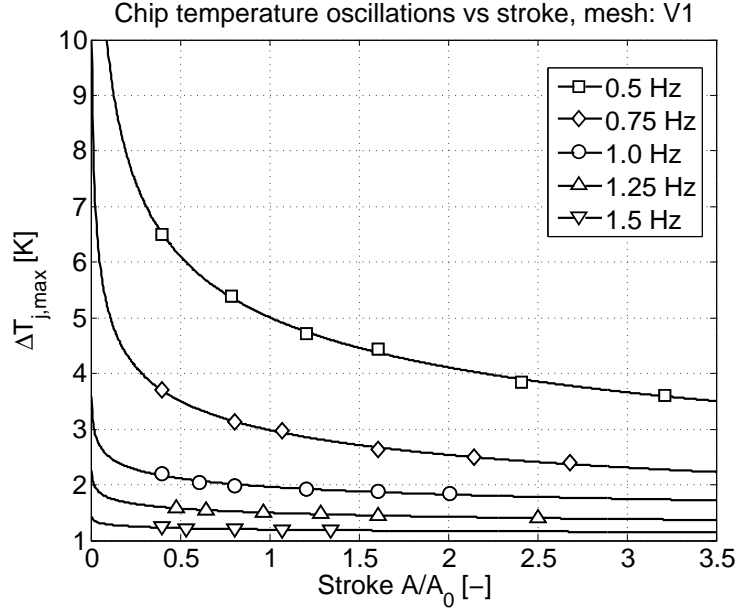


Figure 3.8: Chip junction temperature oscillations $\Delta T_{j,max}$ as a function of \bar{A} and frequency f . A fixed heat transfer mesh design *V1* is implemented.

becomes larger than the oscillation time period, $\tau > 1/f$. The effect of a variable thermal mass factor X_{Cu} , cp. Eq. 3.9, is not graphically presented in this paper. We executed simulation runs for $1 \leq X_{Cu} \leq 3$ and found characteristics similar to that displayed in Fig. 3.8. Generally speaking, an increase in frequency f exhibits a large effect on the reduction of the chip junction temperature oscillations $\Delta T_{j,max}$. For $f \geq 1.0$ Hz, an increase in fluid flow stroke \bar{A} reduces $\Delta T_{j,max}$ to a minor extent only. However, in the case of longer interconnecting tubes, the fluid travel time (or dead time) is longer. Therefore, higher frequencies would help to keep $\Delta T_{j,max}$ at a desired low value.

We close the discussion of the results for the mesh *V1* with a performance overview. In Fig. 3.9 the pressure drop Δp_{RMS} is shown as a function of the fluid displacement \bar{A} , together with the trajectories of constant thermal resistances (isometric R_{th}).

A specific thermal performance can either be reached by adjusting the frequency f or the fluid displacement \bar{A} . E.g. for $R_{th} = 26 \text{ K mm}^2 \text{ W}^{-1}$, the extremes of the driving parameter range are $\bar{A} = 2.1 / f = 0.5 \text{ Hz}$ and $\bar{A} = 0.8 / f = 1.5 \text{ Hz}$. The corresponding system pressure losses are 58 kPa and 80 kPa. From a pumping power perspective, *large displacement / low frequency* is superior to *small displacement / high frequency*. However, this behavior diminishes as \bar{A} increases. For fluid displacements $\bar{A} > 1.5$, the pressure drop stays rather constant as the driving parameters are set to either *large \bar{A} / low f* or *small \bar{A} / high f* . Figure 3.9 contains some important information to lay out such a cooling device according to the system constraints. A minimum and compulsory requirement is a fluid displacement of $\bar{A} \approx 1$. If enough space is available for large pumps, one would rather choose a low frequency and large displacement. In turn, if the chip temperature oscillations are the limiting factor, *small \bar{A} / high f* is the parameter set of choice.

3.3.2 Constant Frequency f , Variable Mesh Design Vi

In the second part of the discussions, the oscillation frequency is always kept constant at $f = 1 \text{ Hz}$, but the microchannel heat transfer mesh Vi in the heat absorber (HA) and dissipator (HD) device is varied. We modeled three meshes ($V1$, $V2$, $V3$) with various porosity values of $\varphi_{V1} = 0.55$, $\varphi_{V2} = 0.50$, and $\varphi_{V3} = 0.45$ (cp, Fig. 3.4).

Figure 3.10 illustrates the system pressure drop as a function of the fluid displacement \bar{A} at a constant frequency of $f = 1 \text{ Hz}$. As discussed in Fig. 3.4, a lower porosity φ value causes a lower permeability κ . Therefore, the pressure losses are highest for $V3$ and lowest for $V1$ at any operating point \bar{A} / f . The difference in pressure loss between $V1$ and $V3$ is 20, 16, and 10% for $\bar{A} = 0.6$, 1.2, and 2, respectively. In turn, the porosity of $V3$ compared to $V1$ is lower by 18%.

We can complete Eq. 3.20 to describe the system pressure drop as a function of

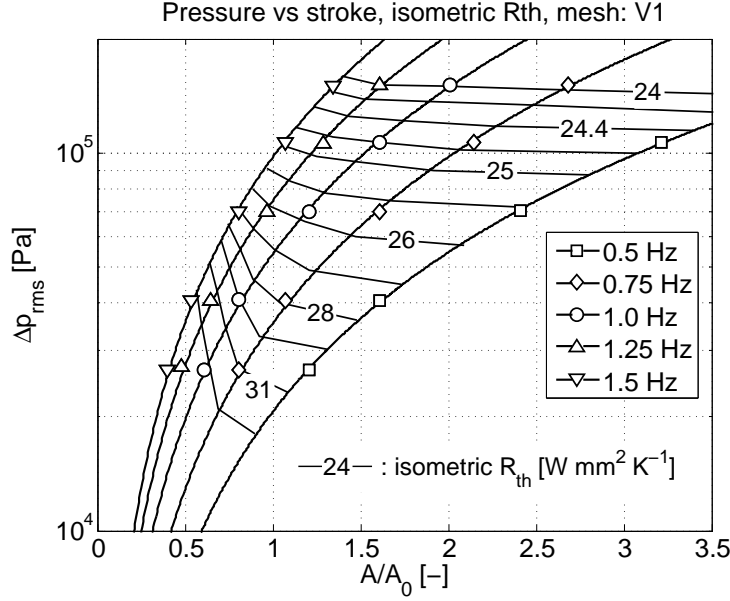


Figure 3.9: Averaged system pressure losses Δp_{RMS} as a function of fluid displacement \bar{A} and frequency f . A fixed heat transfer mesh design $V1$ is implemented. Additionally, isometric thermal resistance R_{th} values are plotted to illustrate the dependency of fluidic and thermal performance.

stroke \bar{A} , frequency f , and porosity φ as

$$\Delta p_{RMS}(\varphi, f, \bar{A}) = 1.056e5 \cdot 0.308^\varphi \cdot f^{1.441} \cdot \bar{A}^{1.416}. \quad (3.26)$$

The same comparison for different porosity levels φ_{Vi} with regard to the thermal performance R_{th} is depicted in Fig. 3.11. Again, recalling the mesh properties illustrated in Fig. 3.4, a lower porosity value φ leads to higher heat transfer rates h , and therefore, the system thermal resistance R_{th} decreases. The performance improvement of $V3$ compared to $V1$ is in the range of 2 - 4% for the fluid displacement range presented in this work. This corresponds to a chip junction temperature decrease of approx. 3 K (based on $T_{j,max} = 358$ K) or a heat flux increase of 7 W/cm² ($R_{th} = 23.9$ K mm² W⁻¹, $\Delta T = 65$ K). In all cases, R_{th} slowly lowers as $\bar{A} > 1$ becomes

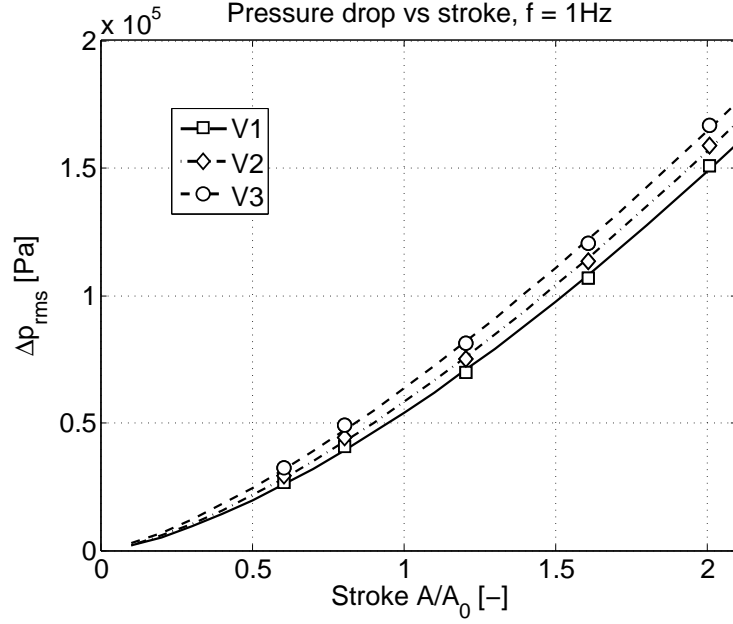


Figure 3.10: Averaged system pressure losses Δp_{RMS} as a function of fluid displacement \bar{A} and heat transfer mesh design V_i . The pump oscillations frequency is kept constant at $f = 1\text{Hz}$.

larger. In turn, the slope increases rapidly as $\bar{A} < 1$ moves towards zero.

A higher thermal performance can be achieved by improving the heat transfer rate of the microchannel heat transfer mesh, e.g. by changing from $V1$ to $V3$. This is at the cost of higher pressure losses and, correspondingly, higher pumping power. The interplay of fluidic and thermal performance for various mesh densities is described in Fig. 3.12. We can find an ideal heat transfer mesh design according to the given performance specifications. Down to a cooling performance of $R_{th} \approx 27 \text{ K mm}^2 \text{ W}^{-1}$ the coarsest mesh $V1$ would be the design of choice. In the range of $27 > R_{th} \geq 25.5 \text{ K mm}^2 \text{ W}^{-1}$, the microchannel mesh design $V2$ performs best with regard to the pumping power. And finally, for $R_{th} < 25.5$, it is the mesh $V3$ that would be chosen. This is an important observation since it illustrates the necessity to first define peak

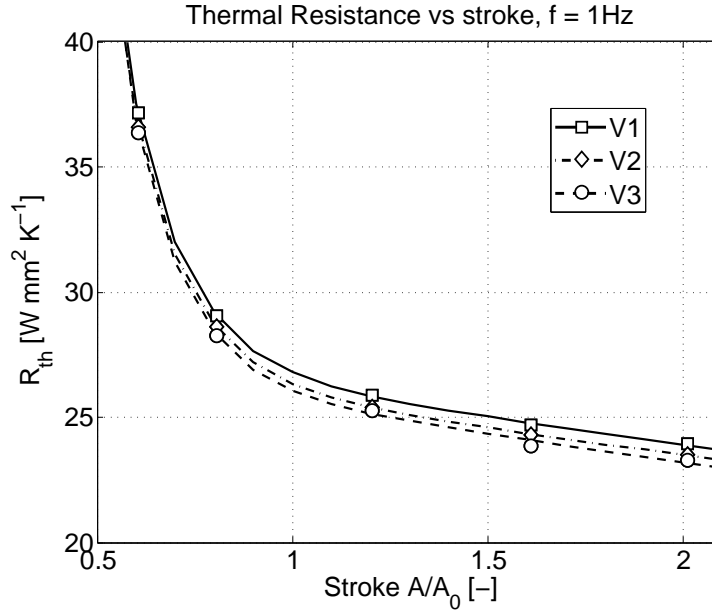


Figure 3.11: Area-normalized thermal resistance R_{th} from the chip junction T_j to the thermal ground potential T_{amb} . The thermal performance R_{th} is described as a function of fluid displacement \bar{A} and heat transfer mesh design V_i . The pump oscillations frequency is kept constant at $f = 1$ Hz.

performance specifications of such a heat transfer/heat spreading system. Once the cooling requirements and the available pumping power are set, the microchannel heat transfer mesh can be designed accordingly.

3.3.3 Experimental Verification of Simulation Results²

As mentioned earlier, the corresponding experimental implementation of the at hand heat spreading system has been accomplished in a different work [44]. In this chapter we are verifying the simulation results with the according experimental data.

A very close match was found for the cycle-averaged system pressure drop. In Fig.

²This section is not published in [44].

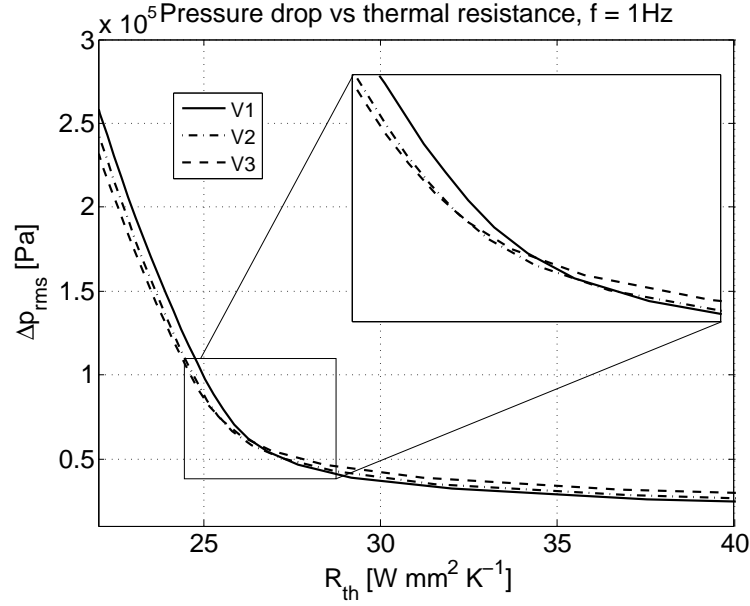


Figure 3.12: Cycle-averaged system pressure losses Δp_{RMS} as a function of the area-normalized thermal resistance R_{th} and heat transfer mesh design V_i . The insert displays a close-up view in the range of $25 \leq R_{th} \leq 28.5$, $40'000 \leq \Delta p_{RMS} \leq 125'000$.

3.13 the measured pressure losses as a function of \bar{A} and the frequencies f 0.5, 1.0, and 1.5 Hz are plotted and compared to the simulation results, cp. Chapter 3.2.1. Even with an assumed error estimation of 10%, the simulation results are highly satisfactory. Since the characteristic behavior of the system pressure loss with regard to the frequency, fluid displacement and heat transfer mesh properties is well reflected, we conclude that the simulation model presented in this work is, at least from a fluidic perspective, set up well.

The comparison of the thermal system performance between the simulation and experiments is shown in Fig. 3.14. Again, with regard to the frequency and fluid displacement, the characteristics match well. However, the experimental data pre-

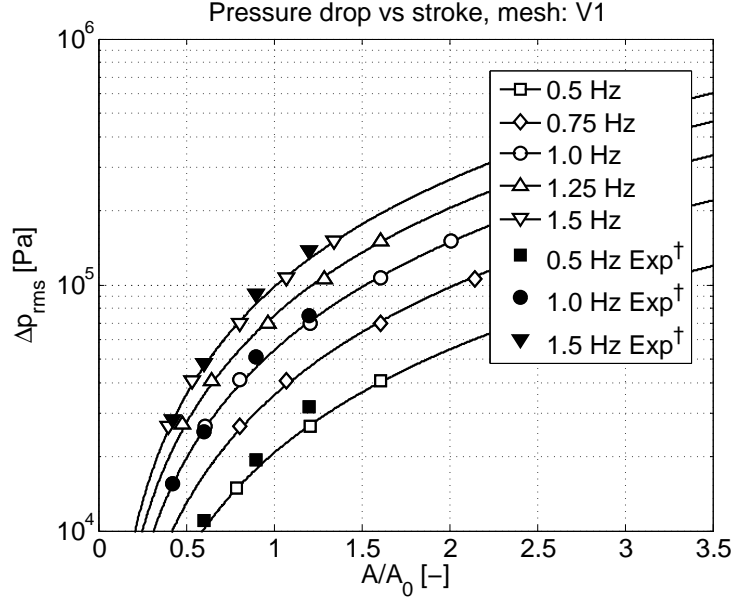


Figure 3.13: Comparison of the system pressure drop between the numerical simulations and the experiments. †The experimental data is discussed in Chapter 3 and published in [44].

sented in Fig. 3.14 excludes the thermal resistance of the rack-loop's cold plate. The subdivision of the overall thermal budget of the present cooling device is presented in Chapter 4.3.4, Fig. 4.8. The value of $R_{CP} = 0.021$ K/W is subtracted from the overall thermal resistance and a chip area of 15×15 mm² is taken into account in order to compare the experimental results with our numerical model, cp. Fig. 3.14. The deviation becomes larger as \bar{A} decreases. As discussed in Fig. 3.6, the sensitivity of R_{th} over \bar{A} grows exponentially as $\bar{A} \rightarrow 0$. Here, small deviations have drastic consequences to the thermal performance. The mismatch is therefore explained with small inaccuracies of the piston pump fluid displacement. However, this operating point is of little interest, and in the range of $0.8 < \bar{A} < 1.5$, the simulation agrees well with the experimental data.

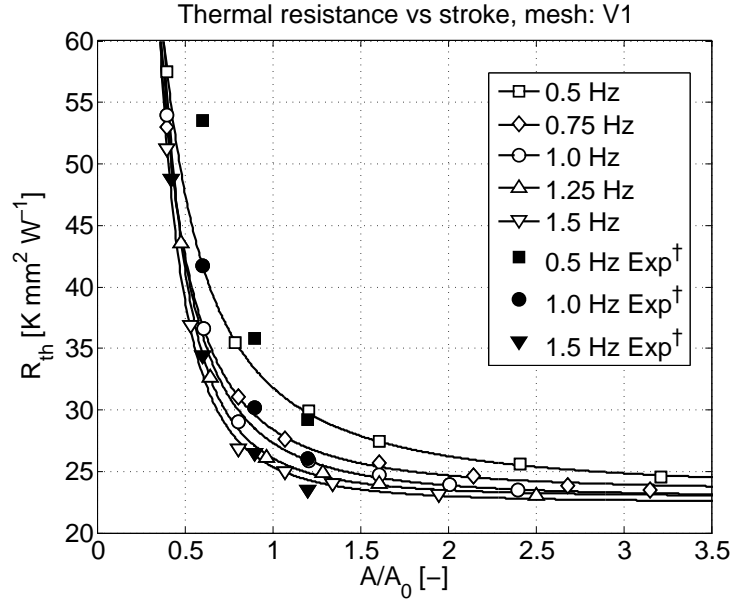


Figure 3.14: Comparison of the system thermal resistance between the numerical simulations and the experiments. For comparison reasons, the rack-loop's thermal budget of $R_{th} = 0.21$ K/W, cp. Chapter 4.3.4, is subtracted and a chip area $A_{chip} = 15 \times 15$ mm² assumed. †The experimental data is discussed in Chapter 3 and published in [44].

3.4 Summary and Conclusions

We have demonstrated an efficient approach to predict the performance figures of a self-contained, reciprocating liquid cooling system for low form factor electronics equipment. A two-dimensional model comprising the heater chip, the absorber and dissipator cold plates, and the interconnecting tubes has been set up and solved numerically using a commercial CFD code. The microchannel heat transfer meshes are described as fluid saturated porous media, where a velocity-dependent permeability is introduced to transform the nonlinear porous media flow into a pseudo-linear equation. This, in turn, is introduced into the Navier-Stokes equations as a body force. The convective heat transfer between solid and fluid is established with the

definition of the corresponding boundary conditions by a velocity-dependent heat transfer coefficient. To make the entire porous media cross section active for high heat transfer, the thermal conductivity of the fluid inside the porous media is defined as *anisotropic*. The thermal conductivity in the direction perpendicular to the flow equals that of the solid, i.e. copper. For tractability reasons, transition regions from porous media to free flow are not modeled in detail. Instead, the different elements are physically separated but interconnected in the model using adequate boundary conditions.

The thermal and fluidic results are presented in quasi-stationary conditions, where physical values are averaged over one fluid pump cycle. Therefore, each simulation run starts from $t = 0$ and an initial temperature T_0 and lasts for multiple cycles until quasi-stationary states are reached.

The system driving parameters are the fluid displacement per oscillation cycle, namely the stroke \bar{A} , and the frequency f . The results discussed in this work cover the range of $0.5 \leq \bar{A} \leq 3.5$, $0.5 \leq f \leq 1.5$, and three different microchannel heat transfer meshes with porosities of $0.45 \leq \varphi \leq 0.55$.

The pressure losses follow a power characteristic of both \bar{A} and f , and a specific pressure drop is reached depending on the operating points, e.g. *large \bar{A} /low f* , or *small \bar{A} /high f* . For $\bar{A} < 1$, the thermal resistance R_{th} drastically increases, and for $\bar{A} > 2$, R_{th} approaches an asymptotic value. Therefore, the system has to be designed so that the liquid pump stroke is in the range of $1 < \bar{A} < 2$. Chip heat loads of 600 W ($A_{chip} = 15 \times 15 \text{ mm}^2$) are manageable in order that the junction temperature stays below 85 °C ($T_{amb} = 20 \text{ °C}$). An increase in oscillation frequency f has a positive effect on the thermal performance, however, with increasing pump stroke \bar{A} , the improvement diminishes. The junction temperature cycling $T_{j,max}$ decreases with an increase in the fluid oscillation frequency f . However, for $f > 1 \text{ Hz}$, the junction temperature oscillations realize a minor diminution. One can expect a $T_{j,max} < 2 \text{ K}$

for $f > 1\text{Hz}$.

A specific thermal performance can either be reached by adjusting the frequency f or the fluid displacement \bar{A} . From the comparison of fluidic and thermal performance, we conclude that, from the perspective of the pumping power, *large \bar{A} /low f* is superior to *small \bar{A} /high f* .

However, from a design view point, one has to first localize the system constraints and specifications. The fluid volume of the entire heat spreading system, including the absorber HA , interconnecting tubes, and dissipators HD devices, is a crucial parameter, since it defines the pump stroke and power. The system volume is in the range of several hundred microliters (excluding the reservoirs of the pumps), and the volume of interconnecting tubes should be in the range of the heat dissipators (100-300 μl). Other important system constraints are the maximum power load, the maximum allowable chip temperature cycling, and the space available space inside the electronic equipment. We have shown how the maximum cooling performance specifications have an influence on the design of the microchannel heat transfer mesh design.

4 Experimental Investigation of a Self Contained, Reciprocating Liquid Heat Spreader System for Low Form Factor Electronics¹

Abstract

A self-contained, small-volume liquid cooling system for thin form factor electronic equipment (e.g. blade server modules) is demonstrated experimentally in this paper. A reciprocating water flow loop absorbs heat using mesh-type microchannel cold plates and spreads it periodically to a larger area. From there, the thermal energy is interchanged via large-area, low pressure drop cold plates with a secondary heat transfer loop (air or liquid). Four phase-shifted piston pumps create either a linearly or radially oscillating fluid flow in the frequency range of 0.5 - 3 Hz. The tidal displacement of the pumps covers 42 - 120% of the fluid volume, and, therefore, an average flow rate range of 100 - 800 ml/min is tested. Three different absorber mesh designs are tested. Thermal and fluidic characteristics are presented in a time-resolved and a time-averaged manner. For a fluid pump power of 1 W, a waste heat flux of 180 W/cm² ($\Delta T = 67$ K) could be dissipated from a 3.5 cm² chip. A linear oscillation flow pattern is advantageous over a radial one because of the more efficient heat removal from the chip and lower hydraulic losses. The optimum microchannel mesh density is determined as a combination of low pump losses and high heat transfer rates.

¹This Chapter is submitted for publication: R. Wälchli, T. Brunschweiler, B. Michel, D. Poulikakos, "Self-Contained, Oscillating Flow Liquid Cooling System for Thin Form Factor High Performance Electronics", *ASME Journal of Heat Transfer*, 2009

Nomenclature

A	Area [mm ²]
CP	Collector plane [mm]
D	Channel width [mm]
D_{PP}	Piston pump stroke [ml]
D_{VC}	Volume coverage [%]
DCB	Direct copper bonding
f	Piston pump frequency [Hz]
HA	Heat absorber
HD	Heat dissipator
$HTL1$	Primary heat transfer loop
$HTL2$	Secondary heat transfer loop
Nu	Nusselt number [-]
P	Power [W]
p	Pressure [Pa]
PP	Piston pump
R	Thermal resistance
Re	Reynolds number [-]
RMS	Root mean square
$RTD(i)$	Resistance temperature detector at location $i = 1,4$
T	Temperature [°C]
t	Time [s]
V	Volume [m ³]
$V1, V2, V3$	Microchannel mesh designs
\dot{V}	Fluid flow rate [ml/min]

Greek letters

α	Womersley number [-]
β	Transitions number [-]
Δ	Difference between two measurements
ϕ	Piston pump phase shift [rad]
φ	Mesh porosity [%]
κ	Exponent [-]
ν	Dynamic viscosity [m ² /s]
σ	Standard deviation
τ	Time constant [s]

subscript/superscript

<i>chip</i>	Heater/sensor chip
<i>CP</i>	Collector plain
<i>fluid</i>	Cooling fluid
<i>HA</i>	Heat absorber
<i>HD</i>	Heat dissipator
<i>i</i>	Counter for each piston pump ($i = 1...4$)
<i>in</i>	Inlet
<i>j</i>	Chip junction location
<i>max</i>	Maximum
<i>mean</i>	Averaged value
<i>min</i>	Minimum
<i>PP</i>	Piston pump
<i>tot</i>	Total, overall
<i>tube</i>	Interconnecting tube

4.1 Introduction: Transition to Liquid Cooling

With the continuous increase in power dissipation and advances in packaging technology of electronics equipment, the industry is increasing its product development efforts towards effective heat removal concepts. For blade servers, which are optimized to minimize physical space, effective heat removal from high performance central processing units (CPU) and memory cards is of vital importance. Blade modules are typically restricted to the minimum size requirements of a standard server-rack configuration (1U: one rack unit, 19" wide and 1.75" tall), while still having all the functional components to be considered a computer [4],[5]. Heat spreading concepts such as heat pipes and vapor chambers are traditionally used to distribute excess heat from the processors to a larger area within the blade. There, thermal energy is absorbed by means of high performance air-moving devices blowing subcooled air across the blade. Air heat exchangers are employed to increase the active heat transfer area. This requires a considerable amount of power for the data center air conditioning and air blower operation. Furthermore, the air cooling for both the blade modules and the data center implies a sophisticated air-flow management [51], [52], [53], [54].

As an alternative to air cooling, which reaches its cooling capacity at $\sim 100 \text{ W/cm}^2$ [55], liquid cooling using microchannel cold plates has been demonstrated to be a viable solution for future applications. From the very first demonstrations to enhanced packages, various approaches have been reported resulting in cooling capacities of 350 W/cm^2 and higher [6], [7], [8], [9], [10]. One broad field of cooling schemes, that has received increased interest recently, employs oscillatory flows. Early work on enhanced heat transfer using high frequency oscillatory/pulsating flows can be found in Siegel and Perlmutter [56] and Kurzweg *et al.* [57]. High heat transfer coefficients from a heated floor of a rectangular duct employing low frequency, large

tidal reciprocating flows have been demonstrated by Cooper *et al.* [58]. In Lia *et al.* [59] the heat transfer rate could be enhanced by 100% for reciprocating air flows as compared with standard cooling fans. Furthermore, Sert and Beskok [60] discuss in a numerical study a single-phase, closed microfluidic system, that utilizes reciprocating flow forced convection.

Compared with air, water has a 4000x higher volumetric heat capacity and is simpler to direct within a highly populated electronic package. In contrast, an all liquid cooled computing system requires a significant amount of supplementary equipment, such as piping, hoses, and pumping station. High investment costs are expected when adapting data centers to liquid cooling. Furthermore, a liquid inside electronic equipment can cause significant damage in case of leakage. The working fluid volume embedded in the computing system should therefore be minimized, to limit damage to a minimum in case of flooding. In a blade server system, one could think of a primary, closed fluid loop integrated into each individual blade unit to cool the CPUs and spread the heat to a peripheral area where a second, data center-scale fluid loop collects the waste heat from each blade and finally in a preferred scenario reuses it, for example for district heating [34]. The connection between the local and the global fluid loop is done by means of conduction through a large area interface. This opens up a variety of innovative and highly efficient centralized pumping schemes for an all liquid cooled data center.

The basic idea of spreading heat from a small source to a large area could also be fulfilled by means of a passive phase-change device (vapor chambers or heat pipes). Compared to active liquid cooling systems they are more convenient in operation since no active pumping device is required, making this technology interesting cost- and maintenance-wise. However, they might not be able to handle very high heat fluxes (e.g. $> 150 \text{ W/cm}_2$); thermal spreading distance is limited, and they are optimized to a fixed design point and less flexible for variable thermal loads.

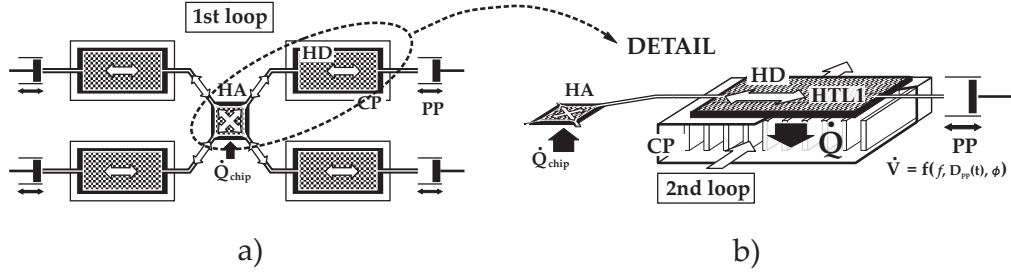


Figure 4.1: Illustration of the oscillating liquid cooling principle: a) heat spreading system with a chip waste heat absorber (HA) in the center and the four heat dissipator (HD) cold plates in the periphery. The fluid oscillations are created by means of phase-shifted piston pumps (PP). b) heat exchange from the chip via the oscillating fluid to the collector plane (CP) of the secondary heat transfer loop.

4.1.1 Principle of Operation

In this paper, we introduce a hybrid (combined liquid-air) cooling system exploiting the effectiveness of liquid cooling to transport thermal energy from the chip via a microchannel heat absorber to a peripheral location. A self-contained, blade-level liquid cooling circuit spreads heat from the source to a larger area. Liquid-to-air heat exchangers dissipate the heat to the environment using traditional air fans blowing across the blade module. This can be seen as a soft transition to all liquid cooling. No central pump and fluid distribution network is needed and the system assembly corresponds to a traditional air heat sink. Therefore, small additional investment costs incur for a data center. Alternatively, the air cooling can be replaced by a secondary, data center-level fluid heat transfer loop that aims at collecting thermal energy from each individual blade module. In this case, a collector plane in between the blades is in thermal contact with the peripheral heat exchangers of the primary heat transfer loop. The risk of flooding is reduced to the amount of liquid contained in the closed cooling circuit inside a blade.

In the following, we demonstrate a self-contained, hermetic liquid cooling system

using oscillating fluid flows to spread heat from a small source to a large area, Fig. 4.1. This is defined as the primary heat transfer loop (*HTL1*) inside the blade. Efficient heat spreading has been demonstrated with effective thermal conductivities of 20x and 50x over copper for spreader plates and interconnecting tubes respectively [20]. A low volume, high-performance microchannel heat absorber (*HA*) is in thermal contact with the heat source. Adiabatic channels connect to four large area heat dissipators (*HD*), which are placed in available space areas of the blade module around the primary heat source. The oscillating fluid flow is established using reciprocating piston pumps (*PP*) connected to the outward-facing side of the *HD*s. Within a pumping cycle, the working fluid takes up heat from the source, carries it to the peripheral *HD*s, exchanges it via the collector planes (*CP*) with a secondary heat transfer loop (*HTL2*), and returns again cooled to the *HA*. The base area ratio of the dissipator plates to the absorber plate A_{HD}/A_{HA} is greater than 30. The four piston pumps operate with identical displacements D_{PP} and frequencies f . However, depending on the phase shift the oscillation flow pattern changes. The position of each individual pump i is defined as:

$$x_i(t) = D_{PP} \cdot \sin(2\pi \cdot f \cdot t + \phi_i), \quad i = 1 \dots 4. \quad (4.1)$$

Flow Pattern	ϕ_1	ϕ_2	ϕ_3	ϕ_4
<i>linear</i> [mm]	0	0	π	π
<i>radial</i> [mm]	0	$\pi/2$	π	$3\pi/2$

Table 4.1: Phase shift ϕ of the four piston pumps (*PP*) to establish linearly and radially oscillating fluid flows.

In a linearly oscillating flow (*linear*), a pair of actuators on either side operate with a phase shift of 180° , whereas in a radially oscillating flow (*radial*) each piston pump

has a 90° phase shift to its adjoining pumps, see Table 4.1. The idea behind a radially oscillating flow pattern is to create a constant flow rate at the source that changes its flow direction by 360° within an oscillation cycle. This constant mass flow rate results from the accumulation of the four sinusoidal actuated flows. Thereby, constant high heat transfer rates can be expected, which result in minimized temperature fluctuations of the heat source, i.e., the microprocessor [11]. However, this requires more complex pumping installations. In a linearly oscillating flow, only one reciprocating pump would be required (push-pull piston).

The purpose of the present experimental study is to demonstrate the effectiveness of the above described self-contained, oscillating flow liquid cooling system. In the sections below experimental details and manufacturing issues will be discussed, followed by specific experimental results on the time-resolved and averaged hydraulic and thermal behavior, along with their analysis and discussions. Finally, specific conclusions will be drawn.

4.2 Device Fabrication, Experimental Apparatus and Procedure

4.2.1 Microchannel Cold Plates: HA & HD

Figure 4.2 shows the design of the absorber and dissipator microchannel cold plates which are manufactured in a *direct copper bonding (DCB)* process. Therein, $200\ \mu\text{m}$ thick copper sheets are patterned using photolithography and wet etching. A chemical oxidation process builds a defined copper oxide layer. Finally, the layers are stacked and fused at a temperature above the liquidus temperature of the oxide but below solidus temperature of the copper. This results in an interface-free bond because of interlayer grain growth [17], [18]. The manufacturing of the *DBC* microchannel cold plates was done by Curamik (Eschenbach, Germany).

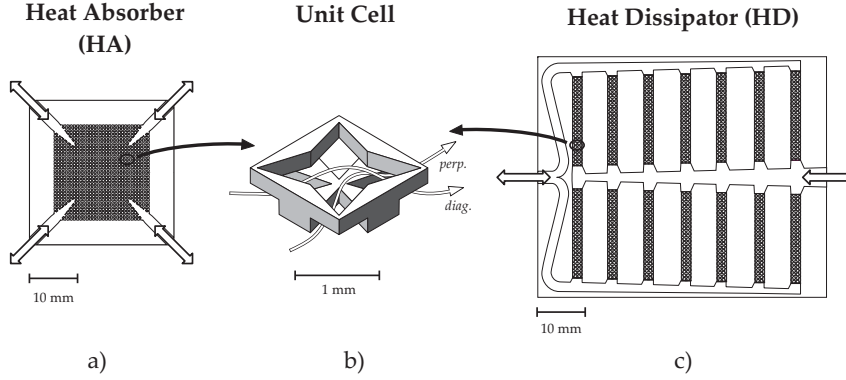


Figure 4.2: Microchannel cold plate design of a) the heat absorber (*HA*) and c) the heat dissipator (*HD*). The axially symmetric unit cell heat transfer mesh is displayed in b).

The *HA* cold plate, Fig. 4.2 a), is 30x30x2 mm³ with a heat transfer mesh base of 20x20 mm². By varying the aspect ratio of the microchannels a unit cell, see Fig. 4.2 b), three different mesh porosities

$$\varphi = \frac{V_{void}}{V_{cell}} \quad (4.2)$$

are realized. The three *HA* versions are referred to as *V1* ($\varphi_{V1} = 56 \%$, $V_{HA,V1} = 76 \mu\text{l}$), *V2* ($\varphi_{V2} = 52 \%$, $V_{HA,V2} = 81 \mu\text{l}$), and *V3* ($\varphi_{V3} = 46 \%$, $V_{HA,V3} = 85 \mu\text{l}$). To facilitate the generation of the flow patterns mentioned above (*linear* and *radial*), the layout of the *HA* and its corresponding heat transfer mesh create a four-fold symmetry (two diagonal and two normal planes). All four ports are identical, and fluid entering one port can exit the other three ports with a similar pressure drop. This is facilitated by the diagonal manifolds and guarantees a uniform flow distribution. The mesh layout is designed with respect to the unique nature of the radially oscillating flow pattern, cp. Fig 1.3. As it can be deduced from the mesh unit cell, Fig. 4.2 b), *perpendicular* and *diagonal* flow directions are ensured. In the case

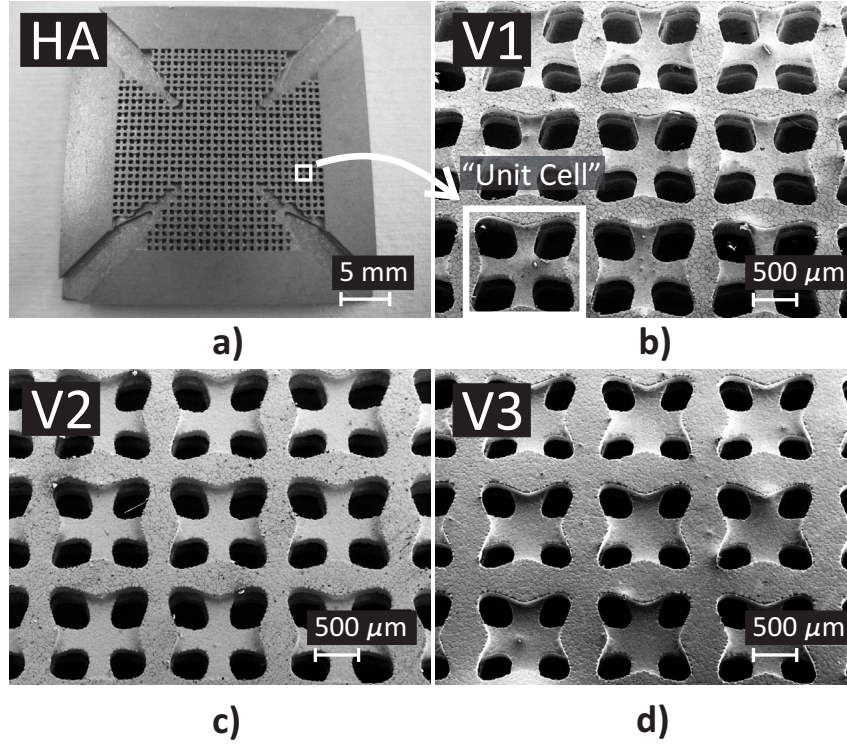


Figure 4.3: Photograph of the microchannel heat transfer mesh. a) displays the layout for the heat absorber *HA* with the covering top layer removed. b) - d) represent the cold plate mesh structure built up by stacking and duplicating the “unit cell”. The mesh porosities are $\varphi_{V1} = 56 \%$, $\varphi_{V2} = 52 \%$, and $\varphi_{V3} = 46 \%$.

of linear oscillations, the fluid flows only in horizontal direction. Herewith, the heat transfer mesh penalizes linear oscillations in a sense, so that it was possible to design it with a higher surface enlargement at similar frictional losses. Detailed discussions on the design and characterization of the different microchannel *HAs* presented here can be found in a previous publication [35]. Figure 4.3 depicts photoprahps of the manufactured copper microchannel cold plates.

For the peripheral heat dissipators *HD*, Fig. 4.2 c), a large area, low fluid volume cold plate is designed holding two inlet/outlet manifolds and multiple branching

channels. The microchannel heat transfer mesh, which is analogous to the one used in the *HA*, is placed in the branching channels. Each flow path has identical pressure loss, and the total inlet to outlet flow resistance is similar for the fluid entering from either side. The *HD* is 50x60x2 mm³ in size and contains $V_{HD} = 517 \mu\text{l}$ of fluid volume. The fluid volume ratio of *HD* to *HA* is 6; this illustrates the difference in power density the fluid has to absorb (*HA*) compared to its dissipation rate (*HD*). Furthermore, the *HD* can be designed with low hydrodynamic losses.

The interconnecting tubes between the *HA* and the *HDs* are 60 mm long and have a 2.5 mm diameter ($V_{tube} = 294 \mu\text{l}$). For flexibility reasons, polyethylene tubes were used. A leak-free connection between the tubes and the heat exchangers (*HA* and *HD*) is ensured by using slide-on copper adapters. They are soldered into the manifolds of the microchannel cold plates *HA* and *HD* after the *DCB* manufacturing.

4.2.2 Piston Pump Actuators

To carry out an accurate parametric study for different driving frequencies and volume displacements, a piston-type displacement pump is used. A frequency-controlled electric motor (maxon EC 32, maxon DEC 50/5, reduction gear 14:1) powers two disks via a T-type bevel gear (1:1 ratio). The disks feature boreholes with different eccentricities and angular positions. A double-acting hydraulic cylinder is connected to the eccentric locations of each disk and, therefore, creates a sinusoidal motion according to the rotary motion of the disks. Depending on the angular dislocation between the two disks the appropriate phase shift ϕ_i for radial or linear oscillations can be set, see Table 4.1. The piston area A_{PP} is 172 mm². In this work, four different pump strokes D_{PP} are studied, namely, 0.7, 1.0, 1.5, and 2 ml. We define the averaged flow rate of the oscillating liquid cooling system as

$$\dot{V} = 2 \cdot 2D_{PP} \cdot f \quad [ml/min], \quad (4.3)$$

representing the fluid volume passing the HA per cycle time. According to the liquid contents of the HA , the interconnecting tube, and the HD s, each of the four piston pumps displaces 42, 60, 90, and 120% of a quarter of the entire system volume (volume coverage D_{VC}), respectively:

$$D_{VC} = \frac{D_{pp}}{V_{HA}/2 + 2 \cdot V_{tube} + 2 \cdot V_{HD}} \cdot 100 \quad [\%]. \quad (4.4)$$

To emphasize the importance of the volume coverage D_{VC} , it is worth mentioning that as long as $D_{VC} > V_{tube}$ a fraction of the cooling fluid shuttles heat from the HA to the HD 's. If that is not the case anymore, the HD 's would be useless and the entire system would overheat immediately. The piston pump actuators presented in this work are aimed at establishing a well-controllable flow rate depending on frequency and stroke. Note, however, that this type of actuation is not practical for a real blade server type thermal management system, for which a fully hermetically sealed flow loop using membrane pumps would be a more likely scenario.

4.2.3 Experimental Setup and Data Reduction

An 18.6x18.6 mm² heater/sensor chip represents the blade server's power source to be cooled. Uniform Joule heating power (P_{chip}) of the entire surface A_{chip} is ensured by measuring current and voltage. Platinum resistance temperature detectors (RTD) are evenly distributed over the chip surface. The mean chip temperature $T_{j,mean}$ is determined by recording seven RTD s distributed over the entire chip base area and averaging over 50 measurements. $RTD1$ and $RTD4$, which are discussed later for the transient measurements, are located in the upper left corner and the center of the heater/sensor chip respectively.

External temperature measurements are taken using cold-junction compensated T-type thermocouples (TC) (Omega 5 SRTC-TT-(T)I-40-1M, NI SCXI-1102). The

fluid temperature T_{fluid} between HA and HD is measured by placing a TC in one of the four interconnecting tubes. The temperature T_{base} is measured between HD and CP by means of thermocouples that are placed in small grooves that have been cut into the top side of the CP .

The system pressure loss is detected using a pressure transducer (Omega PD 23), which determines the amplitude of the pressure oscillations (atmosphere as a reference). The pressure sensor is located at the far end of the primary heat transfer loop, next to one of the double-acting hydraulic cylinders, cp. Fig. 4.1 a). The difference between the extremes is identified, and the root mean square (RMS) value defines the average pressure drop of the oscillating flow loop, i.e. $HTL1$:

$$\Delta p = \frac{\sqrt{2}}{2} \cdot (p_{\max} - p_{\min}) \quad (4.5)$$

As mentioned above the secondary heat transfer loop ($HTL2$) collects heat from the primary heat transfer loop ($HTL1$). The collector planes (CP) are thermally connected with the heat absorber (HD) using thermal interface paste (Dow Corning TC-5026). The four CP s are customized, straight channel, low aspect ratio solid-to-liquid heat exchangers. Correspondingly, we cut 40 channels (width 0.5 mm, pitch 1.25 mm, length 60 mm, and depth 6 mm) into solid brass. An inlet and outlet manifold ensures uniform fluid flow rate distribution across the channels. However, in an air cooled blade module, the CP s would be represented by air fin heat exchangers. For all experiments presented in this work a chiller (Lauda Proline RP 855, $\pm 0.01^\circ\text{C}$ FS) delivers cold water ($T_{in} = 18^\circ\text{C}$) at a constant flow rate of $\dot{V}_{HTL2} = 600$ ml/min (flow rate sensor: Omega FLR 1000, accuracy: $\max \pm 2\%$ FS). In this paper, the $HTL2$ part of the experimental setup acts solely as a thermal ground and is not discussed in more details. However, the total interface-to-inlet thermal resistance amounts to approximately 0.2 K/W for an area of $A_{cp} = 30$ cm². This is

again discussed later in the results section.

Two samples of each heat absorber cold plate version (*HA V1*, *V2*, and *V3*) are tested, with the corresponding sets of piston pump frequencies f and displacements D_{PP} . The *HAs* are connected thermally to the heater/sensor chip at low thermal resistance utilizing high conductive thermal paste (Dow Corning TC-5026) and a clamping device. The contact pressure is kept constant resulting in $R_{TIM} \cdot A_{chip} = 12 \text{ K mm}^2/\text{W} \pm 8\%$.

For the filling procedure, *HTL1* is first flushed for several minutes using an external water loop (deionized water) to remove trapped air bubbles inside the fluid flow system. Next, the external water loop is turned off and *HTL1* closed to become self-contained. The cooling cycles are digitally controlled and data is acquired using a personal computer, corresponding data acquisition hardware and LabVIEW software.

The data obtained from voltage, current, temperature, flow rate, and pressure measurements were reduced to power, thermal resistance, and hydraulic power. The total thermal resistance (R_{tot}) is the sum of components that account for conduction through the silicon substrate and the *TIM* (R_{Si+TIM}), convection to the fluid at the *HA* (R_{HA}), and liquid-to-liquid convection from the *HD* to the *CP* ($R_{HD}+R_{CP}$):

$$R_{tot} = R_{Si+TIM} + R_{HA} + R_{HD} + R_{CP} = \frac{T_j - T_{in}}{P_{chip}} \quad [K/W], \quad (4.6)$$

according to the quadratic error propagation the measurement uncertainty being $\sigma_{R_{tot}} = \pm 4\%$. The hydraulic power defines the pumping power needed to overcome the system pressure at a given flow rate

$$P_{fluid} = \Delta p \cdot \dot{V} \quad [W] \quad (4.7)$$

Here, the measuring inaccuracy is $\sigma_{P_{fluid}} = \pm 5\%$.

4.3 Results and Discussions

4.3.1 Fluidic Performance

The oscillation frequency adopted in this work is $0.5 \leq f \leq 3$ Hz. Lower frequencies lead to poor thermal performances for the pumps strokes studied in this work. However, frequencies $f > 3\text{Hz}$ lead to pressure forces that are not manageable for the piston pumps utilized. Moreover, the pressure level has to be limited to a certain limit, e.g. $p < 2$ bar, to be feasible for a pump-driven water cooling system, otherwise the pump power becomes too high.

For oscillatory flows, the transition from a laminar to a turbulent regime differs substantially from steady-flow conditions. Instead of the Reynolds number, the Womersley number $\alpha = D/2 \cdot \sqrt{\omega/\nu}$ and the transition number $\beta = \Delta x \cdot \sqrt{\omega/\nu}$ are used. The variables D , ω , ν , and Δx denote the channel width, the angular velocity, the dynamic viscosity of the fluid, and the maximal axial displacement of the fluid elements, respectively. By recognizing $\sqrt{\nu/\omega}$ as the well-known Stokes-layer thickness due to pure oscillations, the Womersley number α is the ratio of the geometrical half height to the Stokes-layer thickness, and represents a frequency parameter. On the other hand, the transition number β , which has often been used in the oscillatory-flow literature as an indicator for the laminar-turbulent transition, represents the ratio of the tidal displacement to the Stokes-layer thickness. According to Kurzweg, *et al.* [61], for $\alpha \approx 1$, turbulent flow occurs for $\beta > 3000$. However, a wide range of transition numbers β has been reported [62], [63], [64]. The frequency and flow range tested in this work results in $0.8 \leq \alpha \leq 3$ and $80 \leq \beta \leq 562$. Therefore we assume a laminar flow regime inside the microchannel heat exchangers.

Depending on the fluid displacement D_{PP} , the frequency was set between 0.5 and 3 Hz. For higher frequencies f and displacements D_{PP} , the pressure drop in the system and the power to drive the piston pump become too high, i.e., $\Delta p \geq 2$

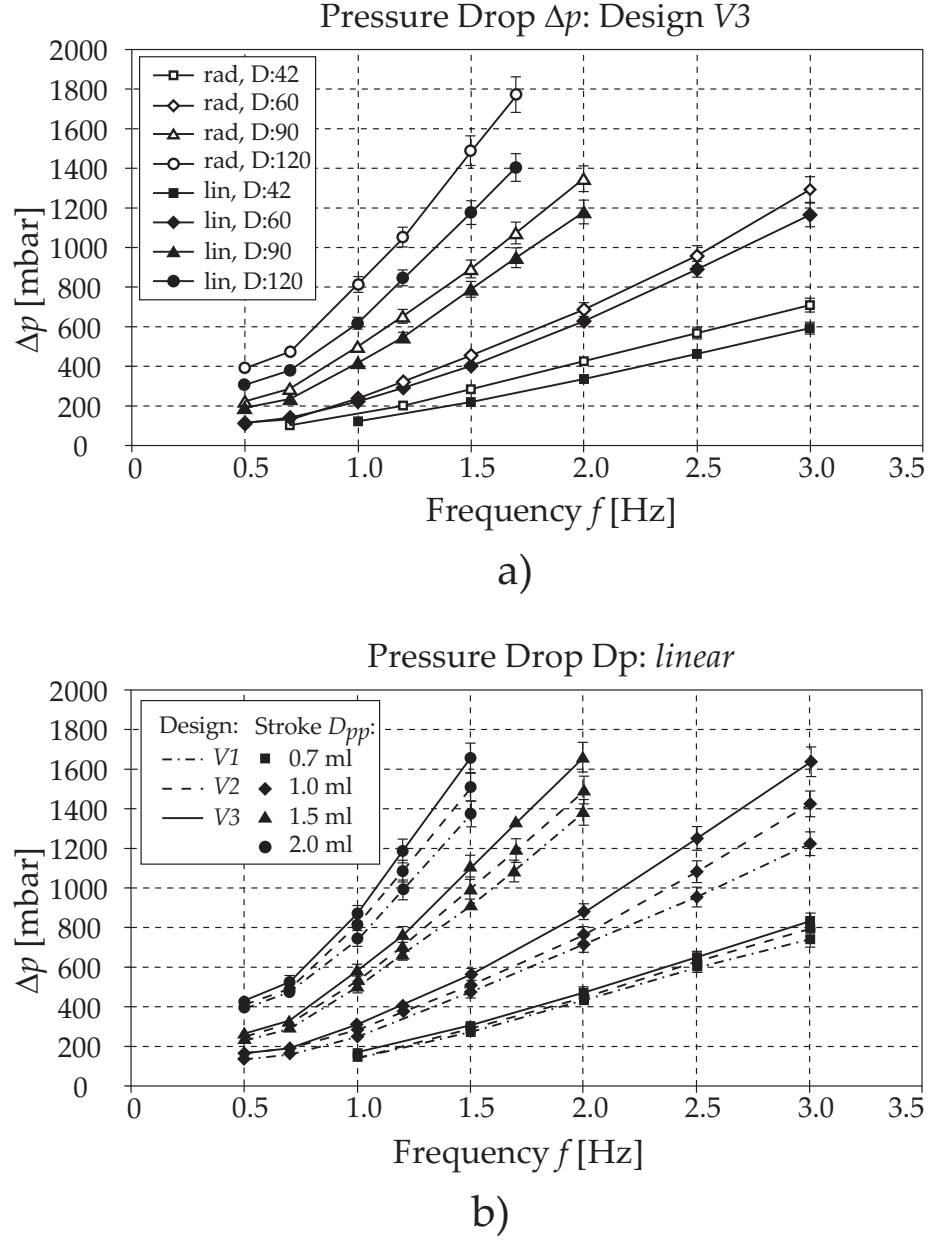


Figure 4.4: Averaged (root mean square) pressure drop: a) for V3, various flow patterns (*lin* = *linear* and *rad* = *radial*), pump displacements D_{PP} , and frequencies f . b) for various absorber designs V_i , pump displacements D_{PP} and frequencies f .

bar. Frequency-dependent pressure drop data with *HA V3* for *linear* and *radial* oscillation flows are shown in Fig. 4.4 a). The comparison of the three different designs *V1*, *V2*, and *V3* for linear oscillation flow is presented in Fig. 4.4 b). For both flow patterns, the pressure oscillations follow a clearly sinusoidal behavior. Furthermore, when plotting the pressure drop against flow rate, the data points for various pump strokes collapse to a single curve. Therefore, we legitimate the decision to define the mean hydraulic losses according to Eq. 4.5.

linear exhibits a significantly lower pressure drop than *radial*. For $D_{PP} = 0.7$ ml the pressure drop in *linear* flow varies between 100 and 800 mbar depending on the frequency, and for $D_{PP} = 2$ ml, it ranges from 300 to 1400 mbar. For a given frequency f , displacement D_{PP} , and absorber design V_i , *radial* outperforms *linear* by 15 to 25%, cp. Fig. 4.4 a). This can be explained by the fact, that in radial oscillation flow the fluid momentum forces per cycle are higher. The flow is less directed and more fluid mixing occurs. For example in the *HA*, the liquid experiences four primal changes of the planar flow direction per cycle when driven in *radial* flow, but only two in *linear*.

Concerning the three different mesh porosities *V1*, *V2*, and *V3* the pressure drop reflect the mesh density, cp. Fig. 4.4 b). Except for the case of $D_{PP} = 0.7$ ml, the hydraulic losses for *V3* are 20% higher than those for *V1*. As will be shown later, a higher heat transfer rate can be achieved at the expense of higher pumping power.

4.3.2 Thermal Performance

As mentioned above, the Womersley number for the entire frequency range is $0.8 \leq f \leq 3$. Small Womersley numbers ($\alpha < 1$) result in quasi-steady flow with oscillatory parabolic velocity profiles. In turn, large α -values ($\alpha > 10$) lead to the “Richardson’s annular effect”, which results in near-wall velocity overshoots (plug-like velocity profile) where the peak velocity no longer occurs in the symmetry plane of the

channel [65], [66]. In the present work, the oscillation flow regime is in the transition zone between a parabolic and a plug-like velocity profile. Therefore we do not expect an enhanced convective heat transfer owing to a lower velocity boundary layer thickness. Theoretically, for $f > 4$, $\alpha > 10$ could be reached. However, because of the limited mechanical stability of the pumps, the tidal displacement had to be reduced to $D_{PP} < 0.7$ ml. This in turn is insufficient to displace a fluid element from HA to HD in one stroke and leads to a reduced overall thermal performance.

Time-Resolved Measurements Figure 4.5 shows the temperature oscillations at various locations ($RTD1$, $RTD4$, T_{fluid}) over two cycles for HA $V2$ and a fixed frequency of 1.5 Hz. All measurements were carried out at identical heating power $P_{chip} = 235$ W. The parameters for the secondary heat transfer loop comply with the descriptions given above. $RTD1$ is located in the corner of the heater/sensor chip, i.e., below the opening manifold of the HA . $RTD4$ is slightly offset from the center of the chip, and T_{fluid} is measured inside one of the tubes between HA and HD . In all subplots, the position of the piston pump (solid line) is shown in arbitrary units. A change from low to high values signifies that the pump pushes fluid across the HA through the tube to the corresponding HD . The temperature cycling demonstrates the dependency of the heat transfer rate on the fluid flow rate. High flow rates lead to a higher convective heat transfer coefficient, hence, to lower temperatures and lower inflow/outflow amplitudes, and vice-versa. In the *linear* flow mode, Fig. 4.5 a), the temperature exhibits two minima and maxima values per cycle. This is due to the fact that the flow rate peaks twice per cycle (zero crossing of the piston position). The two minima are different (e.g. in Figure 4 a) 62 and 65 °C for $D_{PP} = 0.7$ ml) because the flow can be directed *from* (*outflow*, ‘hot’) or *to* (*returnflow*, ‘cold’) the heat source HA . The RTD temperature amplitude decreases with increasing stroke D_{PP} , e.g., for $RTD4$, *linear* decreases from 5 to 2.5 K. The slight phase shift between

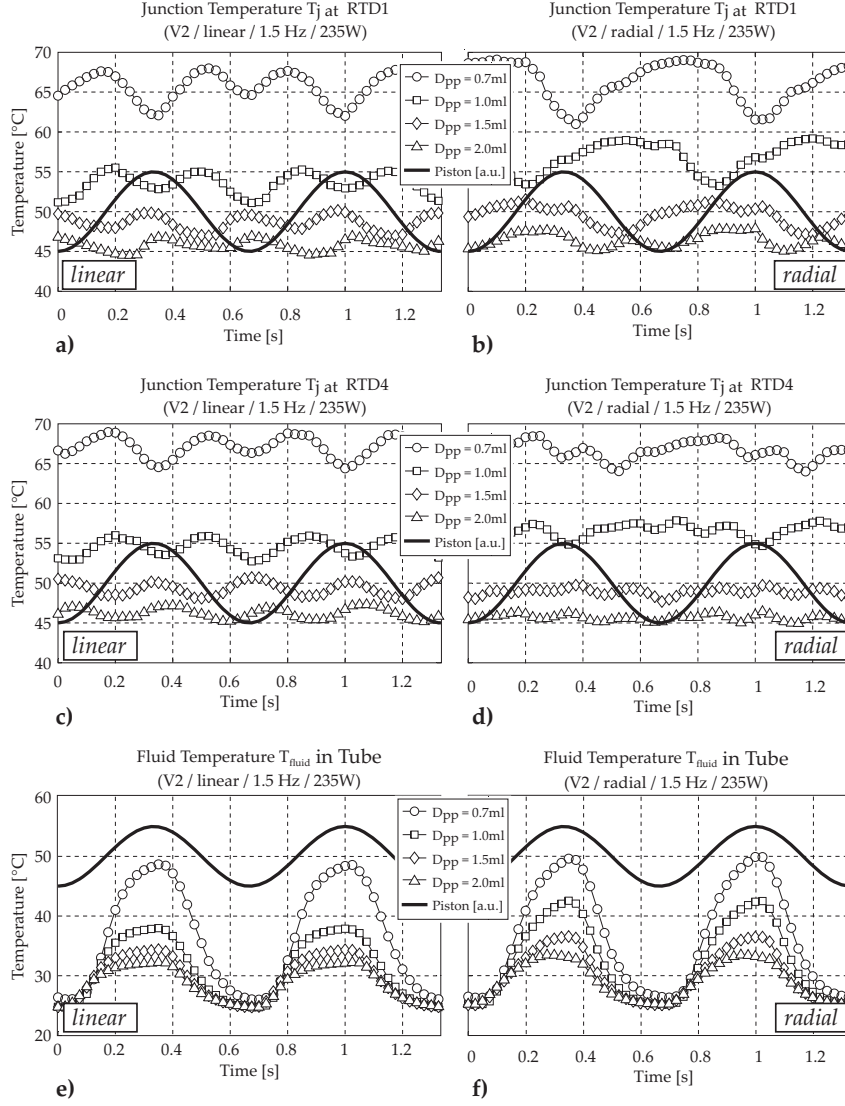


Figure 4.5: Temporal temperature oscillations over two cycles at for *HA V1*, $P_{chip} = 235$ W, and $f = 1.5$ Hz: Panels a)-d) show the chip temperature at two different locations (RTD1: corner region, RTD4: center region) and flow patterns. Panels e)-f) give the fluid temperature in the interconnecting tube between the absorber and the dissipator cold plates.

the piston position signal and the *RTD* temperature is explained by the thermal time constant of the chip/cold plate assembly. Depending on the convective heat transfer rate, the thermal time constant is of the order of $\tau = 0.1 - 0.3s$ [23, pp. 240].

In *radial* flow, Fig. 4.5 b) and d), the *RTD* temperature oscillations follow a different characteristic compared to *linear*. For *RTD1*, which is located at the corner, the ‘hot’ period is much more pronounced compared to *linear*. Only in one quarter of the pumping cycle does *returnflow* from the *HD* occur. The second temperature minimum, as detected for *linear*, is only identifiable for $D_{PP} = 2.0$ ml. The *RTD1* temperature amplitude is significantly higher for *radial* compared to *linear*, i.e., 40 - 60%, leading to a higher average temperature. For radial oscillations, however, *RTD4* exhibits slight benefits compared with linear oscillations. The average temperature is similar, whereas the temperature amplitude can be reduced by adopting radial oscillation flows. For *RTD4* and $D_{PP} = 2.0$ ml, the amplitude is 1 K for *radial* and 2.5 K for *linear*. This, in turn, is the only example in the present work in which radially oscillating flows are advantageous over linearly oscillating flows. Locations away from the center (here represented by *RTD4*) realize a non-symmetric flow regime over a pump cycle in *radial* flow. Pure *returnflow* as described above only occurs during a fourth of a pump cycle. We conclude that a constant, but radially oscillating flow regime could only be established in the very center of the available *HA* cooling device. Although a design change might improve the situation, it is in the nature of the *radial* flow principle to transform to a periodic flow characteristic as the point of interest moves away from the center.

Fig. 4.5 e) and f) illustrates the measured temperature of the thermocouple inserted into the tube between *HA* and *HD*. Again, the solid line describes the piston pump position. The phase shift between fluid displacement and fluid temperature is close to zero, because the heat transfer is dominated by heat advection (negligible thermal mass of thermocouple tip, $\tau \approx 4$ ms). The temperature is high when fluid flows from

HA to *HD* (*outflow*), and low in the inverse direction (*returnflow*). Depending on the pump displacement, the *outflow-returnflow* temperature difference varies between 8 and 25 K. For fixed displacements D_{PP} , the measured fluid temperature is always higher for *radial* than for *linear*. Moreover, in linear oscillation *outflow*, Fig. 4.5 e), a ceiling temperature can be determined for $D_{PP} \geq 1.0$ ml. This is an indication of a full fluid displacement from one side to the opposite side. In contrast, this is not the case for radial flow. Therefore, we deduce a poorer heat shuttling capability for radially oscillating flow than for linearly oscillating flow. After exchanging heat with the *HD* and flowing back to the *HA*, the fluid temperature levels at about 25 °C. Except for $D_{PP} = 0.7$ ml, the variation in *returnflow* temperature for the different flow patterns or pump strokes is negligibly small. This indicates that together the heat dissipator cold plate and the collector plane have a small thermal resistance.

Time-Averaged Measurements Next, we compare the time-averaged thermal performance for the different *HA* designs and flow patterns for a fixed pumping power P_{fluid} , Eq. 4.7. Figure 4.6 discusses how the total thermal resistance R_{tot} depends on the volume coverage per stroke D_{VC} , Eq. 4.4. The experimental data are fitted using a power function of the form

$$R_{tot}(D_{VC}) = a \cdot D_{VC}^b + c. \quad (4.8)$$

It contrasts the linear oscillation and the radial oscillation flow pattern at 0.5 W, Fig. 4.6 a), and 1.0 W, Fig. 4.6 b). First, a clear dependence on the pump power is evident, i.e., a larger volume coverage per stroke, D_{VC} , leads to a better cooling performance. However, R_{tot} approaches an asymptotic value towards $D_{VC} = 120\%$ for linear oscillations. From Eq. 4.8, the asymptotic value of the total thermal resistance R_{min} can be determined considering the parameter γ . When comparing the volume coverage theoretically required to approach R_{min} by 5 %, we find D_{VC}

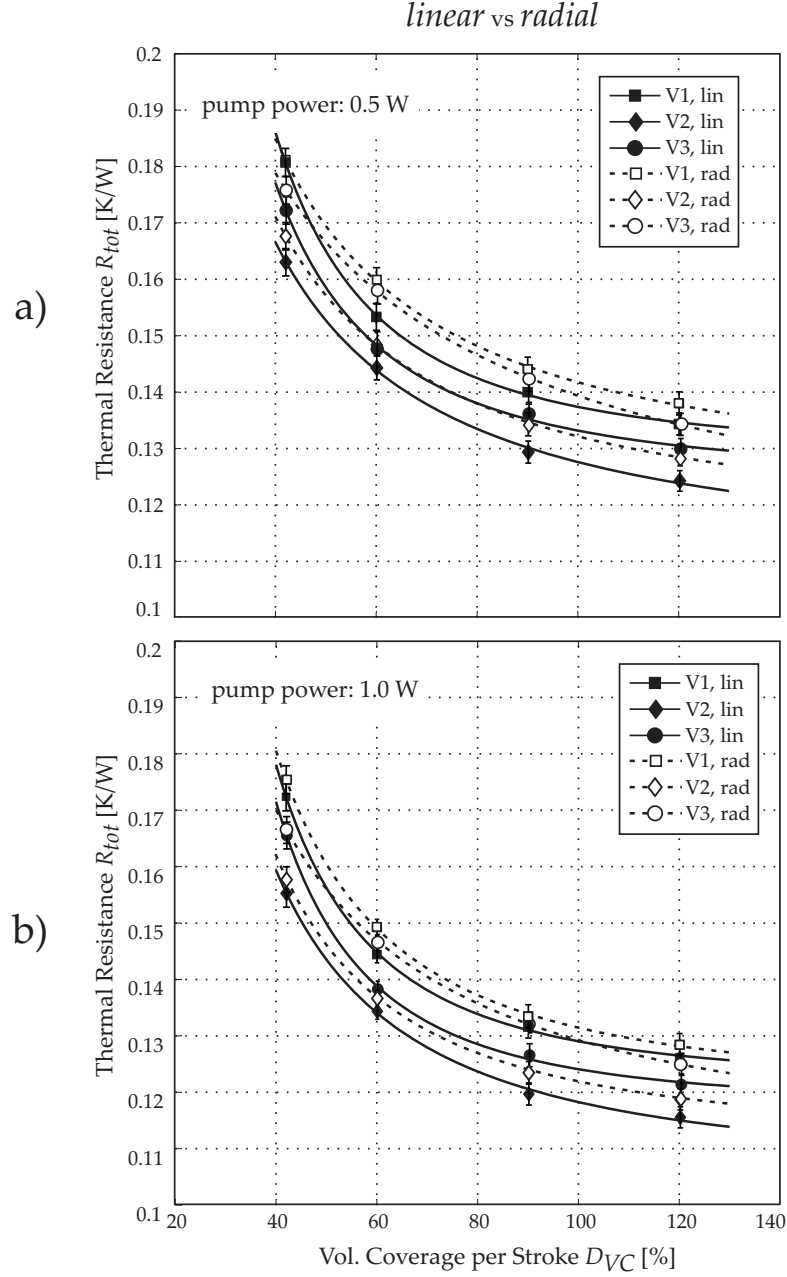


Figure 4.6: Dependence of the averaged thermal resistance of the different flow patterns (*lin* = *linear*, *rad* = *radial*) and heat absorber mesh designs (*V1*, *V2*, *V3*) on the fluid pumping power (a) at 0.5 W and b) at 1.0 W).

= 100 - 120% for *linear* and $D_{VC} > 250$ % for *radial*. Concerning the pump strokes D_{PP} tested in this work, this range has only been achieved for *linear*. Again, this shows that heat spreading is much more effective for linearly oscillating flows than for radially oscillating flows. For all fluid displacements D_{VC} , *linear* performs better than *radial*. As shown in the hydraulic performance section, the radially oscillating flow exhibits higher hydraulic losses. This is the main reason for the performance difference seen in Fig. 4.6. However, when considering the flow rate as the independent variable, the discrepancy between the two flow regimes in terms of thermal resistance is marginal and not identifiable within the measuring error. We conclude that for a constant flow rate, the two oscillation patterns compared in this work perform equally well. However, because of a higher pressure loss more pumping power is needed for radially than for linearly oscillating fluid flows. Furthermore, a self-contained, liquid cooling system with linearly oscillating fluid flows can be established using only one reciprocating pump in conjunction with a spring-type fluid reservoir on the opposite side of the heat spreading system.

Comparing the three different *HA* mesh designs one can see an optimum for *V2* for the entire pump displacement range presented here. Typically, for steady, laminar, and developing flows in a microchannel it holds that $Nu \propto Re^\kappa$, $\kappa \approx 0.5$ and $\Delta p \propto Re^\kappa$, $1.7 \leq \kappa \leq 2$ [35], therefore, $Nu \propto \Delta p^\kappa$, $\kappa \approx 0.3$. *V2* exhibits an optimum combination of thermal and hydraulic performance among the mesh designs presented in this work. Furthermore, the thermal performance of the cooling system presented here reaches an asymptotic value of $R_{tot} = 0.11$ K/W which corresponds to a maximum chip power density of 180 W/cm^2 at $T_{j,max} - T_{in} = 67 \text{ K}$ ($T_{j,max} = 85^\circ\text{C}$, $T_{in} = 18^\circ\text{C}$). T_{in} is the chiller-controlled inlet fluid temperature of the secondary heat transfer loop *HTL2*.

4.3.3 Oscillating Flow versus Steady Flow²

As described in the introduction, Ch. 1.2, the blade-level cooling loop could also be designed in a uniform flow configuration. By replacing the reciprocating pumps with a constant feed pump, a similar fluid flow loop within the blade can be established. However, the absorber cold plate *HA* and the large-area dissipator cold plates *HD* have to be connected in series together with the rotary pump. This adds some additional piping to the flow loop since the liquid has to feed back into the cold plate system once it passed through it.

In order to compare an oscillating-flow loop with a uniform-flow loop, the same cooling devices are utilized and the total active heat transfer area is kept constant. The fluidic losses for the steady-flow configuration include the additional piping. Thus, the system pressure drop is defined by measuring the differential pressure after and before the pump, but does not include the pressure losses across the respective flow meter.

Figure 4.7 depicts the fluidic and thermal performances of the current oscillating flow loop in linear and radial mode, and the uniform-flow loop as described before. In all cases, the microchannel heat transfer mesh design *V1* is employed. The volumetric flow rate in the oscillating configuration is calculated as defined in Eq. 4.3, whereas the steady-flow rate is measured using a corresponding flow rate sensor (Omega FLR 1000). At a given volume flow, the frictional losses are significantly higher in the steady-flow compared to the oscillating-flow regime. At a reference flow rate of 0.5 l/min, *linear* exhibits 800 mbar, *radial* 1000 mbar and steady-flow 1600 mbar pressure loss. This refers to an increase of 25 and 100% for *radial* and steady-flow compared to *linear*, respectively. The situation is not that prominent when comparing the thermal performances of the different configurations. The experimental measurements show that the linearly oscillating flow pattern performs

²This section is not published in [44].

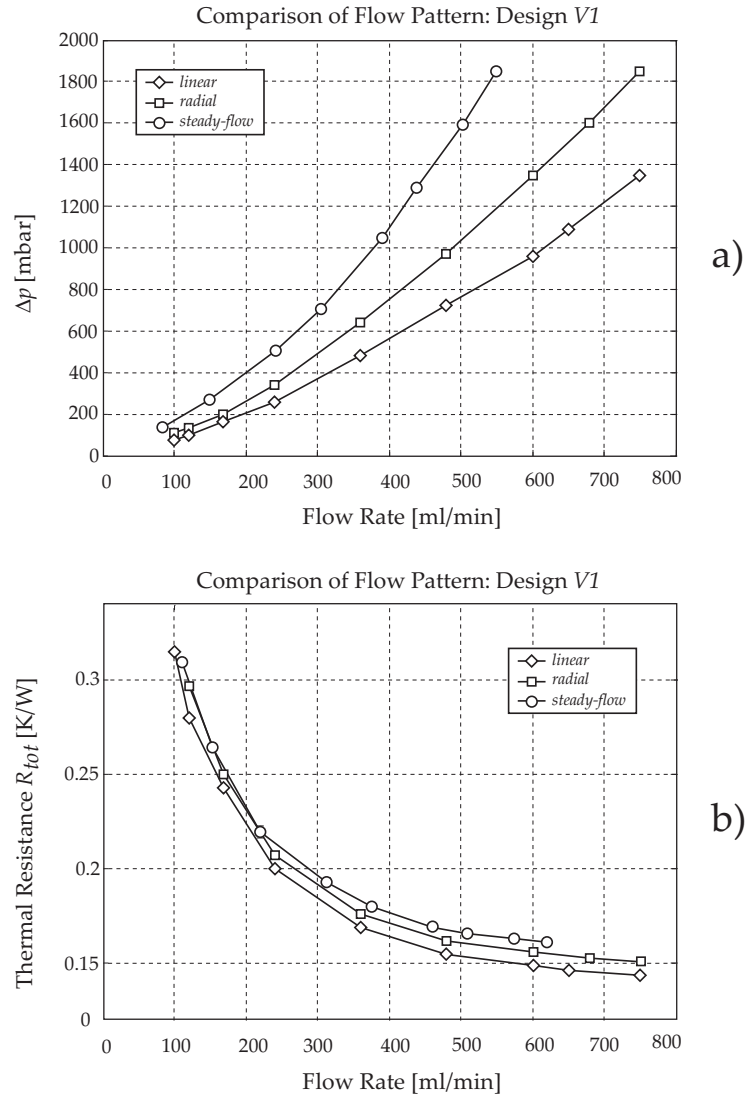


Figure 4.7: a) Fluidic and b) thermal performance comparison of a blade-level heat spreading system in either oscillating (*linear*, *radial*) or uniform flow configuration.

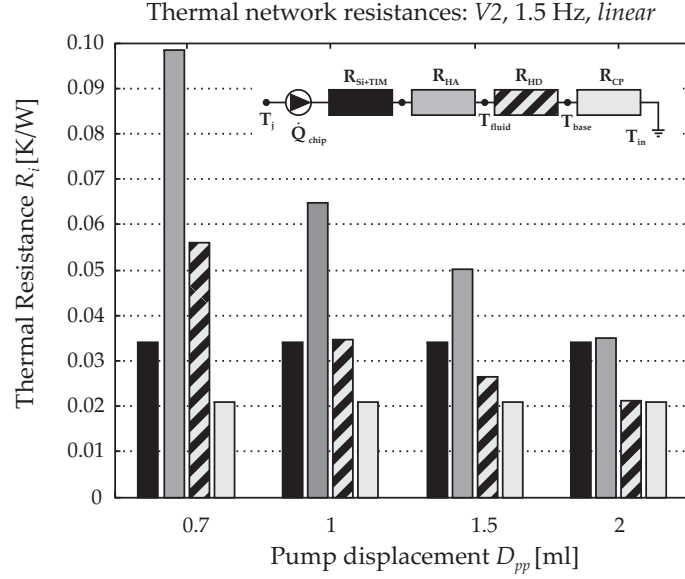


Figure 4.8: Division of the overall thermal resistance into a simplified linear resistor network including R_{Si+TIM} , R_{HA} , R_{HD} , and R_{CP} .

better than the radially oscillating flow pattern, and the steady flow loop exhibits the least cooling capacity. The improvement is in the range of 8% for *linear* compared to steady-flow. This is explained with the advantage of the plug-like flow profile established in the oscillating fluid flow regime. The net frictional losses and the boundary layer thicknesses are smaller in the oscillating compared to the uniform flow.

Owing to the smaller piping system and the elimination of the expansion reservoir, the oscillating fluid flow heat spreading loop can be designed in a highly compact manner. Thus, it has been demonstrated, that the fluid volume can be limited to several milliliters. The prototype presented in this work manages on a total volume of roughly 10 ml (including the piston pump cylinders).

4.3.4 Thermal Budget of Single Cooling Components

We finalize the results discussions with a subdivision of the total thermal resistance R_{tot} into an elemental linear resistor network (cp. insert Fig. 4.8). Therefore we employ time-averaged temperatures T_i and a constant heat flux \dot{Q}_{chip} to calculate the resistor elements of the heat absorber R_{HA} , the heat dissipator R_{HD} , and the collector plane R_{CP} :

$$R_{Si+TIM} + R_{HA} = \frac{T_{j,mean} - T_{fluid}}{P_{chip}}, \quad R_{HD} = \frac{T_{fluid} - T_{base}}{P_{chip}}, \quad R_{CP} = \frac{T_{base} - T_{in}}{P_{chip}}$$

$$R_{tot} = R_{Si+TIM} + R_{HA} + R_{HD} + R_{CP} \quad [K/W]. \quad (4.9)$$

The interface resistance between the heater/sensor chip and the HA as well as the measurement of the different temperature levels have been discussed above. The interface resistance including conduction resistance in the silicon amounts to $R_{Si+TIM} = 0.034 \text{ K/W}$. In fact, four identical, parallel heat current resistor paths branch off from R_{HA} , each one dissipating a quarter of the total power input. This can be simplified to a single linear resistor network as presented in insert of Fig. 4.8. The elemental thermal resistances for $V2$, $f = 1.5 \text{ Hz}$, are presented as a function of the pump displacement D_{PP} , Fig. 4.8. Again, for a larger flow rate ($D_{PP} \uparrow$) the heat absorber cold plate resistance R_{HA} decreases, which also holds for R_{HD} . However, R_{CP} is independent of the primary flow rate, which is expected since the flow rate of the secondary heat transfer loop ($HTL2$) is kept constant for all results presented herein. This could be verified by the experimental measurements presented in this work. It is important to note that with $R_{Si+TIM} + R_{HA} \approx 0.65 \cdot R_{tot}$, the chip to fluid heat transfer resistance contributes the most to the overall thermal performance of the present cooling system. Therefore, because of an effective heat spreading from the hot chip to a large area, the heat exchangers of $HTL2$ can be designed in a simple manner. Here, we have chosen low aspect ratio, straight-channel cold plates.

As mentioned at the beginning, this design could also be replaced by air-fin heat exchangers.

4.4 Summary and Conclusions

We have experimentally demonstrated a high performance thermal management concept for thin form-factor electronic equipment such as a blade server module. By means of a self-contained, reciprocating fluid flow loop, a four-port microchannel cold plate absorbs heat (HA) and delivers the hot fluid via interconnecting tubes to four peripheral dissipating cold plates (HD). There, a periodic heat transfer to a secondary heat transfer loop takes place by thermally attaching the dissipating cold plates to a fluid heat exchanger collecting plane (thermal bus).

To create the fluid oscillations, four piston pumps are actuated, and depending on the phase shift, different oscillation flow patterns (linearly oscillating, *linear*, and radially oscillating, *radial*) can be created. The fluid displacement is between 0.7 and 2.0 ml, i.e., 42 to 120% fluid volume coverage per stroke. Depending on the pump stroke, the oscillation frequency ranges between 0.5 and 3 Hz. Higher frequencies cause unacceptably high pressure losses. Three different heat absorber cold plate designs with varying mesh porosities were tested.

The fluidic performance studies show a significantly lower pressure drop for *linear* than for *radial* (15-25% difference). For *radial*, the fluid changes its flow direction more frequently per pumping cycle, which results in higher momentum forces. Regarding the different heat absorber mesh designs, the densest ($V3$) features 20% higher pressure drop than the coarsest ($V1$). For a flow range of 100-800 ml/min, the pressure losses are between 100 and 1200 mbar.

Thermal characterization is performed taking time-resolved and time-averaged measurements. The chip *RTD* sensors capture the fluid flow oscillations over time. A

larger tidal displacement of the piston pump leads to a smaller temperature amplitude. In linear oscillation flow, two temperature minima and maxima per pumping cycle are found. For radial fluid oscillations, the cooling performance is less efficient: corner regions of the chip exhibit larger temperature cycling and only a small spot in the very center of the chip is cooled more efficiently where the junction temperature is close to constant.

At 1.5 Hz the fluid temperature measured in the interconnecting tube fluctuates between 8 and 25 K, depending on the pump stroke. In *linear*, a ceiling temperature can be determined for at least half the time of the outflow phase. This indicates uniform heat transfer. In *radial*, the heat absorber gets flushed less uniformly.

The averaged thermal performance of the cooling system presented here exhibits a clear dependence on the pump displacement. We have demonstrated a peak cooling performance of 180 W/cm^2 at $\Delta T = 67 \text{ K}$ and a pumping power of 1 W. In *linear*, a pump displacement covering the fluid volume by 100 - 120% achieves a performance roughly 5% above the theoretical minimum thermal resistance. Of the three *HA* designs tested herein, the medium-density mesh performed best ($\varphi_{V2} = 52\%$). The optimum is found as a compromise accounting for both, high heat transfer rate and low hydraulic losses, resulting in the best ratio of heat transfer per pressure drop.

A reciprocating pump flow system as presented here is simpler in terms of equipment and more efficient when operated in a linearly oscillating flow mode. The heat spreading from a small source to a large area is more effective at a given pumping power.

A direct comparison of an oscillating flow and a uniform flow loop depicts the advantage of a self-contained, hermetically sealed oscillating flow pattern. While the total thermal resistance is lower by 8%, *linear* exhibits a pressure loss advantage of >50% compared to the *steady-flow* configuration.

5 Effectiveness of a Radially Oscillating Liquid Heat Spreading System¹

Abstract

The radially oscillating flow hybrid cooling system, in the following referred to as RADIOS, provides a thin form factor cold plate with radial spreading of heat to a larger area. A small liquid volume ($<10\text{ ml}$) is hermetically sealed within the system and does not require external hose connections. Four membrane pumps running in a phase-delayed manner induce a constant-speed, oscillating direction fluid flow at the chip source that continuously shuttles heat to an extended periphery and returns cool liquid to the chip. In the peripheral branches, heat is transferred from the liquid to solid structures and finally dissipated to the air. A micro-scale copper mesh enables low-resistance heat transfer (solid-liquid and liquid-solid) in a thin form factor ($<2\text{ mm}$). Narrow channels between the discrete heat exchanger areas optimize the spreading performance and reduce the fluid volume. Numerical modeling shows an effective conductivity of $20X$ and $50X$ over bulk copper for the spreader plates and the interconnecting tubes, respectively. The technology presented here promotes modular liquid cooling units for low-profile computing systems without incurring the risk of flooding associated with conventional liquid cooling circuits.

¹This Chapter is published in: R. Wälchli, et al., “Radially Oscillating Flow Hybrid Cooling System for Low Profile Electronics Applications”, *24th Annual IEEE Semiconductor Thermal Measurement and Management Symposium*, 2008, San Jose, CA

Nomenclature

ΔT	Temperature difference [K]
A	Cross-sectional area [m ²]
A_{act}	Piston cross-section of actuator [m ²]
C_p	Specific heat [J/(kg K)]
Cu	Copper
D_{act}	Volume displacement of actuators [ml]
f	Actuator frequency [Hz]
h	Heat transfer coefficient [W/(m ² K)]
N	Number of actuators in system [-]
R_{th}	Thermal resistance [K/W]
T_{amb}	Ambient temperature [K]
T_j	Transistor junction temperature [K]
V_{act}	Volume displacement (zero-to-peak) [m ³]
λ	Thermal conductivity coeff. [W/(m K)]
λ_{Cu}	Thermal conductivity coeff. of copper [W/(m K)]
ϕ	Phase shift of actuators [rad]
Ω	Simulation domain
Ω_s	Constant heat flux surface
Ω_q	Constant heat transfer coeff. surface []

5.1 Introduction: Transition to Liquid Cooling

With continuous increase in transistor density and power dissipation of high-end computing systems, efficient and low-cost cooling solutions will be crucial to enable further performance improvements. Without a fundamental change in microprocessor architecture, power densities will approach 150 W/cm^2 within the next years [67],[68]. Without the development of low-resistance spreading technologies, the air-cooling capacity is limited to approximately 100 W/cm^2 [55]. Classical liquid cooling has been proposed and implemented for cooling of high-end bipolar machines. Removal of very high power densities by microchannel liquid cooling was first technically demonstrated in [6] and recently re-introduced and implemented for cooling of CMOS chips [9],[8] with power densities $>350 \text{ W/cm}^2$.

Every chip cooling technology aims at transporting heat to a larger area, where it can be exchanged to ambient air. Heat spreading from a small source to a larger area via conduction adds a considerable amount of resistance to the entire thermal path [31],[69]. To reduce the spreading resistance in the base of an air heatsink, heat pipes and vapor chambers are utilized in most of the computing systems. To optimally use the passive driving characteristics, vapor chambers are designed for a particular power flux close to the critical heat flux. This results in a higher thermal resistance for low heat fluxes and the risk of drying out for very high power densities [70]. Furthermore, vapor chamber cooling systems must be positioned right to operate at maximum performance. This limits the freedom of design and flexibility to implement it in various electronic systems.

Liquid cooling solutions can be built to be more compact than air cooling solutions because of the higher heat capacity of the coolant. An implementation in a data center, however, requires additional equipment, e.g. water supply and piping, usually not present in newer computing centers. In addition, the risk of flooding and

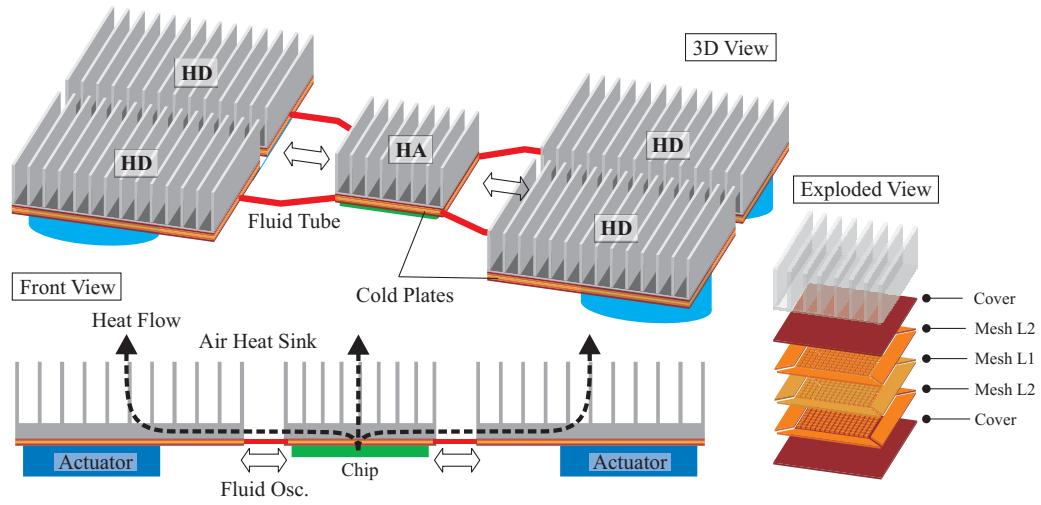


Figure 5.1: Cooling principle: membrane actuators pump liquid through a system of micro-machined copper plates and tubes to spread heat to a larger area. The fluid in the heat absorbers (HA) takes up heat from the chip, shuttles it to the peripheral cold plates in a periodic manner, where heat is exchanged with air via the heat dissipators (HD) and air fins.

the complexity and cost of integrating large fluid networks have prevented the re-introduction of liquid cooling in commercial CMOS systems.

This opens up an opportunity for integrated systems that make use of the performance of liquid cooling, but reject the heat to air like in conventional air cooling. The technology presented here aims at solving all the aforementioned issues of cooling electronics equipment. RADIOS represents a small cooling system integrated in the base of an air heatsink to efficiently spread heat from the source to a larger area.

5.2 RADIOS - Technology

5.2.1 Flow Principle and Driving Scheme

The **radially oscillating** flow hybrid cooling system, in the following referred to as **RADIOS**, is a self-contained, thin form factor heat spreader in direct contact with the microprocessor. Figure 5.1 displays a schematic section cut of the technology: To reduce the spreading resistance to a larger area, the RADIOS heat spreader plates are integrated into the base of an air heatsink. By increasing the effective conductivity of the heat-sink base, a more uniform, low resistance temperature distribution across the whole area is achieved with a thinner and lighter form factor heatsink. A radially oscillating coolant, e.g., water, absorbs heat in the immediate vicinity of the chip with the heat absorber (*HA*) cold plate, spreads it to a larger area, and returns at a lower temperature. When the heated fluid reaches the heat dissipater (*HD*) cold plates, thermal energy is dissipated to ambient air. Several fluidic branches (*N*) shuttle the heat with a periodic phase difference, $\varphi = 2\pi/N$. With at least three branches, fluid can periodically be dispensed in all directions in a plane while maintaining a constant speed flow with a radially oscillating direction at the center of the heat source or chip. By increasing the number of branches, the radial distribution of flow is more uniformly divided [11].

A thermal resistance/capacitance network describes the dynamic behavior [71], [21]. Figure 5.2 illustrates the basic components, such as heat absorber, interconnecting tubes, heat dissipater, and air heatsink. Because of the dynamical operation, each component is exposed to an oscillating heat transfer coefficient and solid-to-liquid temperature difference. Only the center of the heat absorption zone sees a constant temperature and flow. Efforts are currently underway to characterize the time-varying performance of each component. Heat resistance from the dissipating microprocessor to the fluid in the heat absorbing zone is described by R_{sl} . The

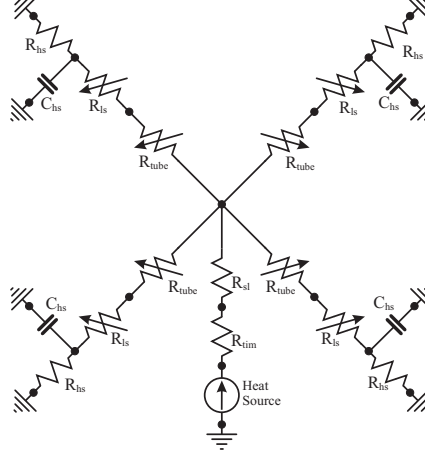


Figure 5.2: Thermal RC model of the RADIOS hybrid cooling system. Heat flows in the liquid from the source through the four branches to the periphery, where it is transferred to air. Variable resistor elements create the characteristic oscillating flow.

variable resistor R_{tube} represents the tube coupling the heat absorber and the heat dissipater. R_{ls} is the heat transfer from liquid to solid and oscillates according to the absolute fluid velocity inside the heat exchanger zone. The air heatsink resistance is described with the block R_{hs} and is not a function of time because air flows constantly across it. C_{hs} represents the thermal capacity. The full model consists of four branches as shown in Fig. 5.2, with the time-varying blocks being identical but phase-shifted by $\varphi = \pi/2$. The description of this RC-model aims at illustrating the driving principle of the cooling system.

5.2.2 Spreader Plate Design

Heat absorption from solid to liquid and heat dissipation from liquid to solid are maximized by a micron-sized copper mesh. Pin-fin-type copper heat exchangers have

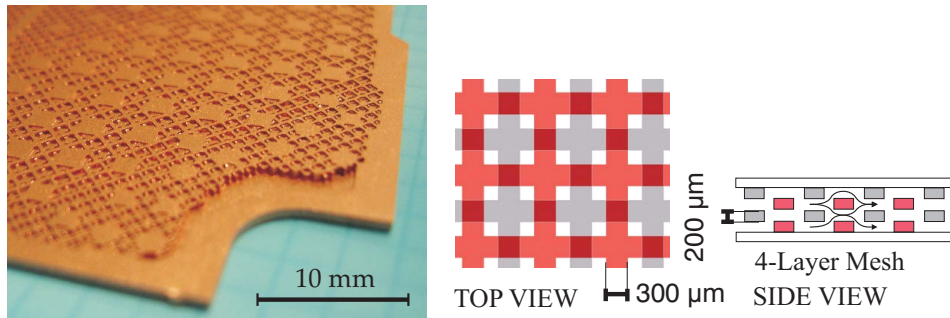


Figure 5.3: RADIOS spreader plates made from stacked micro-patterned copper sheets that form the layered mesh. The cooling fluid flows through the mesh in tortuous manner.

shown high heat transfer rates [72] but cannot be manufactured as thin, stacked metal sheets without loose parts. Therefore we use a layered mesh in which all solid components are interconnected and through which the coolant flows in a similar manner as through an array of horizontal posts to achieve high heat absorption and dissipation, cp. Fig. 5.3. The mesh is produced by stacking thin copper sheets (200 to 300 μm) with through-etched features in a direct bonding process. The manufacturing was done by Curamik (Eschenbach, Germany) and is well suited for mass production. Heat exchanger zones for absorption and dissipation are optimized in terms of pressure drop, thermal resistance, and liquid volume. Reciprocating, phase-shifted membrane pumps create the fluid flow inside the spreader plates. There is one primary spreader plate containing one heat-absorption zone and two secondary spreader plates containing two heat-dissipation zones each. The membrane pumps are directly attached to the backside of the secondary spreader plates or placed remotely where space is available. Commercial voice coil actuators are employed irrespective of power consumption and geometrical constraints. Miniaturized and more efficient actuator versions will be provided later.

5.2.3 Test Vehicle Description

Because of their thin form factor, the RADIOS spreader plates are suitable for many different cooling applications. For example, the heat-absorption plate can be integrated in the base of a finned air heatsink, with the heat-dissipation plates on top of the air fins. In such a configuration, the heat is transported via interconnecting tubes to the top end of the fins with passive conduction spreading in the base plate. Therefore, the air heatsink can be redesigned and improved in terms of performance by uniformly distributing heat to both ends of the air fins. Alternatively, an implementation into a thin form factor system that is densely populated with electrical components is possible: Thanks to its capability to shuttle heat to remote areas, electrical and thermal packaging is optimized.

With the current prototype, we study the spreading effectiveness of the cold plates and compare them with bulk copper in terms of their effective conductivity. The shape of the spreader plates was determined by an existing heatsink product which required the heat absorption and dissipation plates to be placed in the base and on the top of an air heatsink, respectively. This paper investigates the temperature distribution and spreading efficiency of the spreader plates with a focus on the understanding of the general principles of the radially oscillating flow. A discussion of the thermal performance and the characteristics of a full system (including air heatsink, fan, etc.) will follow in a later publication.

Figure 5.4 shows the layout of the first- and second- generation prototype of such a spreader-plate design (D1 and D2). The symmetry axis divides the two different designs, with design D1 on the left and D2 on the right. The absorbing and dissipating plates are connected via copper tubes. In the D1 spreader plate, almost the entire area is populated with the copper mesh, with a higher density is in the vicinity of the chip to maximize heat transfer. The second design reduces the pump volume and optimizes the thermal performance using smaller, heat transfer areas for absorption

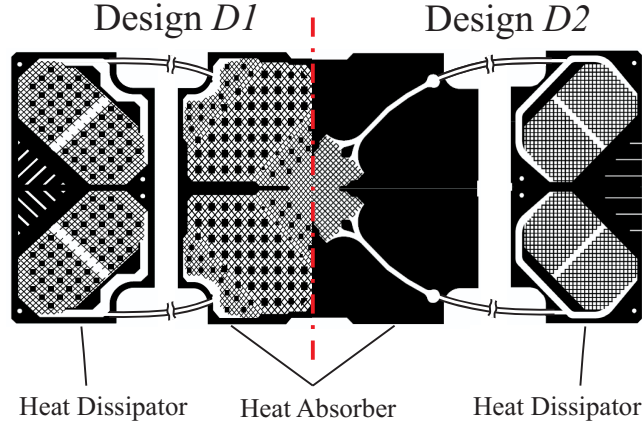


Figure 5.4: Top view of single copper sheet layer of RADIOS heat spreader plate designs D1 and D2. Connection between plates is illustrated schematically. Multiple stacked layers with pattern offset form the spreader plates containing the fluid (cp. Fig. 5.3).

and dissipation. D2 also has a much higher fluid volume-to-heat transfer area ratio right above the microprocessor. Maximizing the solid-liquid temperature difference in the two heat transfer areas optimizes local heat exchange following Newton's law of cooling

$$\dot{q}'' = h \cdot A \cdot \Delta T \quad [W] \quad (5.1)$$

where the fluid takes up thermal energy in the heat-absorbing mesh zone, shuttles it out to the heat-dissipating mesh zone, where heat is exchanged again with a solid. The fluid then returns to chip vicinity at a low temperature level. The total fluid volume is ≈ 4.5 ml, with the fluid flow rate for a four-pump system determined by the following pump relationship:

$$\dot{V} = 4 \cdot f \cdot D_{act} \cdot A_{act} \quad [m^3/s] \quad (5.2)$$

Depending on the power and frequency of the actuators, the fluid displacement D_{act} varies from 0.1 to 0.5 ml (a 0.3 to 1.0 mm actuator stroke) and the flow rate is

between 0.1 and 0.2 liters per minute resulting in a pressure drop across the entire system from 250 to 500 mbar. The best thermal and fluidic performance is reached for frequencies between 1 and 2 Hz. Higher frequencies lead to membrane bulging, and the net volume displacement is reduced. Stiffer membranes would allow faster oscillations but with exponentially increasing power consumption of the actuators.

5.3 Results and Discussions

5.3.1 IR Camera Spreader Evaluation

To allow capturing of surface temperature distributions with an infrared (IR) camera, no air fins were added to the spreader plates. Instead, a high-speed fan impinged air at ambient temperature across the top side of the spreader plates, leading to a rather high overall thermal resistance. To keep the chip below a temperature of $T_j = 358$ K, the heating power was set to $Q_{in} = 10$ W. However, as mentioned earlier, the work presented here aims at comparing the spreading effectiveness of the RADIOS cold plates to passive copper spreaders.

We compared a solid copper device Solid Cu that does not contain any liquid and, therefore, can only spread heat via passive conduction to two different designs D1 and D2 of the RADIOS spreader plate. Note that for the D1 and D2 test vehicle the two secondary spreader plates are arranged along the short and long edge of the primary spreader plate, respectively. Differences in the lateral spacing between the two plates and the Solid Cu test device are compensated by different vertical extension of the inter-connecting tubes, to keep the tube path length constant.

The temperature distribution of the test vehicles is shown in Fig. 5.5. In addition, D1 passive represents the thermal profile of the D1 spreader plate without any liquid pumping; i.e., only passive conduction through the fluid-filled copper mesh. D1 active and D2 active display the time-averaged temperature profile when the actuators

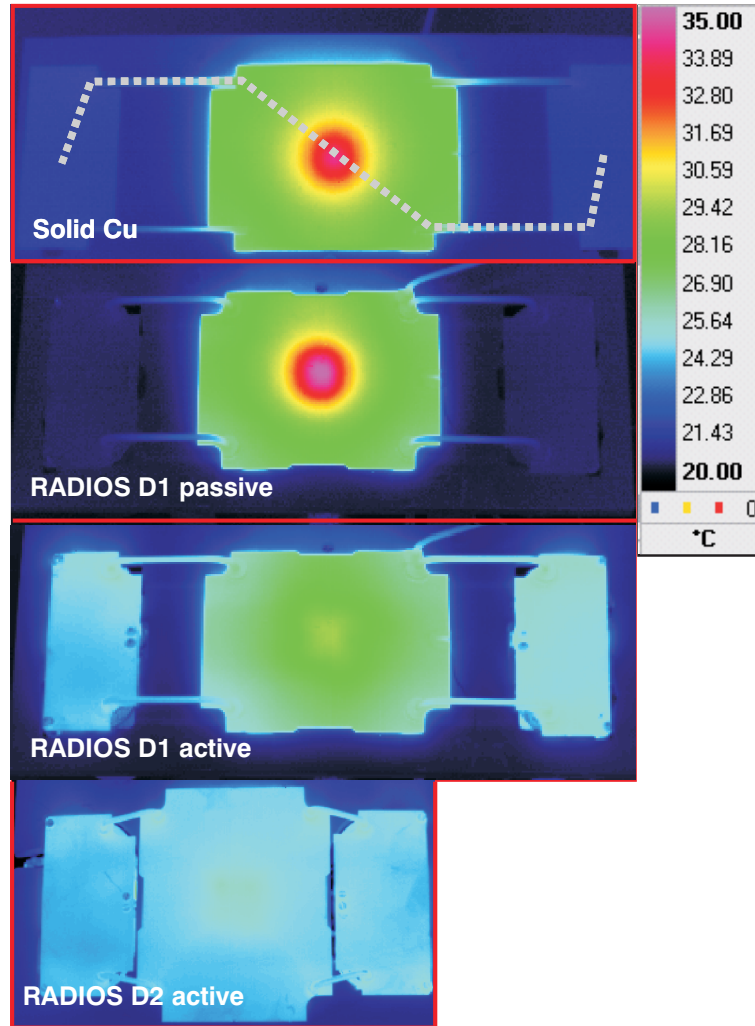


Figure 5.5: Experimental results of the IR imaging of the three different heat spreader plates. Solid Cu represents the reference device with conduction only. RADIOS D1 passive is the D1 spreader plate without any fluid pumping. RADIOS D1 active and RADIOS D2 active are the RADIOS cold plates with fluid oscillation turned on.

are turned on. This leads to a clearly improved temperature distribution compared with the Solid Cu system.

D1 active (max/min [°C]: 29.5/24.8) already has a much smaller temperature difference than Solid Cu does (max/min [°C]: 34.0/22.0). However, the D2 spreader plate exhibits an even more uniform temperature profile compared with its precursor D1. The temperature difference between the hottest and coldest location on the surface is 10X lower with the D2 active (max/min [°C]: 25.9/24.8) than with solid Cu. The IR image of D2 in Fig. 5.5 only points out a slight temperature rise close to the heater chip. Furthermore, it can be stated that by changing from a continuous mesh (D1) to separate regions with narrow channel interconnects (D2), the heat spreading is greatly improved. By comparing the peak temperatures at the heat source, the D1 and D2 plates exhibit a reduction of 13% and 24%, respectively, over the solid copper system. This also corresponds to a 12% improvement for D2 over D1. The same comparison can be seen in Fig. 5.7, which illustrates the IR temperature values along the path indicated by a dashed grey line in Fig. 5.5, in the solid Cu panel.

5.3.2 Model 1 - RADIOS Spreader Plates

To estimate the effective thermal conductivity of the RADIOS spreader plates, a finite element method (FEM) model was established with Qfin 4.0 software, cp. Fig. 5.6. The Qfin code solves the heat conduction in the solid while using empirical models for the heat transfer between the heatsink and the air. Therefore, the full 3D heat conduction equation,

$$\frac{\partial}{\partial x_j} \left(\frac{\partial T}{\partial x_j} \right) = 0 \quad (5.3)$$

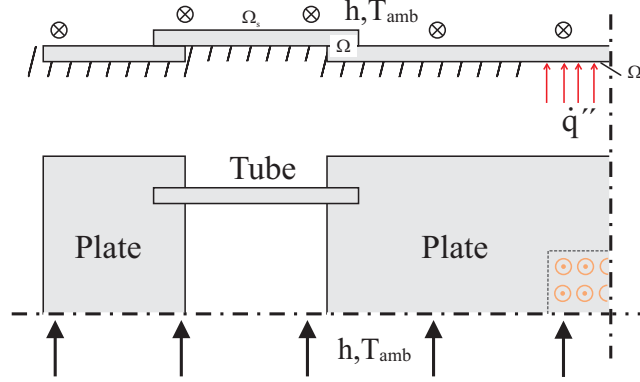


Figure 5.6: Cross section and top view of FEM simulation domain used to fit the experimental results and therefore estimate an effective thermal conductivity of the spreader plates.

with the corresponding boundary conditions on the surfaces,

$$\lambda \left(\frac{\partial T}{\partial x} \right) \Big|_{x \in \Omega_q} = \dot{q}''(\Omega_q), \quad \lambda \left(\frac{\partial T}{\partial x} \right) \Big|_{x \in \Omega_s} = h \cdot [T(\Omega_s) - T_{amb}] \quad (5.4)$$

is solved in the domain of Ω . The same power flux as in the experiment enters the model at Ω_q . Interface resistances between components are neglected, and the backside of the model is assumed to be insulated. The heat transfer coefficient h from the plate surface Ω_s to air was adjusted via the air flow rate until the surface temperature profile matched the experimental data of solid Cu. From thereon, to match the results of the D1 and D2 experiments, the thermal conductivity λ of the spreader plates and the tubes is adapted in the Qfin model. In other words, the models for the two test devices assume net and isotropic heat conduction inside the inside the fluid channels instead of mass flow with its appropriate heat convection rates. This is a drastic simplification of the real situation; however it allows a useful fit of the experimental data to define a metric to quantify the spreading performance of the RADIOS spreader plates.

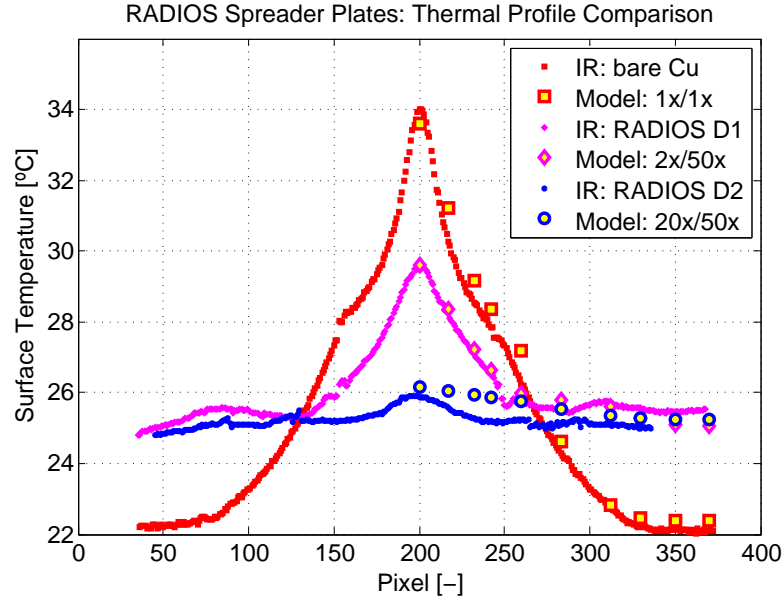


Figure 5.7: Surface temperature profile of the three different heat spreading test devices. Experimental data (small symbols partially fused with lines) are a fit to a FEM model (large symbols).

The large markers in Fig. 5.7 represent the FEM model fit of the three different test vehicles. For D1, the best data fit was achieved by setting λ to 2X and 50X $\lambda_{Cu} = 380 \text{ W m}^{-1} \text{ K}^{-1}$ for the spreader plates and the interconnecting tubes, respectively. Note that effective tube conductivity above 50X does not change the simulation results significantly. Hence, we define λ at its lower bound. For D2 the simulation results matched best by setting λ to 20X and 50X λ_{Cu} for the spreader plates and the interconnecting tubes, respectively. While the models for Solid Cu and D1 reflect the temperature profile of the experimental data to a satisfactory extent, the D2 model data slightly underestimate the spreading effectiveness. This may be due to the anisotropic nature of the D2 spreader design. Nevertheless it provides a good estimate of the efficiency of the spreader plates. Compared with passive spreading

in solid copper, the overall thermal resistance

$$R_{th} = \frac{T_j - T_{amb}}{Q_{in}} \quad [K/W] \quad (5.5)$$

corresponding to the peak temperature, could be reduced by 34 and 64 % with the D1 and D2 cold plates, respectively.

5.3.3 Model 2 - RADIOS Spreader Plates + Solid Base

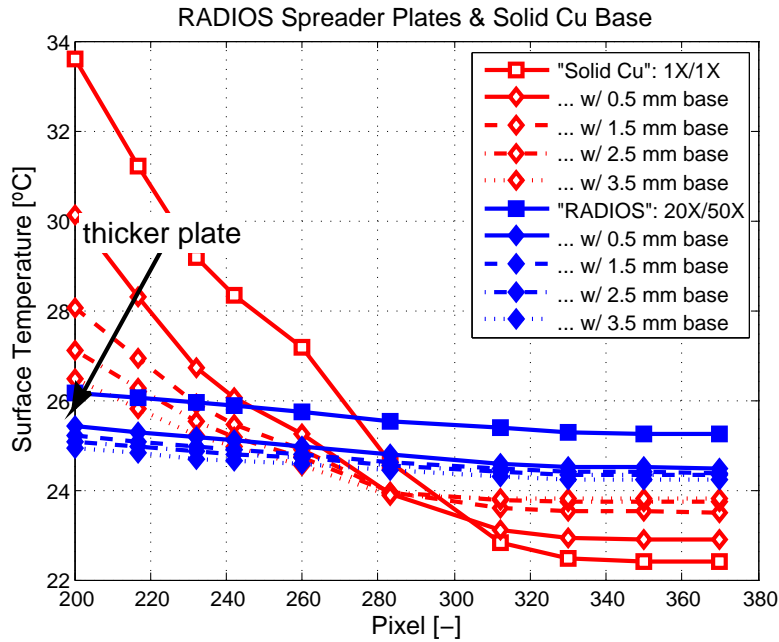


Figure 5.8: Surface temperature profile comparison between solid Cu and RADIOS heat spreading cold plate, with a solid Cu plate attached to the backside to enable better passive conduction.

The comparison presented above only allows heat flux flowing to the heat-dissipating plates via the interconnecting tubes. A system relying purely on thermal conduction would not use such a narrow pathway to spread heat to a larger area, but would instead have a continuous thick solid copper base plate to enhance spreading. A

more realistic comparison that takes this into account was performed using the same plates, tube dimensions, thermal conductivity values for the passive and active devices, heater chip power, and air flow conditions. Figure 5.8 shows the surface temperature profile from the center to the periphery of the spreader (indicated by the dashed grey line in Fig. 5.7). The backside plate thickness varies from 0.5 to 3.5 mm. As a reference performance figure, the setup presented before is illustrated as "Solid Cu": 1X/1X and "RADIOS": 20X/50X. For the solid copper system (λ equaling 1X λ_{Cu} for both plates and tubes), the peak temperature could be lowered from 33.6 °C to 30.1 and 26.5 °C by attaching a solid base plate of 0.5 and 3.5 mm thickness, respectively. This implies a reduction of R_{th} by 30 and 61% respectively. For the RADIOS cold plate approach (λ equaling 20X and 50X λ_{Cu} for the plates and tubes, respectively), the surface peak temperature dropped from 26.2 °C to 25.4 and 24.9 °C when attaching a solid base of the same thickness as reported before. In this case the thermal resistance R_{th} decreased by 18 and 30%. By comparing the two competing systems, the performance gain amounts to 58 and 34% when attaching a solid Cu base of 0.5 and 3.5 mm thickness, respectively, to the backside of the spreader plates.

Figure 5.8 shows that the solid copper system performance is entirely based on the additional heat flux path inside the fin base plate. However, to achieve the same thermal performance as that of the RADIOS spreader plates, a Cu plate of > 3.5 mm thickness is needed. This in turn requires more vertical space or shorter air fins, which increases the heatsink-to-air thermal resistance R_{hs} and therefore the overall system thermal resistance. Furthermore, a 3.5-mm-thick solid Cu base plate with a 100 x 250 mm² footprint adds a significant amount of weight and cost, which is detrimental for portable applications or blade-server modules.

5.4 Summary and Conclusions

We have shown that effective heat spreading from a small power source to a larger area can be achieved by liquid oscillations in a self-contained, micro-fabricated cold plate. Fluid flows were driven radially from membrane actuators with a phase-delayed drive signal. This induced a constant speed flow at the chip heat source with a periodic flow direction. Heat from the source was shuttled to the peripheral heat exchanger plates in each cycle of radial oscillation. Oscillating frequencies in the range of 1 to 2 Hz achieved the best cooling performance with average flow rates of approximately 0.2 lpm.

The thermal resistance was lowered by 64% when changing from a passive copper spreader to the RADIOS heat spreader. From a relative comparison of two different kinds of cold plates for RADIOS, we conclude that it is preferable to design such a spreader plate with discrete heat exchanger areas and to shuttle thermal energy between temperature extremes. A model based on pure thermal conduction exhibits an effective conductivity of the spreader plates and interconnecting tubes of 20X and 50X, respectively. By attaching a solid base plate of 0.5 and 3.5 mm thickness to the aforementioned device the performance gain of the active RADIOS over the passive Cu spreading system amounts to 58 and 34%, respectively. To achieve the same peak surface temperature as the proposed RADIOS heat spreader without any additional base plate, a base plate thicker than 3.5 mm had to be utilized.

The technology has been shown to be highly effective as an ultra-thin form factor heat spreader. Furthermore, it also allows adapting to the dynamic behavior of high power-density heat dissipating devices. RADIOS is most likely to be beneficial for computing systems with a low-profile form factor such as laptops or blade-server modules.

5.5 Outlook

As a next step we will implement membrane actuators that meet the space specifications for low-profile computing systems. Electromagnetic actuators using the effect of resonance will replace the commercial voice coil actuators used for the test device presented in this paper. The power and volumetric displacement will be adjusted to the required frequency range and pump volume. This would also allow a statement regarding the expected system coefficient of power (COP) figure to be made.

Because of its novel oscillating driving principle, we are going to study the thermal and mechanical dynamics of the RADIOS cooling system in detail. A lumped parameter RC model as presented here helps to simulate the full system dynamics, whereas individual components, such as heat exchangers and interconnecting tubes, can be characterized via analytical, numerical. or experimental investigations.

The thermal and fluidic behavior of the micro-machined copper cold plates will be simulated numerically in full scale by defining the mesh as a porous medium. Therefore, the system performance can be studied and optimized with a reasonable computational effort. Experimental investigations of different spreader plate designs enable a verification of the simulations results. We plan to build RADIOS coolers for selected IBM products with large vertical form factor, but also for cooling of compact low-profile blades.

6 Conclusions

The present thesis was targeted to explore the performance limits of a self-contained, oscillating liquid heat spreading system for low form factor electronics. This work exhibits a thorough description of the blade-level heat spreader system dynamics. The characteristic measures of frequency and fluid displacement and the design of the microchannel heat transfer devices were investigated. Therefore, analytical, numerical and experimental work was carried out. The rack-level cooling loop, acting as the thermal ground potential of the blade loop, was introduced pragmatically. The same holds for the fluid displacement pumps.

An efficient methodology to predict the fluidic and thermal performance of a mesh-type microchannel cold plate was presented in Chapter Two. By means of conjugate CFD simulations of a unit cell stack, the fluidic and thermal characteristics of three different cold plate mesh designs were evaluated. The heat transfer mesh porosities were in the range of $58 < \varphi < 46$ %. In order to reach steady-state conditions, periodic boundaries and an automated iteration procedure were applied. Based on the results of the microchannel-scale numerical simulation, analytical network-like models were discussed to calculate the pressure drop and thermal resistance of microchannel cold plate devices. Experimental work has been executed for verification reasons. By comparing the densest with the coarsest heat transfer meshes at a reference flow rate of 250 ml/min, the heat transfer coefficient increases by 25%. In

turn, this leads to a doubling of frictional losses, and the overall cold plate thermal performance improves by 7%.

The heat transfer mesh performance measures discussed in Chapter Two were used in subsequent numerical modeling work, presented in Chapter Three. The microchannel heat transfer mesh was described as fluid-saturated porous media. The model comprises the heat absorber, the interconnecting tubes, and the heat dissipator devices, and, correspondingly, the time-dependent mass, momentum, and energy equations were solved. The dependency of the overall system performance on the heat transfer mesh porosity, the oscillation frequency, and the fluid displacement were investigated. We have shown that the oscillation frequency is constrained to $0.5 \leq f \leq 2$ Hz for a reasonable pressure work. Moreover, the relative fluid displacement per pump stroke is limited to $1 \leq \bar{A} \leq 1.5$. In turn, frequencies of $f > 10$ would be required to reach superior heat transfer rates due to a plug-like flow profile. It was shown that a large fluid displacement and low frequency driving regime is the most effective in terms of pumping power. Furthermore, the requested cooling performance defines the optimal design of the microchannel heat transfer mesh. For a chip size of $15 \times 15 \text{ mm}^2$ and $T_{j,max} = 85 \text{ }^\circ\text{C}$, a maximum heat load of 600 W was identified ($T_{amb} = 20 \text{ }^\circ\text{C}$).

A self-contained, oscillating flow heat spreader prototype, including the heat absorber and heat dissipator cold plates, was built and experimentally investigated, Chapter Four. Thermal and fluidic characteristics were presented in a time-resolved and cycle-averaged manner. The fluid oscillations were created by means of a piston pump of fixed displacement and the high-heat flux microprocessor was represented by a heater/sensor chip. The study of different oscillation flow patterns concludes that the linear oscillation flow mode is superior to the radial oscillation flow mode. This is an important finding since *linear* requires less pump equipment to the system and allows for innovative, centralized data center pump schemes. Moreover, the

self-contained, blade-level oscillating flow loop was directly compared to the corresponding self-contained, uniform-flow loop. While the total thermal resistance was lower by 8%, *linear* exhibits a pressure loss advantage of $> 50\%$ compared to the *steady-flow* configuration. At a pump power of 1 W and $\Delta T = 67$ K, a peak cooling performance of the linearly oscillating flow loop of 180 W/cm^2 was measured. The dependency of the driving parameters on the fluidic and thermal performance corresponded well with the numerical predictions, cp. Chapter Three. Finally, it has been shown that the thermal interface and the heat absorber cold plate contribute by 65% to the total thermal budget.

Chapter Five covers some experimental and simulation work on an implementation of the oscillating liquid heat spreader into an existing IBM product. The advantage of the self-contained oscillating flow heat spreading system has been demonstrated. Two different heat transfer mesh layouts were tested and the effective thermal conductivity and thinning potential were discussed. It was concluded that a spreader plate design with discrete absorber/dissipator heat transfer areas are preferable. Experimental data from thermographic measurements was inserted into a numerical heat conduction model. An effective thermal conductivity of 20X and 50X higher than copper for the microchannel plates and the interconnecting tubes was identified, respectively.

The thesis at hand provides the key information on the characteristic behavior of the proposed self-contained, oscillating liquid heat spreader for low form factor electronics. Namely, the fluid displacement \bar{A} , the oscillation frequency f and the microchannel heat transfer designs V_i . A peak heat load of 180 W/cm^2 has been demonstrated which is very close to the aspired 2X improvement compared to present-day air cooling solutions for blade-type server modules. With the heat absorber cold plate and the corresponding thermal interface accounting for the majority of the chip junction-

to-ambient thermal resistance, a further optimization of those devices pay off from a performance point of view.

The microchannel heat transfer structure developed in this work was optimized for multi-phase fluid flow patterns, referred to as *radial*. It was concluded that the linear oscillation flow mode is preferable from a pump power perspective. Therefore, the heat transfer mesh design for a successive application running solely *linear* had to be improved towards a higher solid surface-to-volume ratio of the unit cell. The main improvement is to be expected in the reduction of the pressure losses inside the microchannel heat transfer channels. The chip-to-absorber interface resistance could be improved by thinning and optimizing the thermal interface material. The same holds for the thermal path between the dissipator cold plates and the rack-level flow loop. The concept of direct jet impingement on the microprocessor [8] could be applied to the oscillating liquid heat spreader. An assumptive reduction of the absorber and interface thermal budget by 50% would therefore increase the maximum heat load to some 250 W/cm^2 ($\Delta T = 65 \text{ K}$, $2 \times 2 \text{ cm}^2$ chip area).

Despite the striking cooling performance improvement demonstrated in this work, the advantages of the self-contained, oscillating liquid heat spreader system are multifaceted; the small fluid volume, the hermetically sealed fluid flow loop, the partition between blade-level and rack-level cooling circuit, and the improved flow and thermal profiles within channels to be named again. However, the thesis at hand presents some initial conceptions on the fluid pumping scheme and the secondary, rack-level cooling loop. Investigative work is to be conducted thereof. The conclusions and findings of the available research give way to essential improvements in data center thermal management.

Bibliography

- [1] J. G. Koomey, “Worldwide electricity used in data centers,” *Environmental Research Letters*, p. 034008 (8 pp.), 2008.
- [2] J. Scaramella, “Worldwide server power and cooling expense: 2006-2010 forecast,” IDC, Tech. Rep., 2006. [Online]. Available: <http://whitepapers.silicon.com/0,3800002489,60301990p,00.htm?dl=1>
- [3] J. Humphreys and J. Scaramella, “The impact of power and cooling on data-center infrastructure,” IDC Report, Tech. Rep. Doc. 201722, 2006.
- [4] “Ibm bladecentre and system x reference sheet,” IBM STG Field Skills Education Team, 2009. [Online]. Available: <http://www.redbooks.ibm.com/xref/usxref.pdf>
- [5] D. M. Desai *et al.*, “Bladecenter system overview,” *IBM Journal Of Research And Development*, vol. 49, no. 6, pp. 809–821, 2005.
- [6] D. B. Tuckerman and R. F. W. Pease, “High-performance heat sinking for VLSI,” *Electron Device Letters*, vol. 2, no. 5, pp. 126–129, 1981.
- [7] K. Vafai and L. Zhu, “Analysis of two-layered micro-channel heat sink concept in electronic cooling,” *International Journal of Heat and Mass Transfer*, vol. 42, no. 12, pp. 2287–2297, 1999.
- [8] T. Brunschwiler *et al.*, “Direct liquid jet-impingement cooling with micron-sized nozzle array and distributed return architecture,” in *10th Intersociety Conference on Thermal and Thermomechanical Phenomena in Electronic Systems*, 2006, pp. 196–203.

- [9] E. G. Colgan *et al.*, “High performance and subambient silicon microchannel cooling,” *Transactions of the ASME, Journal of Heat Transfer*, pp. 1046–51, 2007.
- [10] H. Y. Zhang *et al.*, “Single-phase liquid cooled microchannel heat sink for electronic packages,” *Applied Thermal Engineering*, vol. 25, no. 10, pp. 1472–87, 2005.
- [11] T. J. Brunschwiler *et al.*, “Heat spreader,” U.S. Patent 017 659 A1, 2007.
- [12] T. J. Brunschwiler, R. J. Linderman, B. Michel, and R. Waelchli, “Method and device for cooling a heat generating component,” W.O. Patent 031 100 A1, 2009.
- [13] S. U. S. Choi *et al.*, “Anomalous thermal conductivity enhancement in nanotube suspensions,” *Applied Physics Letters*, vol. 79, no. 14, pp. 2252–2254, 2001.
- [14] J. A. Eastman *et al.*, “Anomalous increased effective thermal conductivities of ethylene glycol-based nanofluids containing copper nanoparticles,” *Applied Physics Letters*, vol. 78, no. 6, pp. 718–720, 2001.
- [15] T. Brunschwiler, E. Smith, B. Rüttsche, and B. Michel, “Datacenters with direct energy re-use,” in *International Supercomputing Conference*, 2008.
- [16] B. Agostini *et al.*, “State of the art of high heat flux cooling technologies,” *Heat Transfer Engineering*, vol. 28, no. 4, pp. 258–281, 2007.
- [17] K. G. Jillek W., *Handbuch der Leiterplattentechnik*, 1st ed. Bad Salgau: Eugen G. Leuze Verlag, 2003.
- [18] J. Schulze-Harder, “Efficient cooling power electronics,” in *PCIM Conference, Shanghai*, 2006, pp. 208–212.
- [19] K. Boomsma and D. Poulikakos, “The effects of compression and pore size variations on the liquid flow characteristics in metal foams,” *ASME Journal Of Fluids Engineering*, vol. 124, no. 1, pp. 263–272, Mar. 2002.
- [20] R. Wälchli *et al.*, “Radially oscillating flow hybrid cooling system for low profile electronics applications,” in *24th Annual IEEE Semiconductor Thermal Measurement and Management Symposium*, 2008, pp. 142–8.

- [21] M. N. Sabry, "Compact thermal models for electronic systems," *IEEE Transactions On Components And Packaging Technologies*, vol. 26, no. 1, pp. 179–185, 2003.
- [22] Y. Peles *et al.*, "Forced convective heat transfer across a pin fin micro heat sink," *International Journal Of Heat And Mass Transfer*, vol. 48, no. 17, pp. 3615–3627, 2005.
- [23] F. Incropera and D. P. De Witt, *Fundamentals of Heat and Mass Transfer*, 5th ed. John Wiley & Sons, New Jersey, 2002.
- [24] ANSYS, "Documentation for ansys icem cfd /aii environment," release 11.0.
- [25] ANSYS, "Ansys cfx - solver theory guide," December 2006, aNSYS CFX Release 11.0 Documentation.
- [26] T. Barth and D. Jespersen, "The design and application of upwind schemes on unstructured meshes," in *Aerospace Sciences Meeting, Reno*, 1989, p. 13.
- [27] C. Rhie, "Pressure-based navier-stokes solver using the multigrid method," *AIAA Journal*, vol. 27, no. 8, pp. 1017–1018, 1989.
- [28] S. Patankar, C. Liu, and E. Sparrow, "Fully developed flow and heat-transfer in ducts having streamwise-periodic variations of cross-sectional area," *ASME Journal Of Heat Transfer*, vol. 99, no. 2, pp. 180–186, 1977.
- [29] K. Boomsma, D. Poulikakos, and Y. Ventikos, "Simulations of flow through open cell metal foams using an idealized periodic cell structure," *International Journal Of Heat And Fluid Flow*, vol. 24, no. 6, pp. 825–834, 2003.
- [30] K. Boomsma, D. Poulikakos, and F. Zwick, "Metal foams as compact high performance heat exchangers," *Mechanics Of Materials*, vol. 35, no. 12, pp. 1161–1176, 2003.
- [31] S. Lee, S. Van Au, and K. Moran, "Constriction/spreading resistance model for electronics packaging," in *ASME/JSME Thermal Engineering Conference*, vol. 4, 1995, pp. 199–206.

- [32] S. Krishnan, S. V. Garimella, G. M. Chrysler, and R. V. Mahajan, "Towards'a thermal moore's law," *IEEE Computer Transactions On Advanced Packaging*, vol. 30, no. 3, pp. 462–474, 2007.
- [33] P. Rodgers, V. Eveloy, and M. G. Pecht, "Limits of air-cooling: Status and challenges," *Twenty-First Annual IEEE Computer Semiconductor Thermal Measurement And Management Symposium, Proceedings 2005*, pp. 116–124, 2005.
- [34] T. Brunswiler, B. Smith, E. Rütscche, and B. Michel, "Toward zero-emission data centers through direct reuse of thermal energy," *IBM Journal Of Research And Development*, vol. 53, no. 3, 2009, paper 11.
- [35] R. Wälchli, T. Brunswiler, B. Michel, and D. Poulikakos, "Combined local microchannel-scale cfd modeling and global chip scale network modeling for electronics cooling design," *International Journal of Heat and Mass Transfer* (submitted), 2009.
- [36] D. A. Nield and A. V. Kuznetsov, "Effects of heterogeneity in forced convection in a porous medium: Parallel-plate channel, asymmetric property variation, and asymmetric heating," *Journal Of Porous Media*, vol. 4, no. 2, pp. 137–148, 2001.
- [37] D. A. Nield, A. V. Kuznetsov, and M. Xiong, "Effect of local thermal non-equilibrium on thermally developing forced convection in a porous medium," *International Journal Of Heat And Mass Transfer*, vol. 45, no. 25, pp. 4949–4955, 2002.
- [38] A. Nakayama, H. Koyama, and F. Kuwahara, "An analysis on forced-convection in a channel filled with a brinkman-darcy porous-medium - exact and approximate solutions," *Warme Und Stoffubertragung-Thermo And Fluid Dynamics*, vol. 23, no. 5, pp. 291–295, 1988.
- [39] A. F. Miguel and A. H. Reis, "Transient forced convection in an isothermal fluid-saturated porous-medium layer: Effective permeability and boundary layer thickness," *Journal Of Porous Media*, vol. 8, no. 2, pp. 165–174, 2005.
- [40] D. Poulikakos and K. Renken, "Forced convection in a channel filled with porous medium, including the effects of flow inertia, variable porosity, and brinkman

- friction,” *Transactions of the ASME. Journal of Heat Transfer*, vol. vol.109, no.4, pp. 880–8, 1987.
- [41] M. Kaviani, “Laminar-flow through a porous channel bounded by isothermal parallel plates,” *International Journal Of Heat And Mass Transfer*, vol. 28, no. 4, pp. 851–858, 1985.
- [42] K. Boomsma and D. Poulikakos, “On the effective thermal conductivity of a three-dimensionally structured fluid-saturated metal foam,” *International Journal Of Heat And Mass Transfer*, vol. 44, no. 4, pp. 827–836, 2001.
- [43] S. Krishnan, S. V. Garimella, and J. Y. Murthy, “Simulation of thermal transport in open-cell metal foams: Effect of periodic unit-cell structure,” *Journal Of Heat Transfer-Transactions Of The ASME*, vol. 130, no. 2, 2008.
- [44] R. Wälchli, T. Brunschweiler, B. Michel, and D. Poulikakos, “Self-contained, oscillating flow liquid cooling system for thin form factor high performance electronics,” *Journal of Heat Transfer* (in press), 2009.
- [45] D. Nield and A. Bejan, *Convection in Porous Media*, 3rd ed. New York: Springer, 2006.
- [46] J. Lage, *The fundamental theory of flow through permeable media from darcy to turbulence*, In: *Transport Phenomena in Porous Media*, D. Ingham and I. Pop, Eds. Elsevier Science Ltd., 1998.
- [47] A. Bejan *et al.*, *Porous and Complex Flow Structures in Modern Technologies*. New York: Springer, 2004.
- [48] P. Forchheimer, “Water movement through the ground.” *Zeitschrift Des Vereines Deutscher Ingenieure*, vol. 45, pp. 1781–1788, 1901.
- [49] H. Darcy, “Les fontaines publiques de la ville de dijon,” Victor Dalmont, Paris, 1856.
- [50] H. C. Brinkman, “On the permeability of media consisting of closely packed porous particles,” *Applied Scientific Research Section A-Mechanics Heat Chemical Engineering Mathematical Methods*, vol. 1, no. 2, pp. 81–86, 1948.

- [51] M. J. Crippen *et al.*, “Bladecenter packaging, power, and cooling,” *IBM Journal Of Research And Development*, vol. 49, no. 6, pp. 887–904, 2005.
- [52] R. Bianchini and R. Rajamony, “Power and energy management for server systems,” *IEEE Computer*, vol. 37, no. 11, pp. 68–+, 2004.
- [53] T. Brey *et al.*, “Bladecenter chassis management,” *IBM Journal Of Research And Development*, vol. 49, no. 6, pp. 941–961, 2005.
- [54] P. Patel *et al.*, “Ibm bladecenter system electrical packaging design challenges,” in *IEEE 13th Topical Meeting on Electrical Performance of Electronic Packaging*, 2004, pp. 11–14.
- [55] L. Sauciuc, G. Chrysler, R. Mahajan, and M. Szleper, “Air-cooling extension - performance limits for processor cooling applications,” in *19th Annual IEEE Semiconductor Thermal Measurement and Management Symposium*, 2003, pp. 74–81.
- [56] R. Siegel and M. Perlmutter, “Heat transfer for pulsating laminar duct flow,” *Journal of Heat Transfer*, vol. 84, pp. 111–122, 1981.
- [57] U. H. Kurzweg and L. Dezhao, “Heat-transfer by high-frequency oscillations - a new hydrodynamic technique for achieving large effective thermal-conductivities,” *Physics Of Fluids*, vol. 27, no. 11, pp. 2624–2627, 1984.
- [58] W. L. Cooper, V. W. Nee, and K. T. Yang, “An experimental investigation of convective heat-transfer from the heated floor of a rectangular duct to a low-frequency, large tidal displacement oscillatory flow,” *International Journal of Heat and Mass Transfer*, vol. 37, no. 4, pp. 581–592, 1994.
- [59] Q. Lia, K. Yang, and V. Nee, “Enhanced microprocessor chip cooling by channeled zero-mean oscillatory air flow,” in *Proc. of INTERpack 95, Lahaina, HI*, 1995, pp. 789–794.
- [60] C. Sert and A. Beskok, “Oscillatory flow forced convection in micro heat spreaders,” *Numerical Heat Transfer Part A*, vol. 42, no. 7, pp. 685–705, 2002.

-
- [61] E. Kurzweg, U.H. Lindgren and B. Lothrop, "Onset of turbulence in oscillating flow at low wormersley number," *Physics of Fluids A*, vol. 1, no. 12, pp. 1972–1975, 1989.
- [62] S. Sergeev, "Fluid oscillations in pipes at moderate reynolds numbers," *Fluid Dynamics*, vol. 1, pp. 121–122, 1966.
- [63] M. Hino, M. Sawamoto, and S. Takasu, "Experiments on transition to turbulence in an oscillating pipe flow," *Journal of Fluid Mechanics*, vol. 75, pp. 193–207, 1976.
- [64] P. Merkli and H. Thomann, "Transition to turbulence in oscillating pipe flow," *Journal of Fluid Mechanics*, vol. 68, pp. 567–575, 1975.
- [65] T. Zhao and P. Cheng, "A numerical solution of laminar forced convection in a heated pipe subjected to a reciprocating flow," *International Journal of Heat and Mass Transfer*, vol. 38, no. 16, pp. 3011–3022, 1995.
- [66] E. G. Richardson and E. Tyler, "Transverse velocity gradient near the mouths of pipes in which an alternating or continuous flow of air is established," *Proceedings of the Physical Society*, pp. 1–15, 1929.
- [67] International Technology Roadmap for Semiconductors (ITRS), 2006. [Online]. Available: <http://www.itrs.net/Links/2007ITRS/Home2007.htm>
- [68] J. U. Knickerbocker *et al.*, "An advanced multichip module (MCM) for high-performance UNIX servers," *IBM Journal Of Research And Development*, vol. 46, no. 6, pp. 779–804, 2002.
- [69] J. R. Culham, W. A. Khan, M. M. Yovanovich, and Y. S. Muzychka, "The influence of material properties and spreading resistance in the thermal design of plate fin heat sinks," *Transactions of the ASME, Journal Of Electronic Packaging*, vol. 129, no. 1, pp. 76–81, 2007.
- [70] R. S. Prasher, "A simplified conduction based modeling scheme for design sensitivity study of thermal solution utilizing heat pipe and vapor chamber technology," *Transactions of the ASME, Journal of Electronic Packaging*, vol. vol.125, no.3, pp. 378–85, 2003.

- [71] T. Hauck and T. Bohm, “Thermal RC-network approach to analyze multichip power packages,” in *16th Annual IEEE Semiconductor Thermal Measurement and Management Symposium*, 2000, p. 10.1109/STHERM.2000.837088.
- [72] P. Y. Kosar A., “Thermal-hydraulic performance of mems-based pin fin heat sink,” *Transactions of the ASME, Journal Of Heat Transfer*, vol. 128, no. 2, pp. 121–131, 2006.